OPTIMIZATION OF THE PROMPT GAMMA SITE AT THE McMASTER NUCLEAR REACTOR FOR IN VIVO NEUTRON ACTIVATION ANALYSIS

OPTIMIZATION OF THE PROMPT GAMMA SITE AT THE McMASTER NUCLEAR REACTOR FOR IN VIVO NEUTRON ACTIVATION ANALYSIS

By

Jovica Atanackovic, B.Sc.

A Thesis

Submitted to the School of Graduate Studies

in Partial Fulfilment of the Requirements

for the Degree

Master of Science

McMaster University

MASTER OF SCIENCE (2004)
(Medical Physics)

McMaster University
Hamilton, Ontario

TITLE: Optimization of the Prompt Gamma Site at the McMaster Nuclear Reactor for in vivo Neutron Activation Analysis

AUTHOR: Jovica Atanackovic B.Sc. (McMaster University)

SUPERVISOR: Professor David Chettle

NUMBER OF PAGES: xiii, 112

Abstract

This work was the first study at the beam port # 4 at the McMaster Nuclear Reactor, involving prompt gamma in vivo neutron activation analysis. The project consisted of experimental and computational parts. The computational part was done using MCNP program, which simulates the neutron and photon transport in the medium. The first thing assessed was the energy dependent neutron fluence rate in the collimated neutron beam, at the site. This was done in order to figure out the complete source (sdef) card for further MCNP calculations. This was combined experimental and computational work. For the experimental part, various activation foils were used and computational part was done by using MCNP programming.

The second part of the project involved experimental prompt gamma in vivo activation analysis using 7 different phantoms, ranging from 30 mL to 2 L. Three different elements were observed. The prompt gamma in vivo detection of cadmium was the preliminary calibration study and the experiments were done with all seven phantoms. The calibration lines and MDL were assessed for all phantoms, with concentration ranging from 0 to 50 ppm. The prompt gamma in vivo detection of boron and mercury was done using 30 mL phantoms. Calibration lines and MDL for both elements were assessed as well.

MCNP experimental simulations for 30 mL water phantoms were done and they were in close agreement with the experimental results. Furthermore, the MCNP gamma and neutron dose survey in the cave was done.

The results obtained showed that there are numerous open possibilities for improvement in terms of in vivo prompt gamma analysis at the site. It predominantly includes the improvements in prompt gamma detection techniques and MCNP source definition. Furthermore, it was found that MCNP programming is the ideal tool for assessment and control of the experimental results in this case. It means that in the future research, the MCNP modeling will be the essential part of the in vivo prompt gamma activation analysis at this beam port.

Acknowledgments

Firstly, I would like to express my greatest gratitude to my supervisor Dr. David Chettle for guiding me through this project. He is the person who believed in me from the beginning (regardless of my total fiasco in his course 5 years ago) and taught me ***how the research is done independently,*** by giving me complete freedom to implement my own ideas and never interfering with them. He was always there with his great knowledge and experience in the field, to finely shape those ideas and make them look just right. David, thank you for letting me fully express myself. This is, for me, the most important lecture learned from this project, even more important than determining neutron spectra or finding the MDL for cadmium phantoms. I would also like to use this opportunity to thank him for partially financing my MCNP course.

Secondly, I would like to express my appreciation to Dr. Fiona McNeill for being so considerate and giving me the second chance for entering the program. If it weren't for Fiona, these words would have never been written.

Alice Pidruczny is one of the people whom I admire and respect with all my heart. During the last two years I've been annoying her constantly, but she was always there, with her positive and shining attitude to help me get into the prompt gamma analysis field and give me the most precise and best advice. She is the most organized person I've ever met, who does not know for "NO", "CAN'T ", "IMPOSSIBLE". Alice thank you for everything!

I would also like to thank Dr. Soo-Huyn Byun for his tremendous help regarding MCNP calculations and prompt gamma detection system. Furthermore, I would like to thank McMaster Nuclear Reactor, particularly Mike Butler and Chris Heysel for hiring me to work in MNR for one year prior to the start of my MSc. Working there was a great experience. Also, I would like to thank them for funding my RA during my MSc and partially funding my MCNP course.

A huge thank for my wife Jelena, who gave a birth to our beautiful Ana (today, Sept 11 @ 0750 AM), for being great and considerate during last 9 months. Furthermore, I would like to thank my sister Vasilisa, brother Vladan and parents Svetlana and Zoran for giving me the best support for the last two years.

Finally, last but not least, the biggest thank for Vera and Marija, the two girls who were giving me the best "summer balcony support".

Table of Contents

List of Figures

List of Tables

CHAPTER I

Introduction and Theory

1.1 The McMaster Nuclear Reactor (MNR)

McMaster Nuclear Reactor (MNR) is a light water moderated, pool type, research nuclear reactor, located at the central campus at McMaster University. The MNR currently runs on combination of high (HEU) and low (LEU) enriched ^{235}U fuel assemblies. The HEU has the form of UAl-Al or UO_3-Al. Every fuel assembly has 196 g of ^{235}U. The enrichment of HEU is 93%. The LEU has the form of U_3Si_2-Al with loadings of 225 or 284 g of ^{235}U per assembly. The enrichment of LEU is 19.75% **[Kennedy]**.

The reactor core is defined as a rectangular box of axial height of 60 cm. The base of the core is divided into a 9×6 sites, each site is approximately 8 cm by 8 cm square. The columns are labeled with letters A to F, while rows are labeled with numbers 1 to 9. Out of these 54 sites, there are 35 sites for fuel elements, where 6 fuel element sites are hollow, for control rod insertion. There are also 8 sites for graphite reflectors, one site for a beryllium reflector and there are 10 "empty" water sites, where samples for irradiation sit **[Kennedy]**.

The reactor runs at a nominal power of 2 MW. Although it has a licence for 3 MW, the reactor runs at this power very rarely, only when there is a definite need for that. The reactor runs in two shifts, every week day from 8 AM to midnight, with shut down periods of 8 hours (from midnight to 8 AM, following morning). During the weekends the reactor is down; however, if needed, the reactor can be run on Saturdays. The MNR is light water moderated. It is cooled via primary and secondary cooling systems. The

primary cooling system is nothing but the gravity flow of primary water through the reactor core. The secondary cooling system involves two heat exchangers and two cooling towers located outside the reactor building. The heat generated by MNR is released into the atmosphere via cooling towers. Furthermore, light water in MNR is cleaned by a demineralizer system that runs primary water through the appropriate mixture of organic cation and anion resins. This greatly reduces various mineral concentrations in the primary water, and therefore reduces gamma fields above the pool and therefore in the reactor building. More detailed information about MNR and how it functions is available on the official web site of MNR **[MNR website]**.

As mentioned above, the MNR is a research reactor, but the main source of funding for this reactor is the production of ^{125}I for medical purposes. The MNR has 6 beam ports where various research applications or projects are taking place throughout the year. The main academic users of MNR are the departments of physics, medical physics, engineering physics, biology and chemistry.

This research, involving prompt gamma beam port, (bp # 4), is the first project of this kind performed at this beam port. More information about bp # 4 and prompt gamma analysis will be available in the following sections of this chapter.

1.2 Reactor Neutron Spectrum

As it was said above, MNR runs on ^{235}U enriched fuel. The neutrons from this fission process have an average energy of 2 MeV **[Duderstadt]**. In light water moderated reactors, like MNR, the neutrons are slowed down by collisions with moderator atoms (water in this case), until they come into the thermal equilibrium with

them. This corresponds to neutron energy of 0.0253 eV **[Technical report 107]**. The fission neutron spectrum represents the fission neutron energy immediately after the fission occurred. This continuous spectrum can be analytically described by any one of the three equations; Cranberg, Grundl and Watt's equations **[Technical report 107]**. See the figure below:

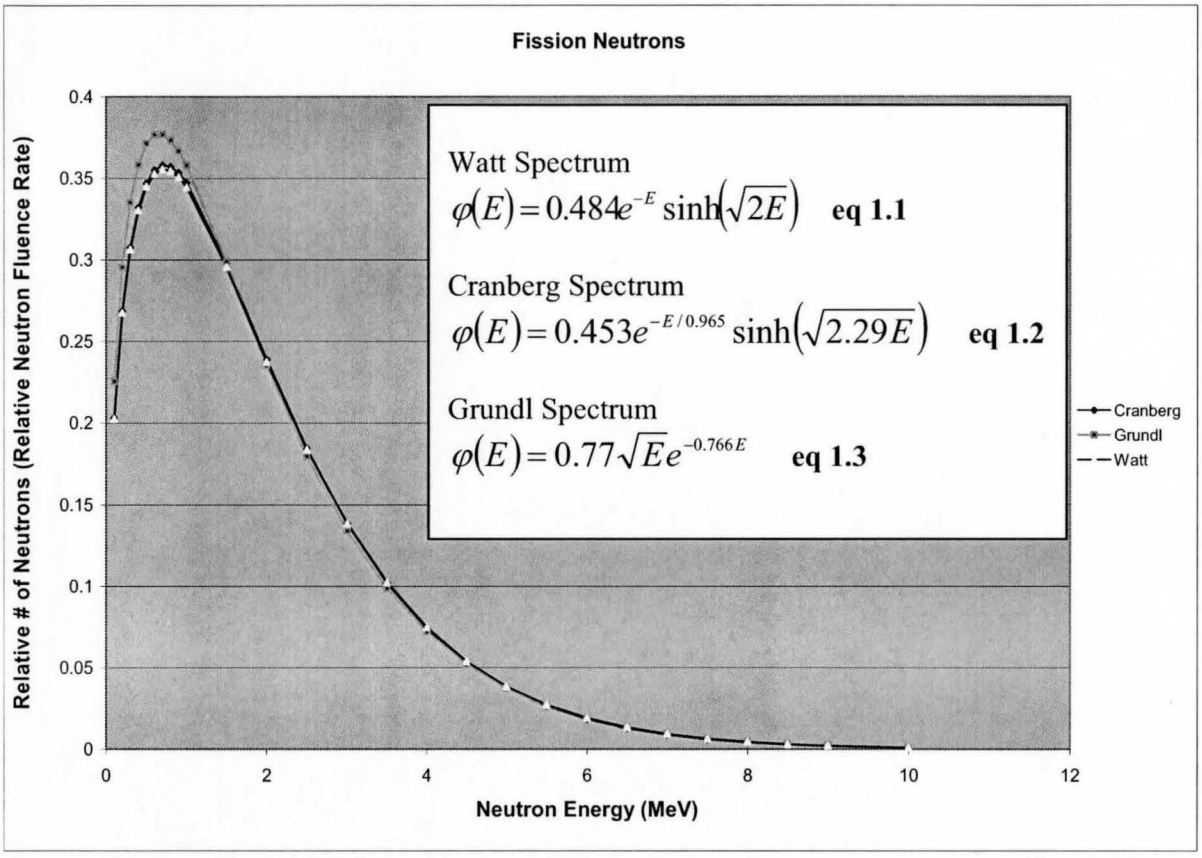

Figure 1.1: *Cranberg, Grundl and Watt's analytical representations of the neutron fission spectrum*

As seen from the figure 1.1, the three spectra are very similar and they overlap each other, almost entirely. Note that the energy input for all three equations is in MeV. It is also important to realize that these are not absolute values for neutron fluence rates. These equations represent relative values of neutron fluence rate, or the shape of the

spectrum. The absolute value for neutron fluence rates predominantly depends on reactor power and fuel used. It also depends on the core and fuel elements' shape.

Furthermore, fission neutrons in MNR are moderated to thermal neutron energies very rapidly (μs range). Theoretically, the thermal neutron energy distribution is described by the Maxwellian fluence rate distribution **[Technical report 107]**:

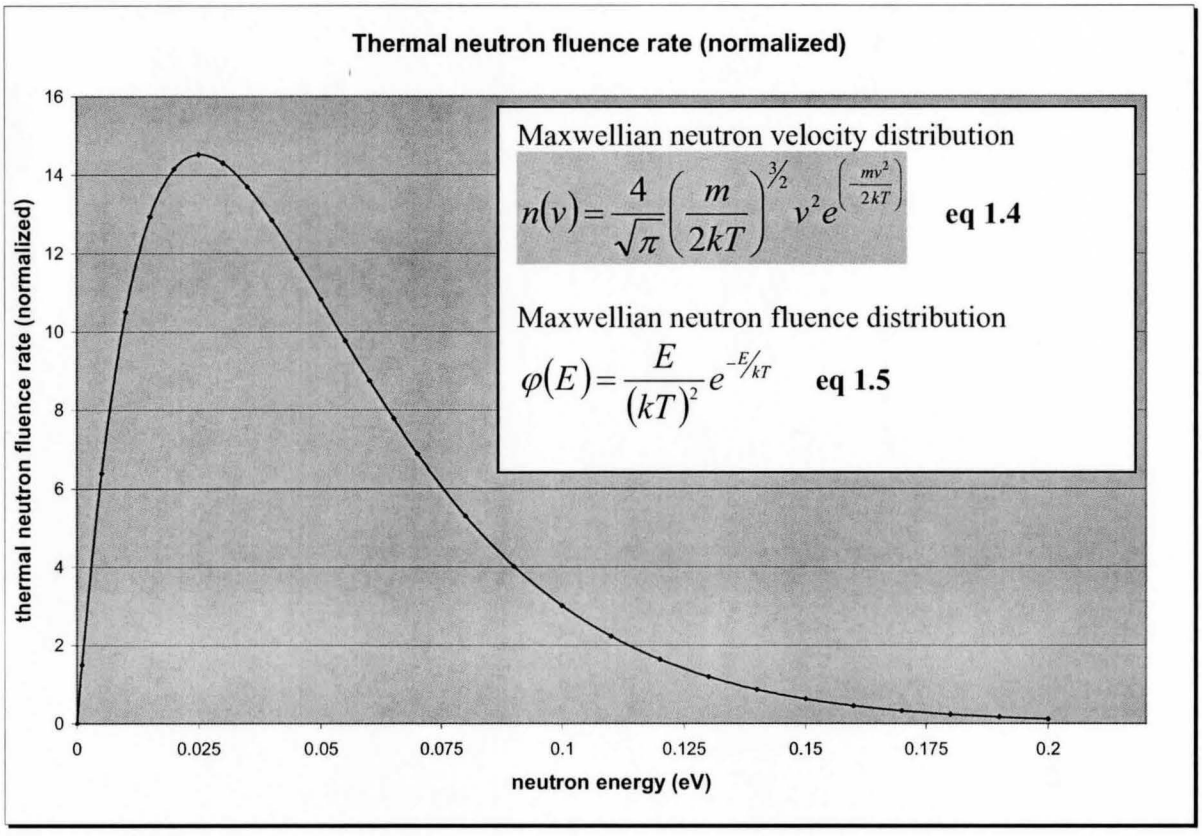

Figure 1.2: *Normalized thermal neutron fluence as a function of neutron energy.*

The equations 1.4 and 1.5 represent the same feature. The first equation given, 1.4, represents the distribution of neutrons (# of neutrons) as a function of neutron velocity. The second equation, 1.5, (equation of the graph) represents the normalized thermal neutron fluence rate as a function of the corresponding neutron kinetic energy, where neutron kinetic energy and neutron velocity are related by the basic formula:

$$E_k = \frac{mv^2}{2} \quad \textbf{eq 1.6}$$

Differentiating equation 1.5 with respect to energy and setting the derivative to zero, in order to find maximum value of the function, we find out that the neutron energy for maximum value of the φ(E) function corresponds to E = kT (k is Boltzman's constant). For room temperature of 20.44°C, E = 0.0253 eV (as can be seen from figure 1.2). This is the most probable energy for thermal neutrons at this temperature. Furthermore, this kinetic energy corresponds to the neutron velocity of about 2.2 km/s (when 0.0253 eV is substituted into equation 1.6).

The above equations and graphs explain the thermal portion of the neutron spectrum. The complete reactor neutron spectrum goes up to about 12 MeV (neutron kinetic energy). Because of that large span, the neutron reactor spectrum is arbitrarily divided into thermal, intermediate and fast **[Technical report 107]**. The thermal neutron spectrum is described above and it is the most important part of the reactor neutron spectrum as far as neutron capture reactions are concerned. Almost all elements of interest have the best cross section values for thermal neutrons. Arbitrarily, the thermal neutrons are those neutrons whose kinetic energy lies between 0 and 0.4 eV (cadmium cut off energy) **[Kruger]**. The intermediate neutrons (also known as epithermal or resonance) are those neutrons with kinetic energies above the cadmium cut off, up to about 100 keV. Finally, the fast neutrons are in the range above 100 keV up to the end of spectrum (about 12 MeV) **[Technical report 107]**. The fast portion of the reactor neutron spectrum is described analytically by fission neutron spectrum above (see figure 1.1 and equations 1.1, 1.2 and 1.3). In theory and in the literature, Watt's analytical

spectrum is used most frequently for picturing the fast portion of a reactor neutron spectrum **[Technical report 107]**.

The most complicated region of the reactor neutron spectrum is the intermediate or resonance region. However, this project does not go into the detailed exploration of the intermediate region, because that is not the main goal of the project. The important thing is to emphasize that intermediate neutron fluence rate is approximated with 1/E distribution, where E is the kinetic energy of the neutron, obviously. In other words, the relationship between intermediate neutron fluence rate and neutron energy is given by **[Technical report 107]**:

$$\varphi(E)dE = \frac{q_0}{\xi N \sigma_s}\frac{dE}{E} \quad \textbf{eq 1.7}$$

Where q_0 is the source density, ξ is the average logarithmic energy decrement per collision, N is the number of slowing down atoms per unit volume and σ_s is the microscopic scattering cross section. Now, combining these three theoretical and analytical approximations of the reactor neutron spectrum, the following curve (Figure 1.3) is obtained. This curve spans a whole neutron spectrum region (from 10^{-5} eV up to 10^7 eV) **[Swift-Schultz]**. Note that values for fluence rate (in this case neutron flux density) are not absolute. Again, the only important thing is the shape of the curve that is spanned from near zero energy to 10^7 eV. Three regions, namely thermal, intermediate and fast are clearly indicated and they are analytically described by the given equations. One of the tasks for this project is to explore and define, as well as possible, the neutron reactor spectrum for the prompt gamma irradiation site, using a theoretical knowledge outlined here and appropriate experiments and calculations.

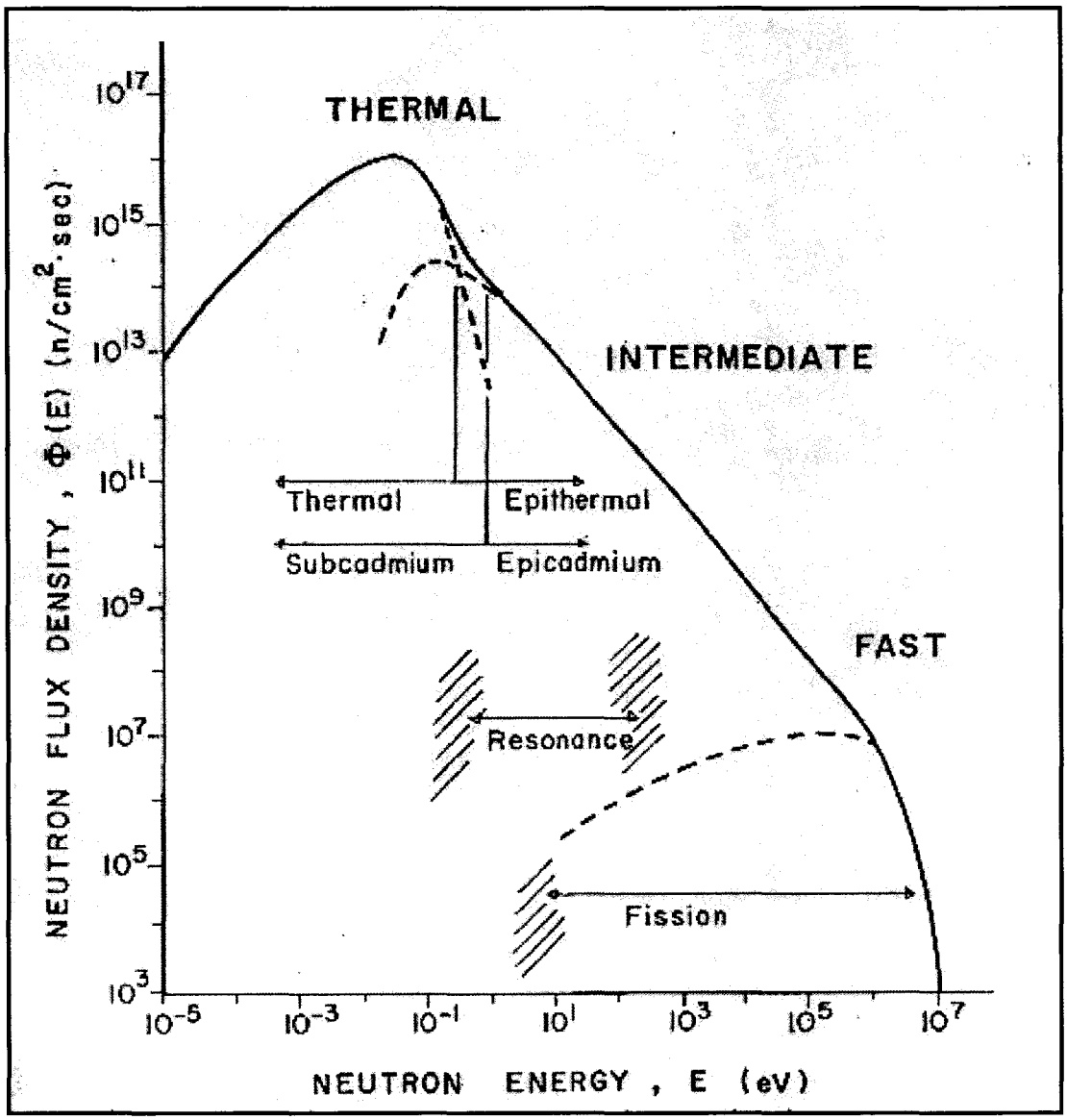

Figure 1.3: *Theoretical representation of neutron fluence rate vs. neutron energy for light water moderated nuclear reactor*

1.3 Introduction to Prompt Gamma Technique and Analysis

Neutron activation analysis is divided into delayed gamma neutron activation analysis (DGNAA) and prompt gamma neutron activation analysis (PGNAA). Delayed gamma neutron activation analysis is actually gamma analysis of the sample, after a sample was bombarded with neutrons. The unstable isotope is formed and that isotope is

counted or examined using spectroscopy techniques, ***after*** the neutron irradiation. Obviously, in this case, the exponential decay of the sample's activity is observed after the irradiation (neutron bombardment). On the other hand, prompt gamma neutron activation analysis (PGNAA) involves the analysis of the sample ***during*** the nuclear reaction (neutron bombardment). When a nucleus captures a neutron, its binding energy is released in the form of cascade of gamma rays. The total energy is usually between 5 and 11 MeV and the time scale of the reaction is typically around 10^{-14} s or less. Obviously, the reactions are very rapid (typical neutron transit limit for nucleus) and gamma emission depends on lifetime of nuclear states. It means that almost every neutron capture by a nucleus yields gamma rays that are potentially usable for analysis **[Failey]**. Comparing the two techniques (prompt gamma and delayed gamma), we observe the fundamental and conceptual difference between them. Simply, for PGNAA, the activity of the sample is constant during the irradiation. It does not depend on half-life of the isotope formed and it is given by simplified the equation **[Tomlinson et al.]**:

$$A = N_0 \varphi \sigma_0 \quad \textbf{eq. 1.8}$$

Where N_0 is the total number of target atoms, φ neutron fluence rate at the site and σ_0 is the thermal cross section for the target atoms. On the other hand, the simplified equation for the activity for DGNAA is given by **[Tomlinson et al.]**:

$$A = N_0 \varphi \sigma_0 \left(1 - e^{-\lambda t_{irr}}\right) e^{-\lambda t_{dec}} \quad \textbf{eq. 1.9}$$

Where t_{irr} is the irradiation time and t_{dec} is the decay time of the new isotope. Note that these equations are presented here in their simplified forms in order to emphasize the difference between PGNAA and DGNAA methods. This project uses more sophisticated

forms of these equations, which will be outlined in later chapters. Considering all these facts, a few logical conclusions can be drawn about prompt gamma techniques.

Firstly, prompt gamma analysis cannot be performed in the reactor core (in our case), nor near the reactor core, because no gamma detector, even with substantial shielding, can withstand large neutron and gamma fields in the reactor core vicinity. For this reason, the reactor neutron source must be extended in the form of a narrow neutron beam, i.e. the neutron beam must be collimated and the experimental site must be located away from the reactor core. This is solved by reactor beam ports. In MNR, there are 6 beam ports, which are extensions of reactor beam tubes. These beam tubes collimate neutrons from the reactor core. Since, the neutrons pass through a large amount of water (moderator) they are highly thermalized, which is very important and useful for this project. In this project, beam port # 4 was used. Furthermore, in beam port # 4, a sapphire filter is located. This filter acts as "*semi permeable membrane for neutrons*". The properties and the shape of the sapphire crystal allow thermal neutrons to reach the collimator, while the majority of higher energy neutrons are backscattered and they do not reach the collimator in the beam port. More detailed information about beam port # 4 and experimental site are given in the next chapter: "**Materials and Methods**".

Secondly, since the prompt gamma irradiation site is located away from the reactor core, the neutron field at the experimental site must be significantly lower than neutron fields in the reactor core. This is true, of course. The neutron fluence rate at the experimental site is expected to be in the order of 10^7 neutrons/cm^{2}s (mostly thermal neutrons), while neutron fluence rates in the reactor core are in the order of 10^{13} neutrons/cm^{2}s. The fact that neutron fluence rate in the beam port is almost a million

times lower than neutron fluence rates in the reactor core, along with the fact that the collimated beam consists of mostly thermal neutrons, makes our experimental site ideal for detecting trace elements like cadmium and gadolinium which posses substantial thermal neutron cross section.

Thirdly, the location and shielding of the detector plays an important role in prompt gamma technique. Ninety degree geometry allows the detector to be located very close to the beam. The detector requires heavy shielding in order to stop scattered neutrons from entering and damaging the detector. The observed sample is located directly in the beam, close to the detector, so it can be irradiated and counted simultaneously.

1.4 Trace Elements and Importance

The main purpose of this project is to try to establish the technique for trace elements detection at MNR at the prompt gamma position. Trace element detection is one of the main research areas at the Medical Physics Unit at McMaster University. Numerous articles have been written on the detection of manganese **[Arnold]**, aluminum **[Pejovic-Milic]**, cadmium **[Carew]**, lead, mercury, uranium **[O'Meara]**, etc, by various techniques. The most frequently used methods are the neutron activation techniques at McMaster Tandem Accelerator and XRF techniques. Furthermore, there are two research projects done at MNR; detection of aluminum **[Palerme]**, and calcium measurements **[Swift-Schultz]**. However, both projects were done at beam port 2, where the experimental settings and beam properties are very different from beam port 4, used for this work. Hence, this project is a pilot study for trace element detection at this

particular experimental site at MNR. With this in mind, the detection of a several trace elements was investigated in order to optimize the system for further and more detailed individual studies of them. As mentioned before in this chapter, the best candidates for prompt gamma analysis are the elements with huge cross sections for thermal neutrons. Those are listed below, along with their thermal cross sections **[Brookhaven; NuDat]**, and their prompt gamma energies of interest **[Brookhaven; CapGam]**:

- ^{113}Cd (20600 ± 400 b; E_γ=558.46 keV)
- ^{155}Gd (60900 ± 500 b; E_γ=199.21 keV)
- ^{157}Gd (254000 ± 815 b; E_γ=181.93 keV)
- ^{199}Hg (2150 ± 48 b; E_γ= 367.94 keV)

The elements listed undergo (n,γ) reactions. Another very interesting reaction that is observed using prompt gamma technique is $^{10}B(n,\alpha)^7Li$ **[Brookhaven; ENDF]**. The thermal cross section for this reaction is 3837 ± 9 b **[Brookhaven; NuDat]** and the gamma energy of interest is 480 keV **[Brookhaven; ENDF]**. In this thesis, the emphasis was on the detection of cadmium and the main experiments were done with cadmium solutions. In this project, the cadmium measurements were established as the calibration measurements. Also, after certain sets of cadmium measurements were done, the boron and mercury measurements were performed. Unfortunately, this project does not include gadolinium measurements.

Furthermore, the properties of the above elements and their metabolism in human body are not investigated here, as this work concerns their detection only. However, it is important to mention that they are highly toxic and they accumulate in the body (especially kidney and liver). Some of them (cadmium) are very hard to eliminate, i.e.

have a relatively long biological half-life. A very good reference for Cd properties is Carew's MSc thesis; chapter I.

CHAPTER II

Materials, Methods and Experimental Procedures

2.1 Description of Prompt Gamma Experimental Site

Detailed descriptions of the prompt gamma experimental site will be given here. The prompt gamma experimental site was built at the beam port # 4, as the extension of beam tube # 4 in MNR. It was designed for irradiation and analysis of small samples that are delivered to the site via pneumatic rabbit system, i.e. automated compressed air insertion system **[Shaw]**. The simple scheme of prompt gamma facility is given below:

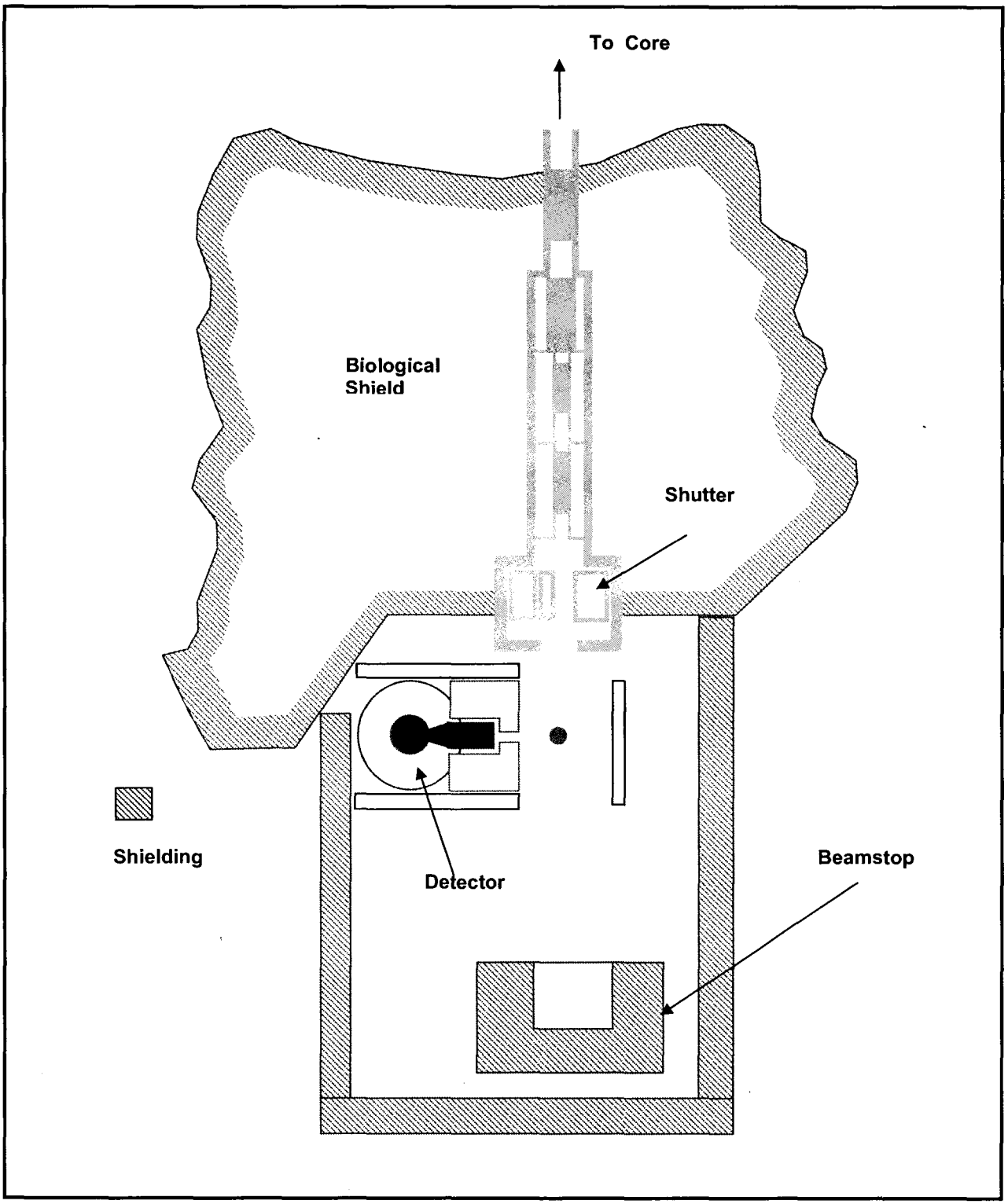

Figure 2.1: *Prompt gamma facility in MNR; Source: MNR webpage*

Furthermore, the simplified scheme of the beam port # 4 components is given below:

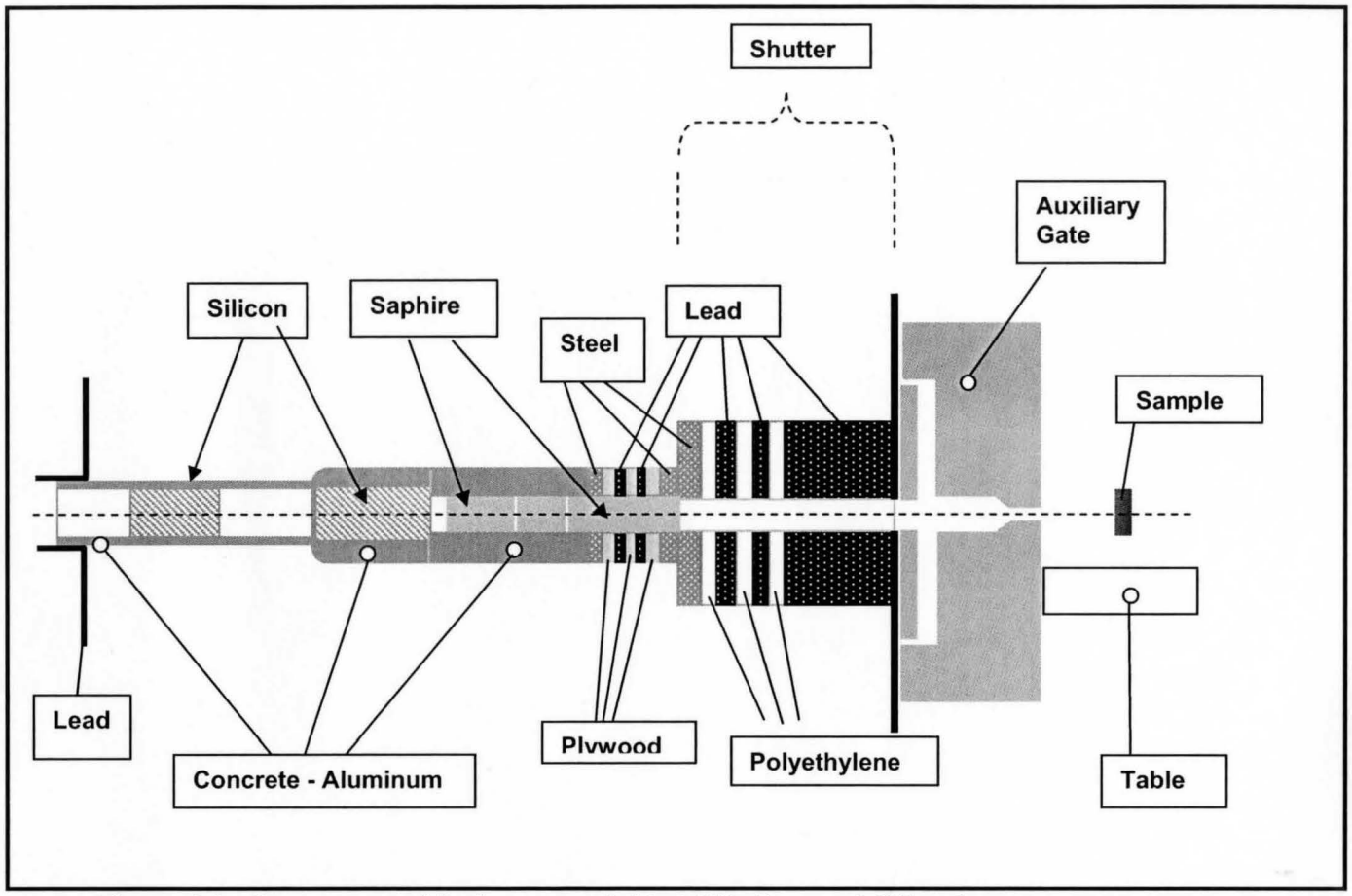

Figure 2.2: *Components of the beam port # 4 in MNR; Source: MNR web page.*

As mentioned in the first chapter, the neutrons are highly thermalized while traveling in the beam tube # 4 toward beam port # 4, because of the large amount of water present. Furthermore, upon entering bp # 4, they pass through two silicon (Si) and two sapphire (Al_2O_3) filters, shown in the figure 2.2. These filters further thermalize the collimated neutron beam.

In order to be a considered for a high energy neutron filter, a material must have certain properties. It must have (de Broglie's) wavelength dependent cross section, such

that the total cross section is low at thermal energies and large at epithermal and higher energies. **[Mildner]**. The efficiency of the neutron filter is defined by the ratio:

$$R = \frac{\sigma_{abs}(E) + \sigma_{inc}(E) + \sigma_{inel}(E) + \sigma_{el}(E)}{\sigma_{tot}} \quad \textbf{eq 2.1}$$

Where: σ_{abs}, σ_{inc}, σ_{inel}, σ_{el} and σ_{tot} are absorption, incoherent, coherent inelastic, coherent Bragg's and total cross section, at thermal neutron energy, respectively and σ_{tot} is averaged between 0 and 10^4 eV (constant value). The lower R value is significant for better quality filters. In the given equation, low value of numerator implies good transmission of neutrons in the wanted thermal energy range, while a large denominator implies strong scattering of epithermal and fast neutrons. **[Nieman]** For sapphire and silicon filters, R values are estimated to be 0.0488 and 0.08 for 0.0253 eV. **[Nieman]**

Furthermore, neutron attenuation through a sapphire filter, as a function of the neutron's de Broglie wavelength is given in the following figure: **[Stamatelatos]**

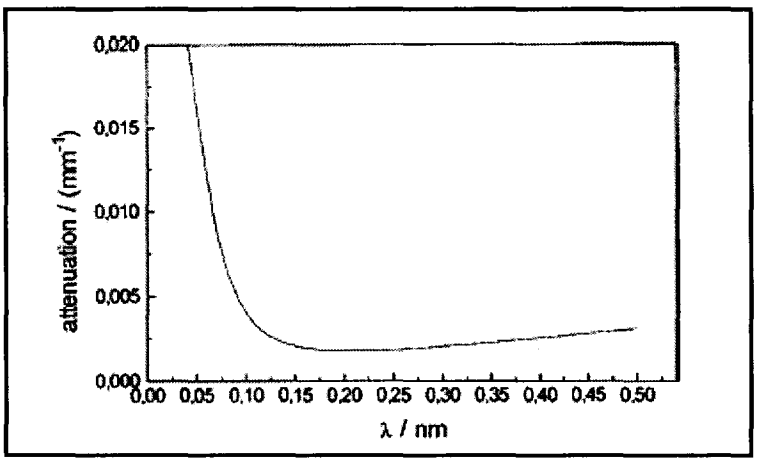

Figure 2.3: *Macroscopic linear attenuation factor for sapphire as a function of wavelength*

The neutron de Broglie wavelength is given by well known de Broglie formula for matter waves:

$$\lambda = \frac{h}{mv} = \frac{h}{p} \quad \textbf{eq. 2.2}$$

Where, h is Planck's constant and m, v, and p are neutron's mass, velocity and momentum, respectively. Knowing that neutron's kinetic energy is given by:

$$E_k = \frac{p^2}{2m} \quad \textbf{eq 2.3}$$

and combining the above two equations, we obtain the relationship between neutron's kinetic energy and corresponding neutron's de Broglie's wavelength in nanometers:

$$E_k = \frac{8.18 \times 10^{-4} eV \times nm^2}{\lambda^2} \quad \textbf{eq. 2.4}$$

According to the above equation, de Broglie wavelength for thermal neutrons (0.0253 eV) is approximately 0.18 nm. As can be seen from figure 2.3, this indicates that thermal neutrons (0.18 nm and higher de Broglie wavelengths) are very poorly attenuated by sapphire crystal, while attenuation for higher energy neutrons (de Broglie wavelengths below 0.18 nm) increases drastically as de Broglie wavelength decreases.

Besides neutron filters, bp # 4 contains significant lead and concrete shielding (see the figure 2.1) in order to minimize induced gamma fields as well as gamma fields from the MNR core itself. At the end of the bp # 4 and at the entrance of the experimental prompt gamma cave there is a beam shutter, so that the neutron beam can be shut off when needed. The prompt gamma cave itself is the bounded space at the lowest level in MNR. It is a box with rectangular shape in its base. The base is just a MNR floor, three vertical sides are made of concrete bricks and the upper base is movable. It consists of two wooden boxes filled up with wax slabs. As mentioned, these two wooden boxes can be moved with the MNR crane in order to allow the access to the

cave. The fourth vertical side is just the reactor pool wall, where the beam entrance is located. A germanium solid state detector is located inside the cave, perpendicular to the neutron beam and it is heavily shielded with wax, boroflex and lead. The figure below illustrates the interior of the prompt gamma cave:

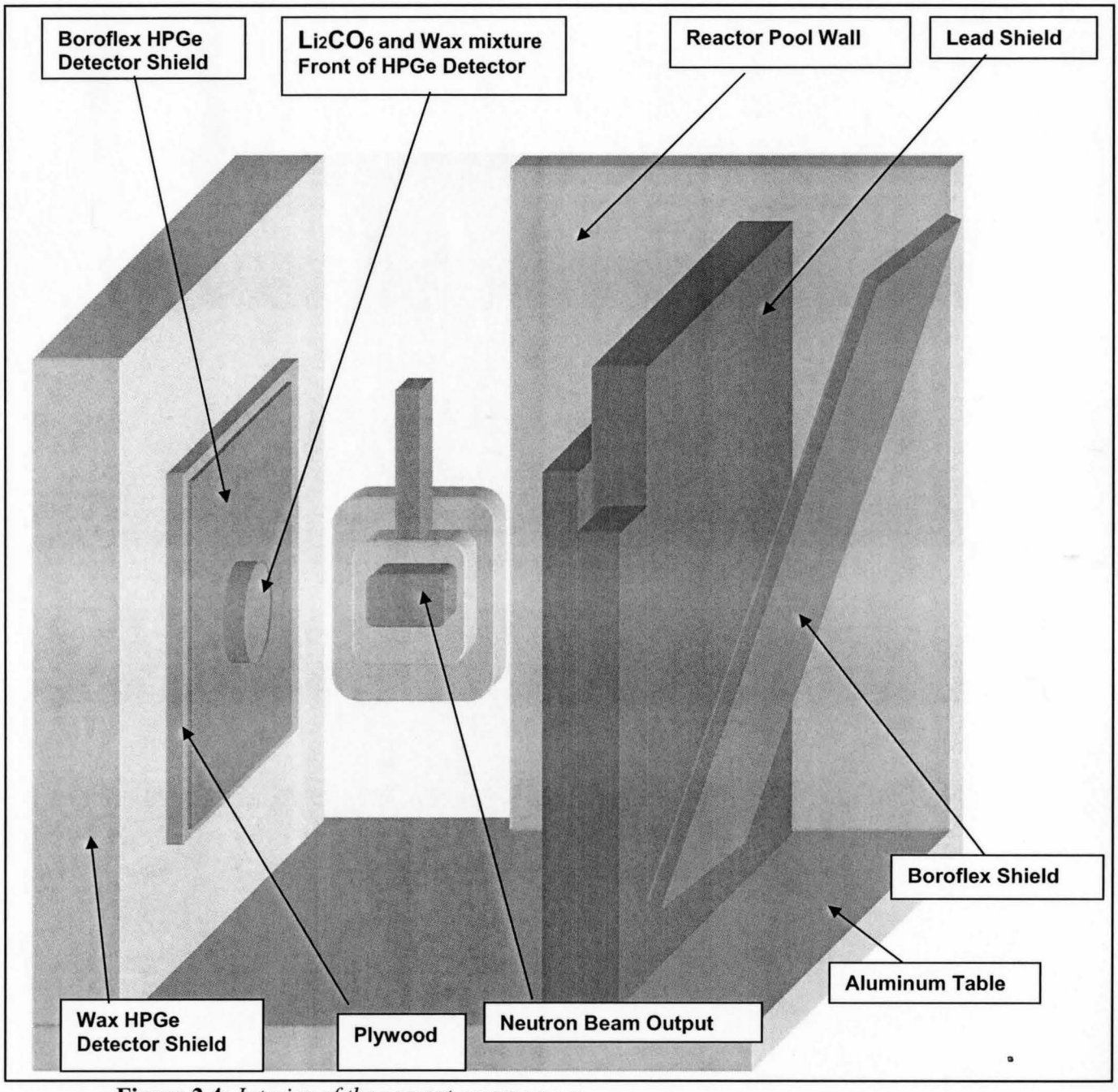

Figure 2.4: *Interior of the prompt gamma cave*

2.2 Foil Irradiation Experiments

The first experimental step was the determination of neutron fluence rates as a function of the neutron energies, i.e. determination of neutron spectra of the collimated neutron beam. The neutron beam at the output has rectangular shape with dimensions 1 inch by 2 inches. Since the vertical beam cross section is relatively small it is assumed that, spatially, the beam is homogenous, therefore, the spatial fluence rate, at any beam vertical cross section ($\varphi(x,y)$) is assumed to be constant. The primary step was the determination of thermal and epithermal neutron fluence rates. This was achieved by irradiation of proper foils at the site. The foils used for this experiment were indium, manganese and gold foils. All the foils were circular in shape and they were irradiated with and without cadmium covers. This was done because cadmium is a thermal neutron filter, i.e. it stops all the neutrons with kinetic energies below the cadmium cut off energy (approximately 0.4 eV) **[Kruger]**. Therefore, when irradiated in cadmium capsule, the foil gets activated only by epithermal neutrons. Therefore, the conclusion can be drawn about the relationship between thermal and epithermal portions of the neutron beam. The following paragraph summarizes the thermal / epithermal foil experiment, with appropriate reaction's resonance integrals and thermal cross sections **[Brookhaven; NuDat]**, and half lives and energies of interest for reaction's products **[Ernest Orlando Lawrence]**:

GOLD FOILS $^{197}Au(n,\gamma)^{198}Au$

$I_{tot} = 1550 \pm 28$ b
$\sigma_0 = 98.65 \pm 0.09$ b at 0.0253 eV
$\tau = 2.69517$ d
E = 411.8 keV

a) Without Cd lining:

mass: 0.195 g
thickness: 2.032×10^{-4}m
purity: 24K
start time: 09:33:29 AM (MNR time), August 22/03
stop time: + 30 min

b) With Cd lining:
mass: 0.223 g
thickness: 2.032×10^{-4}m
purity: 24K
start time: 10:40:44 AM (MNR time), August 25/03
stop time: + 30 min

MANGANESE FOILS $^{55}Mn(n,\gamma)^{56}Mn$

$I_{tot} = 14 \pm 0.3$ b
$\sigma_0 = 13.3 \pm 0.2$ b at 0.0253 eV
$\tau = 2.5785$ h
E = 846.7 keV

a) Without Cd lining:
mass: 0.0461 g
thickness: 5.08×10^{-5}m
purity: 80% Mn-Cu
start time: 07:13:30 PM (MNR time), September 23/03
stop time: + 3 h

b) With Cd lining:
mass: 0.0459 g
thickness: 5.08×10^{-5}m
purity: 80% Mn-Cu
start time: 10:15:48 AM (MNR time), September 04/03
stop time: + 3 h

INDIUM FOILS $^{115}In(n,\gamma)^{116m}In$

$I_{tot} = 2650 \pm 100$ b
$\sigma_0 = 162.3 \pm 0.7$ b at 0.0253 eV
$\tau = 54.29$ min
E = 1097.3 and 1293.6 keV (note: these two observed, because of the highest relative intensities and good statistics).

a) Without Cd lining:
mass: 0.28 g

thickness: 3.048×10^{-4}m
purity: assumed 100%
start time: 10:00:53 AM (MNR time), September 26/2003
stop time: + 5 min

b) With Cd lining:
mass: 0.2188 g
thickness: 3.048×10^{-4}m
purity: assumed 100%
start time: 02:57:24 PM (MNR time), September 29/03
stop time: + 5 min

Also, three figures below illustrate cross section vs. energy for (n,γ) reactions for three foils used, where resonance regions are clearly indicated:

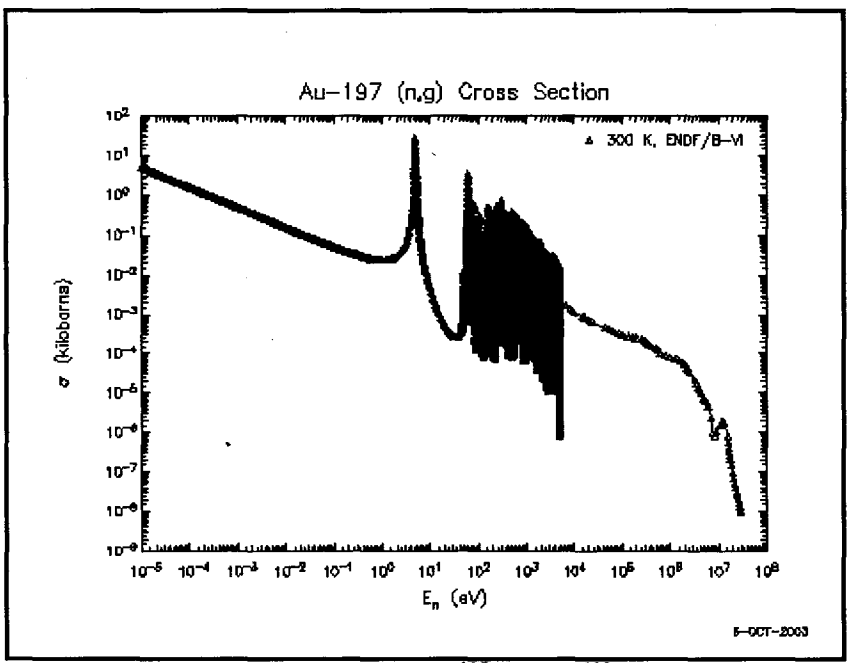

Figure 2.5: *Plotted cross section for $^{197}Au(n,\gamma)^{198}Au$ reaction (Source: ENDF files, Brookhaven)*

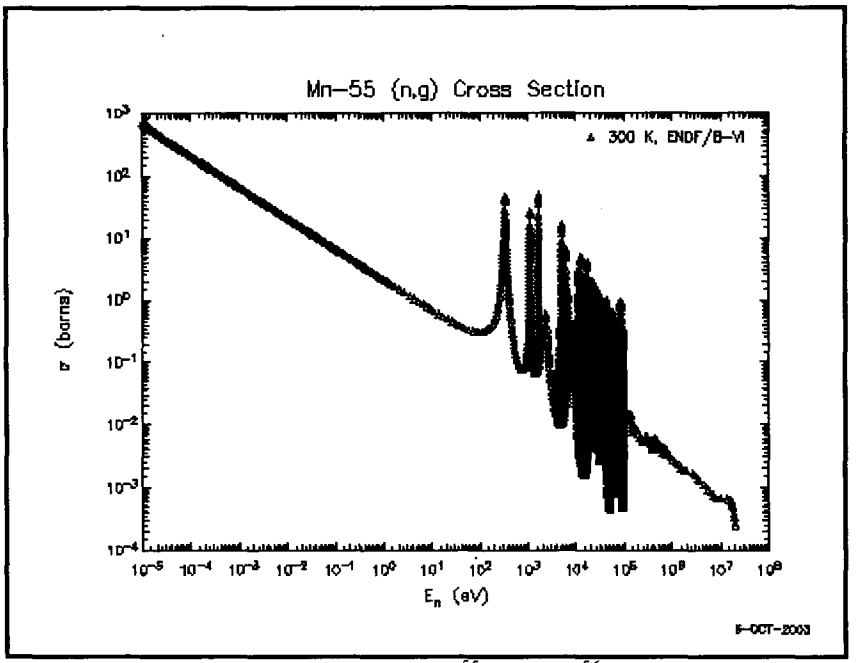

Figure 2.6: *Plotted cross section for $^{55}Mn(n, \gamma)^{56}Mn$ reaction (Source: ENDF files, Brookhaven)*

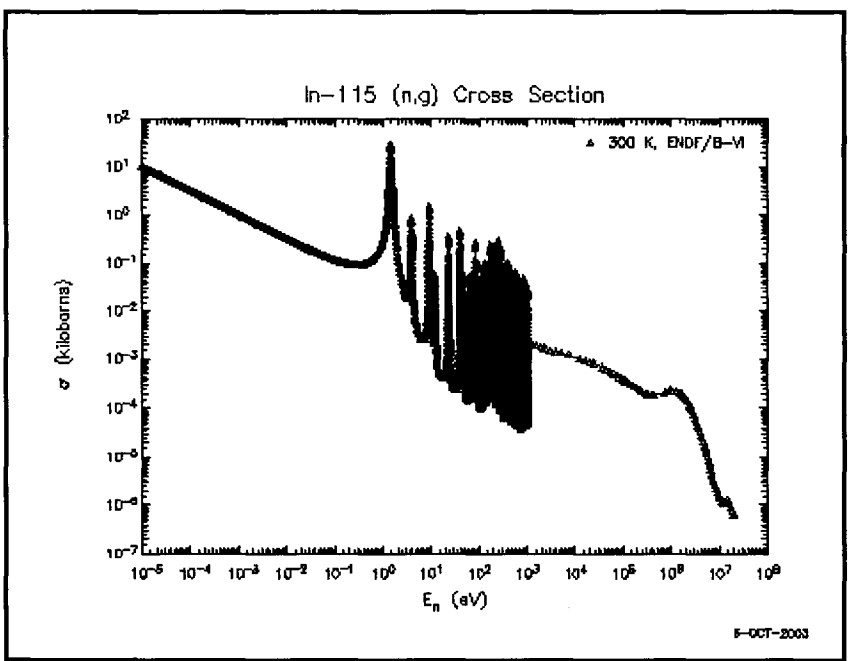

Figure 2.7: *Plotted cross section for $^{115}In(n, \gamma)^{116m}In$ reaction (Source: ENDF files, Brookhaven)*

The foil irradiations were performed using already established rabbit system, which delivers small polyethylene vials in the center of the beam. The foils were in the vials. After appropriate irradiations, the foils were counted in the counting room in the Nuclear Research Building (NRB). The germanium detector (HPGe) was previously calibrated for absolute efficiency at the counting position (position # 1), using europium liquid standard solution. The calibration was performed because we needed absolute values for the neutron fluence rates, therefore we needed absolute value for reaction rates, i.e. absolute activities of the irradiated foils. The detector used for foil counting was solid state germanium detector from NRB lab. The detector was calibrated for the absolute efficiency using the standard source, which is a liquid mixture of antimony - tellurium (^{125}Sb – ^{125m}Te) and europium (^{154}Eu and ^{155}Eu) with the mass of 5.236g. The source was established on May 1, 1983 and energy range was from 27.4 to 1596.5 keV. The source was established by "National Bureau of Standards Certificate" (Standard Reference Material, SRM 4276B-198). The source was enclosed in glass ampoule. Obviously, the energy range covers nicely all the peaks from the foils used in thermal-epithermal neutron detection. The standard source has 18 lines that are available for calibration. For this particular calibration 16 lines were used, ranging from 86.6 to 1596.5 keV. Half-lives for these isotopes are **[Ernest Orlando Lawrence]**: 1006.743 days, 3136.445 days and 1737.8015 days for ^{125}Sb, ^{154}Eu and ^{155}Eu, respectively. The standard was counted on October 29, 2003, for 15 hours live time, in order to get better statistics for some ^{125}Sb peaks.

The results provided the information about thermal and epithermal neutron fluence rates. However, this could not give us any knowledge about fast neutrons in the beam. The original hypothesis is that the portion of fast neutrons in the beam is negligible, but this needed to be confirmed. This was done by another set of experiments, irradiation of threshold foils. Those are the materials that have high reaction cross section for fast, rather than thermal neutrons.

The method of finding the fast neutron fluence rate is very similar to the method of finding the thermal neutron fluence rate. The activation of various (available) foils was performed. Obviously, all the threshold foils were enclosed in cadmium caps. This is because we wanted to prevent any thermal neutron capture. There were a few commercially available foils that were used in this experiment. Those are listed below along with their experimental threshold energies **[Reactor Experiments Inc.]**:

$^{103}Rh(n,n')^{103m}Rh$.....neutron energy: 0.8 MeV

$^{115}In(n,n')^{115m}In$.....neutron energy: 1.2 MeV

$^{232}Th(n,f)^{140}Ba$.....neutron energy: 1.4 MeV

$^{58}Ni(n,p)^{58}Co$.....neutron energy: 2.8 MeV

$^{54}Fe(n,p)^{54}Mn$.....neutron energy: 3.1 MeV

The foils listed above were manufactured by ***"Reactor Experiments"*** company, located in New Mexico. These foils have very high purity (more than 99 %).

Every nuclear reaction: X(a,b)Y has Q value (energy released) **[Krane]**:

$$Q = (m_X + m_a - m_Y - m_b)c^2 \quad \textbf{eq 2.5}$$

Where different m's are the rest masses of the nuclei involved in reaction. The Q value may be positive, negative or zero. If Q>0, the reaction is exothermic (no energy is

required for this reaction) **[Krane]**. All thermal neutron absorption reactions are exothermic, because the kinetic energy of thermal neutron (projectile) is negligible, 0.0253eV. If Q<0, the reaction is said to be endothermic (energy is required for the reaction to take place) **[Krane]**. In this case, we require projectile particles (neutrons in our case) with a significant amount of kinetic energy (MeV range). Also, in order for an endothermic reaction to take place, there must be a certain energy threshold, under which the reaction is not possible. That projectile kinetic energy threshold is given by **[Krane]**:

$$T_{th} = (-Q)\frac{m_Y + m_b}{m_Y + m_b - m_a} \qquad \textbf{eq 2.6}$$

Of course, this is a theoretical threshold, which is different from practical energy threshold. The practical thresholds for the reactions used in this project are taken from the reaction foil kits and they are listed above. These practical thresholds are in close agreement with ENDF files. Those reaction energy thresholds are pictured below.

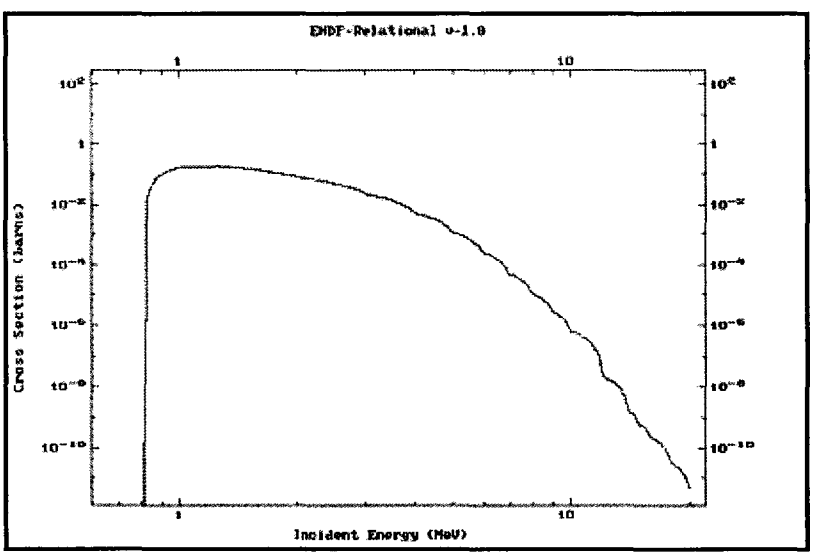

Figure 2.8: Cross *section vs incident neutron energy for* $^{103}Rh(n,n')^{103m}Rh$ *threshold reaction; Source: ENDF, Brookhaven, JENDL-3.3 library*

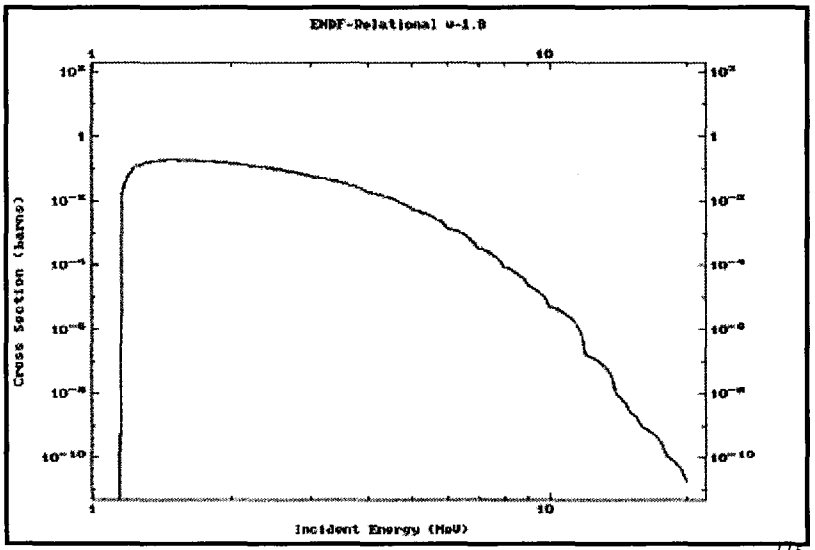

Figure 2.9: Cross *section vs incident neutron energy for* $^{115}In(n,n')^{115m}In$ *threshold reaction; Source: ENDF, Brookhaven, JENDL-3.3 library*

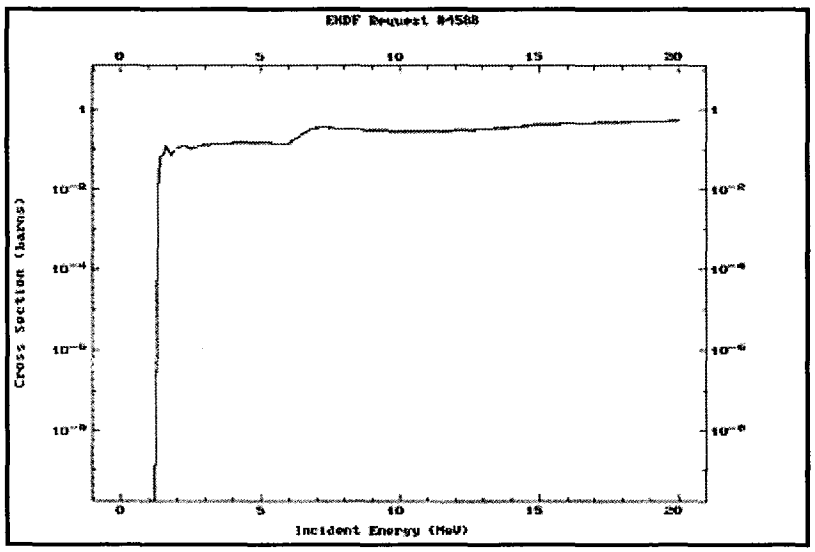

Figure 2.10: Cross *section vs incident neutron energy for* $^{232}Th(n,f)^{140}Ba$ *threshold reaction; Source: ENDF, Brookhaven, JEF-2.2 library*

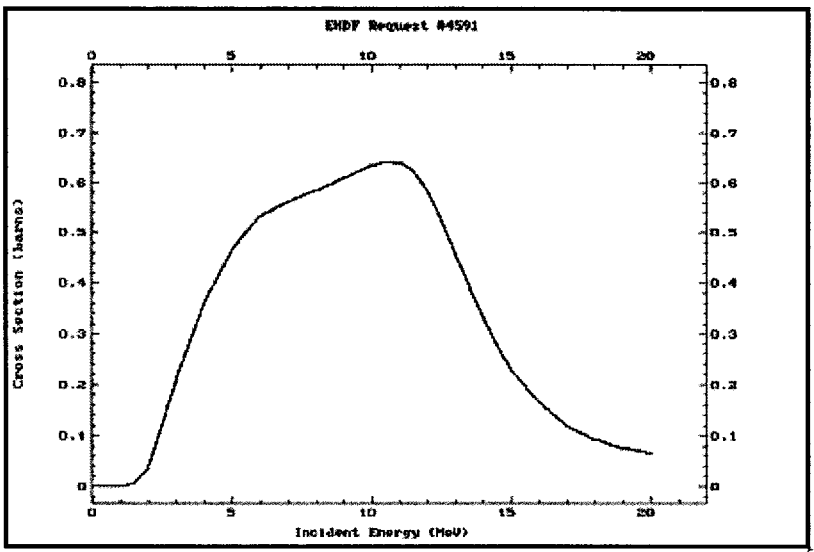

Figure 2.11: Cross *section vs incident neutron energy for* $^{58}Ni(n,p)^{58}Co$ *threshold reaction; Source: ENDF, Brookhaven, JENDL-3.3 library*

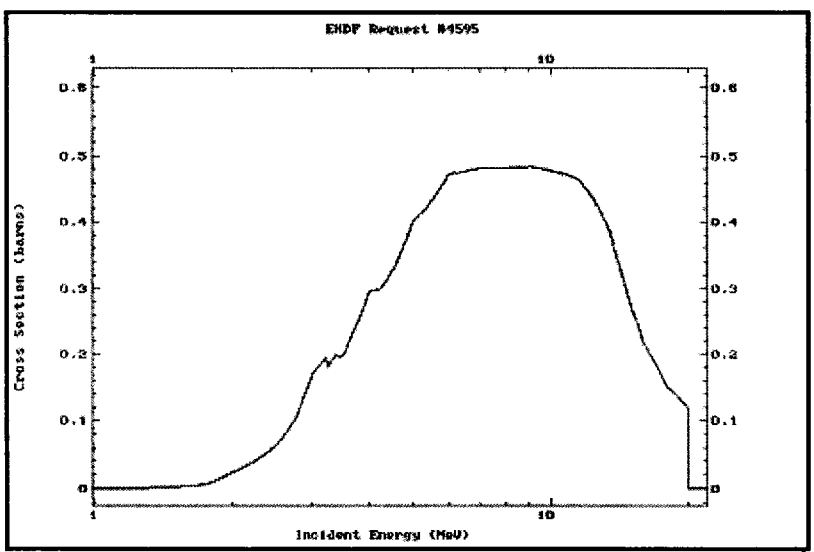

Figure 2.12: Cross *section vs incident neutron energy for* $^{54}Fe(n,p)^{54}Mn$ *threshold reaction; Source: ENDF, Brookhaven, ENDF B-VI library*

2.3 Prompt Gamma Irradiation Experiments: Preliminary Irradiations and Phantom Irradiations

Before any phantom irradiation took place at the experimental site, it was necessary to explore the site further, because no information was available about it. In

other words it was necessary to establish background with MNR on and off. Furthermore it was necessary to calibrate the system for spectroscopy amplifier's low and high gain. The main components of the detection system are germanium detector (HPGe), GMX-30190 Series, manufactured by *Ortec*; Spectroscopy amplifier, model 2020, manufactured by *Canberra*; ND580 ADC manufactured by *Nuclear Data Inc.*; ND599 Loss-Free Counting Module (LFC), manufactured by *Nuclear Data Inc*, as well. This LFC provides real-time correction of system counting losses. Also, there is appropriate MCA and the software associated with it.

For calibration and background experiments, few materials were used: water, quartz, calcium chloride ($CaCl_2$), sodium chloride (NaCl), graphite, iron powder and polycarbonate materials. All these materials were irradiated at the experimental site. They were delivered to the irradiation position using already established pneumatic rabbit system and all the materials were enclosed and thermally sealed in small polyethylene vials. Furthermore, there were lots of runs of empty vial, empty irradiation position (MNR on and off) and there were some overnight runs.

When the background was established and the system was calibrated for low and high gain, the phantom irradiation took place. The experimental site was changed and modified in order for these phantoms to fit nicely, 90 degrees both to the detector and the neutron beam. They were all centered to be exactly in the beam, using appropriate plywood holders. The phantoms had to be inserted manually, using a specially designed aluminum long pole. During the irradiation the prompt gamma cave cover was open, with the phantom in the beam. The Health Physics department allowed the irradiation to take place with the cover open, because the gamma and neutron dose survey was done

before any irradiation took place. It was found out that gamma and neutron dose rates from the phantom scatter were negligible. There were 7 polyethylene phantoms (plastic bottles) and they had different volumes: 30 ml, 60 ml, 125 ml, 250 ml, 500 ml, 1 l and 2 l. The cadmium compound $CdCl_2 \times 5/2\ H_2O$ was dissolved in the water and it was used for Cd detection, Cd linear calibration of the system and establishment of minimum Cd detection limit (MDL). The concentration of Cd in the phantoms varied from 0 to 50 ppm. Furthermore, the minimum detection limits were established for mercury and boron, using the smallest polyethylene vials, based on Cd results previously obtained.

CHAPTER III

Experimental Results and Analysis

3.1 Simple Site's Testing and Background Radiation

Three irradiations were done for background spectrum at high gain spectroscopy amplifier gain (24.6), energy range up to 2.8MeV. The first irradiation was only sample holder without sample vial. Reactor was operated at 3MW and irradiation lasted for 5h. Gross count rate was 611.52 ± 0.18 c/s. Five significant prompt gamma peaks were observed. See the table below:

sample holder only		
line (keV)	count rate(c/s)	error (%)
510.22	8.42	0.73
582.74	1.02	3.66
801.74	0.50	5.74
1630.55	1.22	2.15
2218.68	0.66	2.92

Table 3.1: *Significant activities due to prompt gamma of sample holder, without the polyethylene vial*

The second irradiation was an empty sample vial (polyethylene). The reactor was at 3MW and irradiation lasted for 10h. Count rate was 1560.7 ± 0.2 c/s. In this case we had 7 significant prompt gamma peaks. This is different from previous irradiation, due to presence of single and double escapes from hydrogen (polyethylene vial). See the table below, for the peaks.

Empty sample vial		
line (keV)	count rate (c/s)	Error (%)
510.14	14.76	0.42
582.64	1.17	3.22
801.59	0.53	5.83
1198.92	4.72	0.84
1630.21	1.43	2.26
1708.61	4.63	0.96
2218.34	56.76	0.14

Table 3.2: *Significant activities due to prompt gamma of sample holder, with empty polyethylene vial*

This little experiment showed that the presence of small polyethylene vial increased hydrogen line at 2.2 MeV about 100 times and the gross count rate by 2.5 times approximately. Also, the annihilation peak is increased almost two times. These facts are surprising, because one would expect that scattered neutrons captured by paraffin and wax shielding would significantly contribute the most to those lines. Obviously, this is not true. Apparently, the polyethylene vial, located *directly in the beam* caused these big increments in the counts. This showed us that the beam was well collimated and the fluence rate of neutrons, scattered of the shielding is minimal (negligible). Also, these facts showed that materials with high concentration of hydrogen (organic materials), located directly in the beam will produce huge prompt gamma hydrogen peak at 2.2 MeV. This cannot be avoided, because the final goal of this project would be the organic material (phantom, or even person), located directly in the beam. Furthermore, good outcome is the fact that we would not have to worry about contribution of that massive shielding to the hydrogen line and background, because it is negligible, obviously.

The third run was 55 h, when reactor was shut down (during the weekend). Gross count rate was only about 0.1 c/s, ie., the detector picked up only 19868 events over the period of 55 hours. In this case, no significant features (gamma lines) were observed.

This means that the detector is shielded very well and that the outside events would not interfere with our measurements and counts.

3.2 Energy Calibration of the Counting System at High and Low Spectroscopy Amplifier Gain; 30 and 6 respectively

The Calibration at lower spectroscopy amplifier (Canberra, model 2020) gain was performed in order to calibrate the system up to about 12 MeV. For this exercise Fe powder sample was used and the conversion gain on ADC (ND-580) was 8 K channels. Natural iron consists of four stable isotopes with the following fractions: ^{54}Fe (5.845 %), ^{56}Fe (91.754 %), ^{57}Fe (2.119 %) and ^{58}Fe (0.282 %). **[Brookhaven; Table of Nuclides]** For the calibration at low gain, the most prominent lines of ^{54}Fe and ^{56}Fe were used, as well as annihilation peak and prominent hydrogen peak at 2.2 MeV. The thermal neutron capture cross sections for ^{54}Fe and ^{56}Fe are (2.25 ± 0.18) b and (2.59 ± 0.14) b, respectively. **[Brookhaven; NuDat]** The following table and graph below, summarize the energy calibration of the system at low gain (6). Note that all the information about lines' intensities and correct energies are taken from **Brookhaven** web site, as well, CapGam section. Note that the lines' intensities are given relative to the most intense prompt gamma line for the particular nuclide. For example, the most prominent prompt gamma line for ^{56}Fe is at 7631.06 keV, while the second one is at 7645.58 keV with intensity of 86 % relative to the 7631.06 keV line.

Calibration Fe powder		(gain = 6)		relative int
channel	meas (keV)	calc (keV)	lines	%
298.28	511	510.99	annihilation	100
1129.73	1725.29	1725.4	^{56}Fe (1)	21.72
1470.61	2223.3	2223.17	H	100
2836.68	4217.98	4218.03	^{56}Fe (2)	23.34
4002.29	5920.35	5920.32	^{56}Fe (3)	33.1
5173.68	7631.18	7631.06	^{56}Fe (4)	100
5183.71	7645.58	7645.71	^{56}Fe (5)	86.21
6314.53	9297.8	9297.8	^{54}Fe (1)	100

Table 3.3: *Prompt gamma system energy calibration up to 12 MeV using Fe powder*

As is obvious from the table above, two close ^{56}Fe lines at 7631 and 7645 keV were used, along with the most prominent line of ^{54}Fe at 9.3 MeV. Also, at lower energies, the hydrogen line was used at 2223.26 keV, along with two ^{56}Fe lines at 4.2 MeV and 5.9 MeV and finally, the annihilation line was used. These 8 lines gave us a calibration curve with the equation: E (keV) = 1.4604(ch #) + 75.343 (excel estimate) and the graph is linear, as it is obvious ($R^2 = 1$). See the graph below.

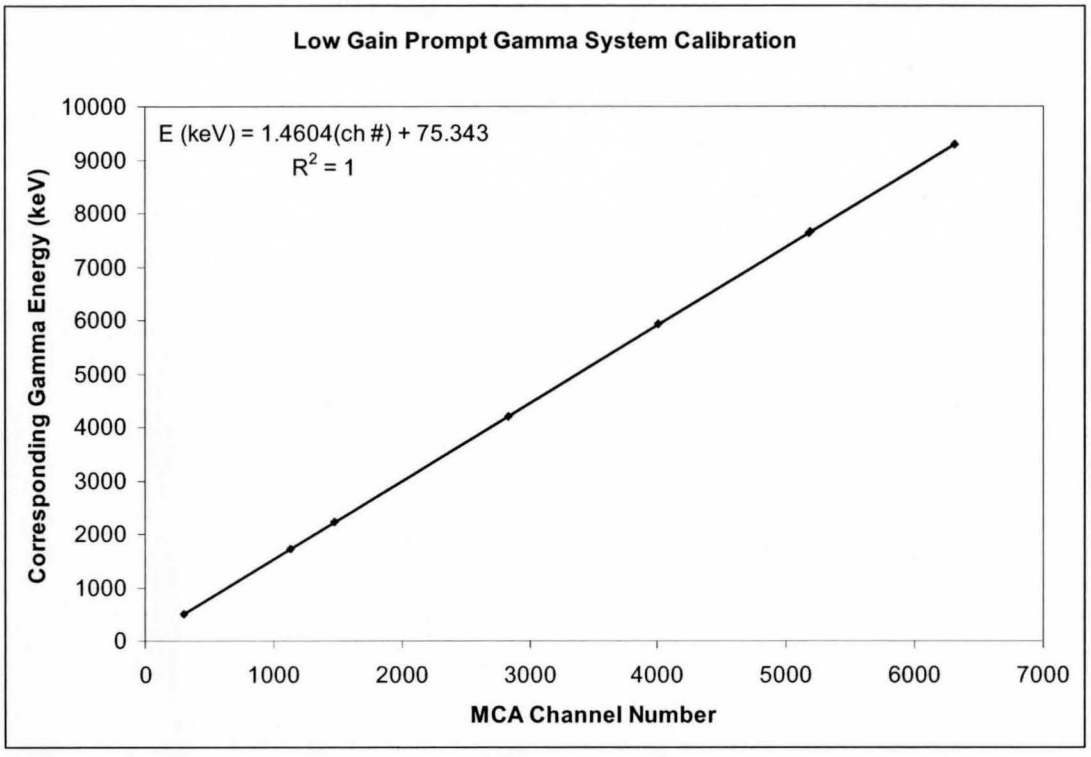

Figure 3.1: *Low spectroscopy amplifier gain (6) prompt gamma system energy calibration*

The energy calibration at high spectroscopy amplifier gain was done similarly. The spectroscopy amplifier gain was set up to 10 and conversion gain on ADC was set up to 4 K channels. The following table, along with the graph summarizes the result.

Calibration Fe powder		(gain = 30)		relative int
channel	meas (keV)	calc (keV)	lines	%
606.17	352.36	352.36	Fe (1)	32.76
975.35	558.46	558.46	Cd	100
2867.51	1612.78	1612.78	Fe (2)	18.55
3069.16	1725.29	1725.29	Fe (3)	21.72
3962.11	2223.3	2223.3	H	100

Table 3.4: *Prompt gamma system energy calibration up to 2.3 MeV using Fe powder*

The graph corresponding to the above table is given below:

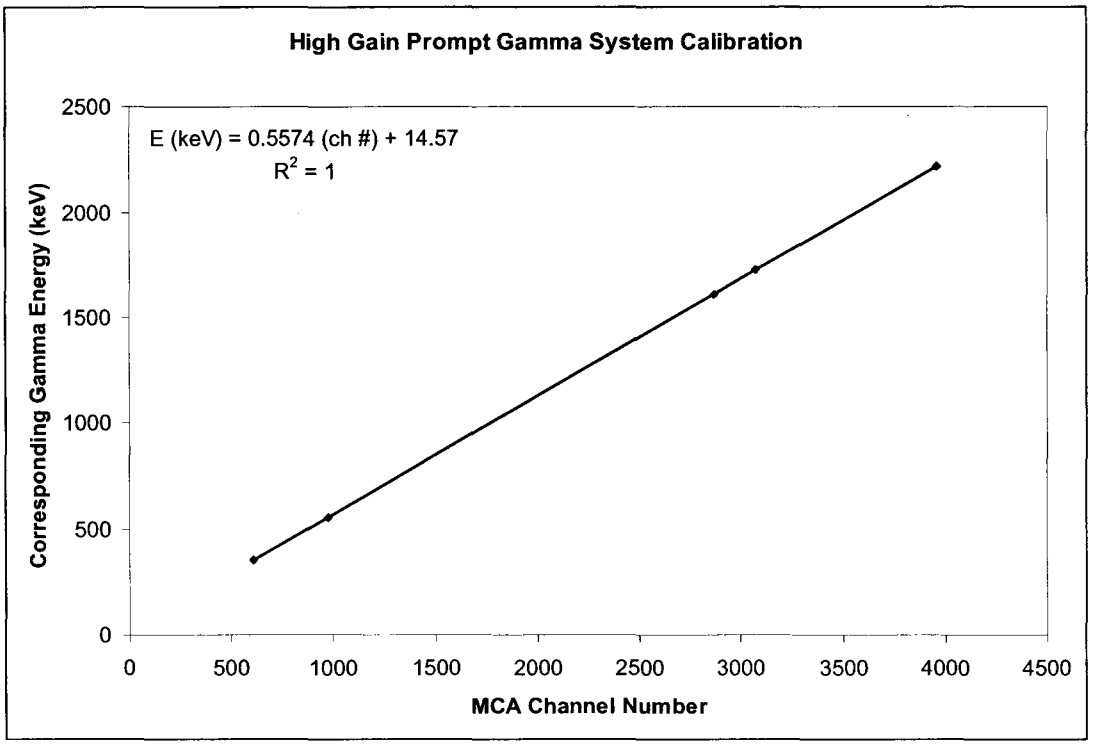

Figure 3.2: *High spectroscopy amplifier gain (30) prompt gamma system energy calibration*

Again, obviously, from the graph, equation and R^2 value, the relationship is strictly linear.

3.3 Irradiations of Other Probes (Materials)

Furthermore, a few other samples were irradiated using the settings from above and some important features were noticed based on these samples. Those samples were: quartz, water, polycarbonate, empty sample vial, graphite and calcium chloride ($CaCl_2$). They were done in order to check calibration and to see the prompt gamma features at different energies. Another interesting feature of concern is the background count associated with these materials and the area under hydrogen peak. The point was to try to minimize both, if possible. Previous irradiations at higher gain showed that the hydrogen

peak was predominantly due to plastic vial. See the above results. When empty plastic vial was irradiated at lower gain, the net count rate due to hydrogen was 49 c/s. Furthermore, with a water sample net count hydrogen rate was 104 c/s. This seems logical, because in this case our source of hydrogen was the water, besides the same plastic vial, so the area under hydrogen peak (2.2 MeV) was much higher. Graphite and quartz gave 59 and 60 c/s, respectively. The reason for about 17 % increased hydrogen activity, compared to empty vial is probably due to the higher thermal neutron scatter rate in graphite and quartz, compared to water. In particular, the graphite and quartz have relatively high thermal neutron scatter cross sections, (4.746 ± 0.002) b and (1.992 ± 0.006) b, respectively **[Brookhaven; NuDat]**. Therefore, those scattered neutrons will be further absorbed by the huge wax shield and that is the source of the increased count rate of 2.2 MeV hydrogen prompt gamma line. Furthermore, the polycarbonate sample gave the similar results as water. Finally, when calcium chloride was irradiated in the polyethylene vial, at low spectroscopy amplifier gain, a huge number of chlorine peaks was observed. Apparently, no calcium peaks were detected simply because ^{40}Ca thermal neutron cross section is (0.410 ± 0.002) b and ^{35}Cl thermal neutron cross section is (43.6 ± 0.4) b. **[Brookhaven; NuDat]** Therefore, the ratio in thermal neutron cross sections is approximately 100 times in the favor of chlorine. All those chlorine peaks, spanning the complete spectrum, to about 8.58 MeV (last chlorine prompt gamma line **[Brookhaven; CapGam]**), greatly confirmed the system energy calibration at low gain. There were about 80 prominent chlorine lines detected, along with their single and double escape peaks.

3.4 The Foil Irradiation Experiment and Determination of the Neutron Energy Spectrum at the Prompt Gamma Irradiation Site

The detailed procedures, foils' properties and experimental methods for these experiments are given in the previous chapter; section 2.2. After irradiation, each foil was counted several times using MCA equipment in the NRB lab and simple time corrections for the activities were performed in order to get activities right after the irradiation. This is illustrated below, through the equations 3.1 to 3.5. The counting position for each foil was closest to the detector. Manganese and indium foils were circular in shape with approximately equal radii and gold foils were rectangular in shape and they were all enclosed in polyethylene vials, while counted. Also the absolute efficiency of the detector, at this stage was not important, because in our calculations, we compared the foils made of the same material, irradiated with and without cadmium caps and counted at the same position. This will become evident after simple math is observed. See the below equations, 3.1 to 3.5 for the details.

During the neutron bombardment, two processes occur in material; an unstable isotope is formed and the same isotope decays. We call these processes production and decay. Right after the bombardment, production process stops, but decay process continues. This process is described by simple exponential decay equation (see the equation 3.2). In this part of the experiment we aim for activity A_0, which describes the activity of the sample just after the neutron irradiation, because we compare this activity for the same foils (covered and not covered with cadmium cap).

The number of counts recorded under a certain peak, using MCA equipment and divided by the detector absolute efficiency at that peak energy is the time integral of total

activity of the sample, integrated from the beginning to the end of counting period (from t_1 to t_2):

$$\frac{M}{I_\gamma \varepsilon} = \int_{t_1}^{t_2} A(t)dt \qquad \textbf{eq 3.1}$$

Where:

M = net number of counts recorded using MCA equipment

ε = the absolute efficiency of the detector

We know theoretically, that activity is exponential decay function:

$$A(t) = A_0 e^{-\frac{\ln 2}{\tau} t} \qquad \textbf{eq 3.2}$$

Where:

τ = half-life of isotope, of interest

A_0 = activity of the sample just after the neutron bombardment.

This is actually what we compare; A_0 for various foils (irradiated with or without cadmium cap). It is very important to keep in mind at this point that the same foils (with and without Cd cap) have to be irradiated under the same conditions for the same amount of time, in order for them to experience the same neutron field. Putting this further into equation we get A_0:

$$A_0 = \frac{M}{I_\gamma \varepsilon \int_{t_1}^{t_2} e^{-\frac{\ln 2}{\tau} t} dt} \qquad \textbf{eq 3.3}$$

Finally, solving the definite integral, we get:

$$A_0 = \frac{M \ln 2}{\tau \varepsilon I_\gamma \left[e^{-\frac{\ln 2}{\tau} t_1} - e^{-\frac{\ln 2}{\tau} t_2} \right]} \qquad \textbf{eq 3.4}$$

As it was said, above, comparing two count rates (with and without cadmium caps), ln2, τ, ε and I_γ will cancel from the equation, so throughout our calculations, we deal only with quantity C and C_{Cd}. These are short for counts of the foil with and without cadmium cap, respectively. Therefore:

$$C = \frac{M}{e^{-\frac{\ln 2}{\tau}t_1} - e^{-\frac{\ln 2}{\tau}t_2}} \qquad \textbf{eq 3.5}$$

When the foil is irradiated without cadmium cap, the rate of reaction is given by **[Medical Physics 4R06]**:

$$R = \sigma_0 \varphi_{th} + I_{tot} \varphi_{res} \qquad \textbf{eq 3.6}$$

Where:

σ_0 = thermal cross section of the irradiated material

φ_{th} = thermal neutron fluence rate

I_{tot} = total resonance integral of the material

φ_r = resonance neutron fluence rate.

With the presence of cadmium cap, thermal neutrons cannot pass through, so the reaction rate is simply given by **[Medical Physics 4R06]**:

$$R_{Cd} = I_{tot} \varphi_r \qquad \textbf{eq 3.7}$$

Now, R and R_{Cd} are simply given by:

$$R_{Cd} = A_{Cd} \varepsilon \qquad \textbf{eq 3.8}$$

$$R = A \varepsilon \qquad \textbf{eq 3.9}$$

Where, A_{Cd} and A are total count rates of the samples irradiated with and without cadmium cap, respectively. Putting this into the equation, we get:

$$\frac{\sigma_0\varphi_{th} + I_{tot}\varphi_r}{I_{tot}\varphi_r} = \frac{A}{A_{Cd}} = \frac{C}{C_{Cd}} \qquad \textbf{eq 3.10}$$

And rearranging terms, we get:

$$\frac{\sigma_0\varphi_{th}}{I_{tot}\varphi_r} + 1 = \frac{C}{C_{Cd}} \qquad \textbf{eq 3.11}$$

Finally, our desired equation reads:

$$\frac{\varphi_r}{\varphi_{th}} = \frac{\sigma_0}{I_{tot}\left(\frac{C}{C_{Cd}} - 1\right)} \qquad \textbf{eq 3.12}$$

This equation gives us the relationship between resonance and thermal fluence rates. Using this equation, equation for C and C_{Cd} time correction and information on three kinds of foils, given in the chapter 2, we obtain the next results:

i) Gold Foil Results:

It is important to clarify a few things and entries in the following table, so that the confusion is avoided. Those will be applied to the other tabular results given in this section as well. Since the foils were with slightly different masses, the mass correction was applied to the number of counts of the lighter foil. Simply, the values of C or C_{Cd} (from equation 3.5) of the lighter foil was multiplied by the factor: (mass of heavier foil / mass of lighter foil). The error propagation and the way of calculation are given in appendix B4. Finally, the results are given below in tabular form.

Gold Activation (w/o Cd capsule) 0.195 g								
	# of counts	error	t_1 (min)	t_2 (min)	CR	δCR	mass norm	error norm
count # 1	368926	611	17	47	69250472	114780	79194129	131261
count # 2	367640	611	53	83	69454205	115380	79427116	131948
						sum	158621245	186117
						average	79310623	93059
Gold Activation (w Cd capsule) 0.223 g								
	# of counts	error	t_1 (min)	t_2 (min)	CR	δCR	mass norm	error norm
count # 1	2883	70	88	118	548069	13254	548069	13254
count # 2	2729	69	124	154	522139	13269	522139	13269
						sum	1070208	18754
						average	535104	9377
OBTAINED RESULTS								
σ_0 (b)	$\delta\sigma_0$ (b)	I_{tot} (b)	δI_{tot} (b)		φ_r/φ_{th}	$\delta(\varphi_r/\varphi_{th})$		
98.65	0.09	1550	28		0.000432	1.1E-05		

Table 3.5: *Summary of the gold foils activation results and calculations*

Averaging all values for φ_r/φ_{th} for, along with its errors, we obtain average φ_r/φ_{th} for gold foils of $\mathbf{(4.32 \pm 0.11) \times 10^{-4}}$.

ii) Manganese Foil Results:

The next table will give the manganese foil results:

Mn Activation (w/o Cd capsule) 0.0461 g								
	# of counts	error	t_1 (min)	t_2 (min)	CR	δCR	mass norm	error norm
count #1	112843	342	705	735	21119005	63945	21119005	63945
count #2	96243	315	741	771	21164874	69360	21164874	69360
count #3	145545	389	788	848	21080045	56297	21080045	56297
count #4	57832	246	853	883	21005882	89364	21005882	89364
						sum	84369806	141616
						average	21092452	35404
Mn Activation (w Cd capsule) 0.0459 g								
	# of counts	error	t_1 (min)	t_2 (min)	CR	δCR	mass norm	error norm
count # 1	5386	84	54	114	29104	453	29230	455
count # 2	1941	52	138	168	28640	762	28765	765
						sum	57995	890
□						**average**	28998	445
OBTAINED RESULTS								
σ_0 (b)	$\delta\sigma_0$ (b)	I_{tot} (b)	δI_{tot} (b)		φ_r/φ_{th}	$\delta(\varphi_r/\varphi_{th})$		
13.3	0.2	14	0.3		0.001308	4.0E-05		

Table 3.6: *Summary of the manganese foils activation results and calculations*

Again, averaging all the results from this table, we obtain: φ_r/φ_{th} for manganese of

$(13.08 \pm 0.4) \times 10^{-4}$.

iii) ***Indium Foil Results (1097.3 keV line):***

Indium activation (w/o Cd capsule) 0.28 g 1097.3 keV line								
	# of counts	error	t_1 (min)	t_2 (min)	CR	δCR	mass norm	error norm
count # 1	104385	346	268	298	10045064	33299	10045064	33299
count # 2	64698	274	306	336	10113694	42832	10113694	42832
count # 3	39628	222	345	375	10192256	57134	10192256	57134
count # 4	26332	180	377	407	10190307	69492	10190307	69492
count # 5	17426	147	409	439	10146971	85789	10146971	85789
						sum	50688293	135634
						average	10137659	27126.801
Indium activation (w Cd capsule) 0.2188 g 1097.3 keV line								
	# of counts	error	t_1 (min)	t_2 (min)	CR	δCR	mass norm	error norm
count # 1	9240	109	25	55	39957	473	51133	605
count # 2	6106	90	59	89	40757	599	52156	766
count # 3	4109	74	90	120	40744	738	52141	945
count # 4	2733	61	122	152	40776	909	52182	1163
						sum	207611	1789
						average	51903	447
OBTAINED RESULTS								
σ_0 (b)	$\delta\sigma_0$ (b)	I_{tot} (b)	δI_{tot} (b)		φ_r/φ_{th}	$\delta(\varphi_r/\varphi_{th})$		
162.3	0.7	2650	100		0.000315	1.2E-05		

Table 3.7: *Summary of the indium foils (1097.3 keV line) activation results and calculations*

Averaging indium results (line 1097.3 keV), we obtain: $\varphi_r/\varphi_{th} = \mathbf{(3.15 \pm 0.12) \times 10^{-4}}$.

iv) Indium Foil Results (1293.6 keV line):

Indium activation without Cd foil 0.28 g 1293.6 keV line								
	# of counts	error	t_1 (min)	t_2 (min)	CR	δCR	mass norm	error norm
count #1	127838	367	268	298	12301968	35323	12301968	35323
count #2	78882	289	306	336	12330960	45108	12330960	45108
count #3	48370	228	345	375	12440684	58551	12440684	58551
count #4	32563	188	377	407	12601663	72708	12601663	72708
count #5	21323	153	409	439	12416151	88811	12416151	88811
						sum	62091426	141013
						average	12418285	28203
Indium activation with Cd foil 0.2188 g 1293.6 kev line								
	# of counts	error	t_1 (min)	t_2 (min)	CR	δCR	mass norm	error norm
count #1	11656	113	25	55	50404	488	64502	625
count #2	7688	92	59	89	51316	615	65670	787
count #3	5192	77	90	120	51483	759	65883	971
count #4	3374	63	122	152	50340	939	64420	1201
						sum	260476	1842
						average	65119	461
OBTAINED RESULTS								
σ_0 (b)	$\delta\sigma_0$ (b)	I_{tot} (b)	δI_{tot} (b)		φ_r/φ_{th}	$\delta(\varphi_r/\varphi_{th})$		
162.3	0.7	2650	100		0.000323	1.2E-05		

Table 3.8: *Summary of the indium foils (1293.6 keV line) activation results and calculations*

Averaging indium results (line 1293.6 keV), we obtain: $\varphi_r/\varphi_{th} = \mathbf{(3.23 \pm 0.12) \times 10^{-4}}$.

For the clarity, the next table will give the summary of the results obtained:

	$(\varphi_r/\varphi_{th}) \times 10^{-4}$	$(\varphi_r/\varphi_{th}$ **error**$) \times 10^{-4}$
Gold	4.32	0.11
Manganese	13.08	0.40
Indium (1097.3 keV)	3.15	0.12
Indium (1293.6 keV)	3.23	0.12

Table 3.9: *The summary of the foil irradiation results; the relationship between thermal and epithermal neutron fluence rates calculated by various foils*

Obviously, from the above there is a discrepancy in results obtained for different foils. This is due to the use of total resonance integral in our calculations. In particular, the total resonance integral value is calculated using the assumption that nuclear reactor resonance spectrum region is proportional to 1/E. This is illustrated in equation 1.7. The resonance integral is given by:

$$I_{tot} = \int_{E_1}^{E_2} \frac{\sigma(E)}{E} dE \qquad \textbf{eq 3.13}$$

In the case of this project, this is not entirely true, because the resonance part of neutron spectrum is not proportional to 1/E, since the neutron pass through the filters described in chapter 2. By passing through the filters, the 1/E energy distribution is violated and it could not be taken as the true energy distribution. Therefore, we used already established total resonance integrals, which are calculated under the false assumption (the assumptions that are not applicable for our case). This is the reason why the ratios between resonance fluence rates and thermal fluence rates are different for different kinds of foils. Therefore, the above values are averaged and mean value will be used in further calculations. Fortunately, for our case, the resonance fluence rate does not play a significant role in further calculations, since, on average, it is a small portion of the total fluence rate.

3.5 Absolute Efficiency Calibration of the Detector Used for Foil Counting

As mentioned in chapter 2, for calculation of the absolute thermal neutron fluence rates, it was necessary to calibrate HPGe detector (used for foil counting) for absolute efficiency. The standard, described in chapter 2 was used for this calibration. The next table summarizes this information and also gives corrected absolute activities of the

different nuclides in the standard solution, corrected for the time, that passed from May 1, 1983 (when the sample was established) to October 29, 2003, (when the calibration actually took place). This was exactly 7487 days:

Isotope	Photon Energy (keV)	Emission Rate ($s^{-1}g^{-1}$)	Emission Rate (s^{-1})	Error %	Error (s^{-1})	Time Corrected Emission Rate (s^{-1})	Error (s^{-1})
^{155}Eu	86.6	1951	10215.436	0.8	81.72	515.613	4.125
^{155}Eu	105.3	1379	7220.444	1.1	79.42	364.444	4.009
^{154}Eu	123.1	4768	24965.248	0.7	174.76	4772.522	33.408
^{125}Sb	176.4	513.6	2689.2096	0.6	16.14	15.521	0.093
^{154}Eu	248	808.1	4231.2116	0.6	25.39	808.866	4.853
^{125}Sb	427.9	2232	11686.752	0.7	81.81	67.449	0.472
^{125}Sb	463.4	784.8	4109.2128	0.7	28.76	23.716	0.166
^{154}Eu	591.7	578.4	3028.5024	0.6	18.17	578.949	3.474
^{125}Sb	600.6	1326	6942.936	0.6	41.66	40.071	0.240
^{125}Sb	635.9	847.3	4436.4628	0.6	26.62	25.605	0.154
^{154}Eu	723.3	2347	12288.892	0.6	73.73	2349.226	14.095
^{154}Eu	873.2	1425	7461.3	0.7	52.23	1426.351	9.984
^{154}Eu	996.4	1220	6387.92	1	63.88	1221.157	12.212
^{154}Eu	1004.8	2115	11074.14	0.7	77.52	2117.006	14.819
^{154}Eu	1274.4	4076	21341.936	0.6	128.05	4079.866	24.479
^{154}Eu	1596.5	207.2	1084.8992	0.7	7.59	207.397	1.452

Table 3.10: *Emission rates of the standard, SRM 4276B-198, calculated for October 29, 2003, used for efficiency calibration of the detector*

In the above table, emission rate ($s^{-1}g^{-1}$) column represents the emission rate of the every nuclide per gram, when the standard was established, May 1983. The next column represents the normalized emission, multiplied by the mass of standard source, 5.236 g. Finally, the time corrected emission rate column represents the absolute emission rate of every nuclide's energy contained in the standard sample solution, corrected for 7487 days.

The absolute efficiency of the detector is calculated simply by dividing activity of the certain peak obtained on October 29, 2003, by the time corrected emission rate for the same energy, from the table above. In these calculations, the simple activity, obtained by

the MCA equipment, for each peak of interest was used, because observed isotopes; ^{154}Eu, ^{155}Eu and ^{125}Sb have very long half-lives. Furthermore, counting period of 15 hours is negligible, compared to these half lives that are measured in years. Therefore, exponential decay curves that represent the activities of these nuclides can be approximated as linear and constant in 15 h counting time. This implies that activities are constant and integration can be obtained simply by multiplying these constant activities with counting time (15 hours in this case). Since MCA equipment gives us net number of count, these constant activities are obtained simply by dividing net number of counts with counting period of 15 h. This was not case with foil counting. In that case, obviously, we had to integrate activity curve in order to get net number of counts, because of short half-lives of the irradiated foils. See the calculations for activated foils. The uncertainty calculations for absolute efficiencies are given in appendix B. The table below summarizes these results and gives us the absolute efficiency of the detector for different gamma energies.

Radionuclide	Energy (keV)	Activity (c/s)	act error (c/s)	ε_{abs}	ε_{abs} error	error %
^{155}Eu	86.6	62.71	0.054	0.12162	0.0009785	0.80
^{155}Eu	105.3	39.93	0.041	0.10956	0.0012103	1.10
^{154}Eu	123.1	440.5	0.096	0.09230	0.0006464	0.70
^{125}Sb	176.4	1.255	0.019	0.08086	0.0012869	1.59
^{154}Eu	248	39.29	0.033	0.04857	0.0002943	0.61
^{125}Sb	427.9	2.398	0.016	0.03555	0.0003438	0.97
^{125}Sb	463.4	0.8482	0.015	0.03576	0.0006802	1.90
^{154}Eu	591.7	12.7	0.022	0.02194	0.0001368	0.62
^{125}Sb	600.6	1.082	0.015	0.02700	0.0004079	1.51
^{125}Sb	635.9	0.8856	0.016	0.03459	0.0006584	1.90
^{154}Eu	723.3	47.1	0.033	0.02005	0.0001211	0.60
^{154}Eu	873.2	23.18	0.024	0.01625	0.0001150	0.71
^{154}Eu	996.4	21.44	0.024	0.01756	0.0001766	1.01
^{154}Eu	1004.8	33.91	0.028	0.01602	0.0001129	0.70
^{154}Eu	1274.4	53.59	0.032	0.01314	0.0000792	0.60
^{154}Eu	1596.5	3.09	0.008	0.01490	0.0001112	0.75

Table 3.11: *Activity of the standard, SRM 4276B-198, obtained by MCA equipment on October 29, 2003 and calculated absolute efficiency of the germanium detector, for different gamma energies*

The graph below represents the absolute efficiency of the germanium detector, used in foils counting, based on the table 3.11

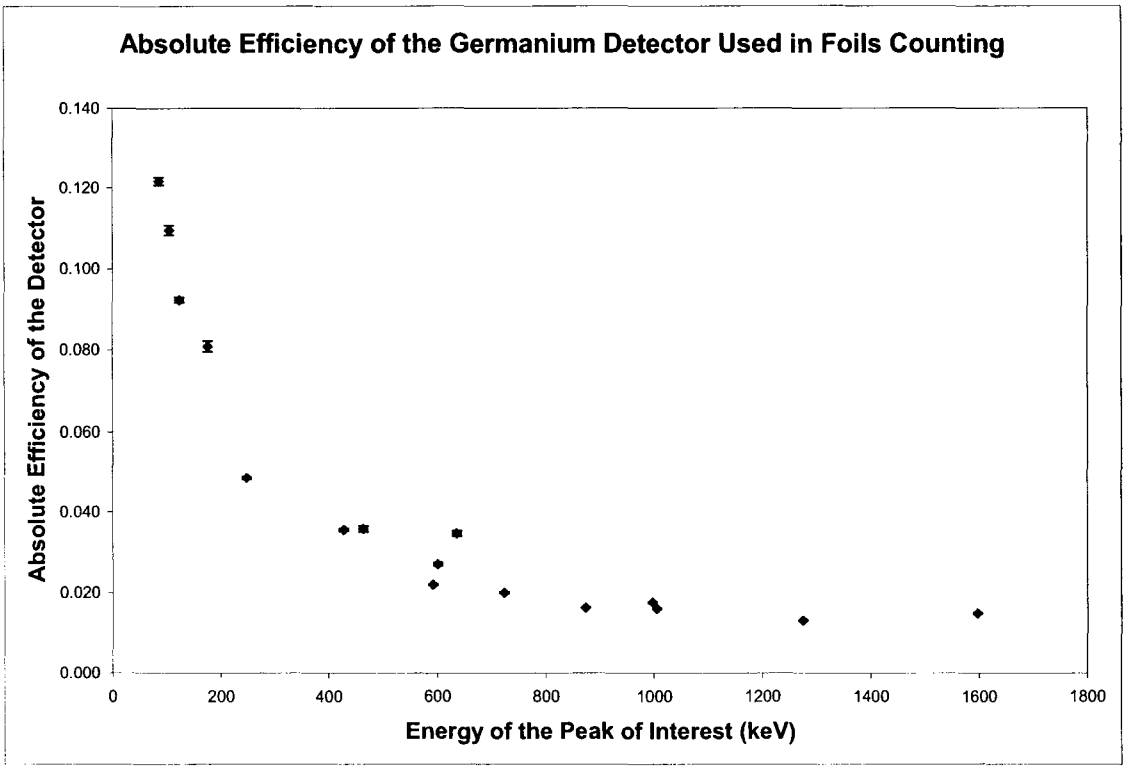

Figure 3.3: *Absolute efficiency of the HPGe detector used in foil counting vs the gamma energy*

In this graph, there are three points that do not fall into the smooth line. These are energies of 436.4, 600.6 and 635.9 keV. They all belong to ^{125}Sb isotope. This outcome is very logical, because, this isotope almost decayed completely. If we look at the table 3.11, we can see that activities under these lines are 0.8482, 1.082 and 0.8856 cps. Therefore, we can exclude these points and get more accurate graph of absolute efficiency of the detector.

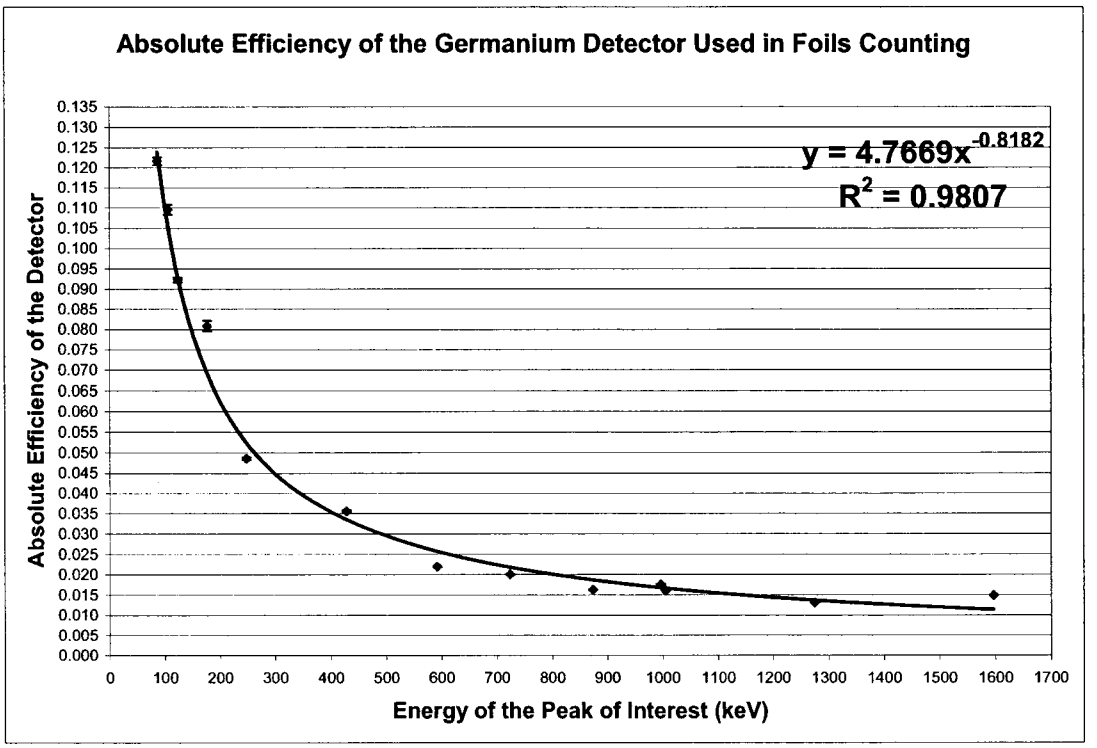

Figure 3.4: *Absolute efficiency of the germanium detector used in foils counting vs the energy with three ^{125}Sb energies excluded*

Obviously, excel gave us the best possible power fit to the relationship between absolute efficiency of the HPGe detector used for foil counting and gamma energy of interest in keV, with R^2 value of 0.9807:

$$\varepsilon_{abs} = 4.7669E^{-0.8182} \qquad \textbf{eq 3.14}$$

This equation will be used in further calculations.

3.6 Calculation of Absolute Value of Thermal Neutron Fluence Rate Using Previous Foil Irradiation Method

For calculating absolute thermal neutron fluence rate on the site, we start with well known production-decay equation for neutron bombardment. The derivations, along

with all explanations of this equation and equation that will be used here are given in appendix A. Therefore, the equation A16, with some modifications will be used here:

$$\varphi_0 = \frac{A_{tot} - A_{epi}}{\varepsilon I_\gamma a N \sigma_0 F_1 \left(1 - e^{-\lambda t_{irr}}\right)} \qquad \textbf{eq 3.15}$$

In this equation, A_{tot} represents the activity of the bare foil just after the neutron irradiation, A_{epi} represents the activity of the foil covered with Cd, just after the neutron irradiation. Furthermore, *a* represents the abundance of the isotope of interest in the bombarded sample (foil); I_γ represents the fraction of gamma rays produced at the energy of interest for each disintegration; ε is the absolute efficiency of the HPGe detector. It was found, that F_1 factors for gold, manganese and indium were 0.9454, 0.9759 and 0.6279 respectively. Furthermore, absolute efficiencies of the HPGe detector for different energies of interest were found using the already established equation 3.14. Substituting all the parameters into equation 3.15, we obtained results for thermal neutron fluence rate, using three foils. The next 4 tables summarize these results. It is important to clarify some entries in tables below. The foil mass difference correction is embedded into the calculations, so that activity column is fixed already. Furthermore, the constant value represents the calculated portion of the equation 3.15 that does not have an error associated with itself and that is:

$$const. = \frac{1}{\varepsilon I_\gamma a N F_1 \left(1 - e^{-\lambda t_{irr}}\right)} \qquad \textbf{eq 3.16}$$

For average and error average calculations, see appendix B4.

i) Gold Foil Results:

Au Activation without Cd capsule (mass: 0.195 g)						error	
	# of counts	error	t_1 (min)	t_2 (min)	A (cps)	A (cps)	
count # 1	368926	611.48	17	47	235.73	0.39	
count # 2	367640	610.74	53	83	236.43	0.39	
				sum	472.16	0.55	
				average	236.08	0.28	
Au Activation without Cd capsule (mass: 0.223 g)						error	
	# of counts	error	t_1 (min)	t_2 (min)	A (cps)	A (cps)	
count # 1	2883	69.72	88	118	1.63	0.039	
count # 2	2729	69.35	124	154	1.55	0.039	
				sum	3.19	0.056	
				average	1.59	0.028	
const.	**σ_0 (b)**	**error**		**φ_0 n/cm^{2}s**	**error**	**$\varphi_0 \times 10^7$n/cm^{2}s**	**error**
10003450	98.65	0.09		23777683	418178.25	2.38	0.042

Table 3.12: *Thermal neutron fluence rate calculated using gold foil activation*

Therefore, the average thermal neutron fluence rate using gold foil activation was found to be: $\varphi_0 = (2.38 \pm 0.042) \times 10^7$ **n/cm^{2}s**

ii) Manganese Foil Results:

Mn Activation without Cd capsule (mass: 0.0461 g)						error	
	# of counts	error	t_1 (min)	t_2 (min)	A (cps)	A (cps)	
count # 1	112843	341.67	705	735	1576.99	4.77	
count # 2	96243	315.40	741	771	1580.42	5.18	
count # 3	145545	388.70	788	848	1574.08	4.20	
count # 4	57832	246.03	853	883	1568.54	6.67	
				sum	6300.03	10.57	
				average	1575.01	2.64	
Mn Activation with Cd capsule (mass: 0.0459 g)						error	
	# of counts	error	t_1 (min)	t_2 (min)	A (cps)	A (cps)	
count # 1	5386	83.85	54	114	2.18	0.03	
count # 2	1941	51.62	138	168	2.15	0.06	
				sum	4.33	0.07	
				average	2.17	0.03	
const.	**σ_0 (b)**	**error**		**φ_0 n/cm^{2}s**	**error**	**$\varphi_0 \times 10^7$n/cm^{2}s**	**error**
242103.1	13.3	0.2		28630841	617062.74	2.86	0.06

Table 3.13: *Thermal neutron fluence rate calculated using manganese foil activation*

Therefore, the average thermal neutron fluence rate using manganese foil activation was found to be: $\varphi_0 = (2.86 \pm 0.06) \times 10^7$ **n/cm^{2}s**

iii) Indium Foil Results (1097.3 keV line):

In Activation w/o Cd capsule (mass: 0.28 g),1097.3						error	
	# of counts	error	t_1 (min)	t_2 (min)	A (cps)	A (cps)	
count # 1	104385	346.03	268	298	2137.50	7.09	
count # 2	64698	274.00	306	336	2152.11	9.11	
count # 3	39628	222.14	345	375	2168.83	12.16	
count # 4	26332	179.57	377	407	2168.41	14.79	
count # 5	17426	147.33	409	439	2159.19	18.26	
				sum	10786.04	28.86	
				average	2157.21	5.77	
In Activation withCd capsule (mass: 0.2188 g), 1097.3						error	
	# of counts	error	t_1 (min)	t_2 (min)	A (cps)	A (cps)	
count # 1	9240	109.27	25	55	10.88	0.13	
count # 2	6106	89.71	59	89	11.10	0.16	
count # 3	4109	74.46	90	120	11.10	0.20	
count # 4	2733	60.93	122	152	11.10	0.25	
				sum	44.18	0.38	
				average	11.04	0.10	
const.	σ_0 (b)	error		φ_0 n/cm^{2}s	error	$\varphi_0 \times 10^7$n/cm^{2}s	error
2102001	162.3	0.7		27795676	277928.3	2.78	0.03

Table 3.14: *Thermal neutron fluence rate calculated using indium foil activation (1097.3 keV line)*

Therefore, the average thermal neutron fluence rate using indium foil activation (line 1097.3 keV) was found to be: $\varphi_0 = (2.78 \pm 0.03) \times 10^7$ **n/cm^{2}s**

iv) Indium Foil Results (1293.6 keV line):

In Activation w/o Cd capsule (mass: 0.28 g), 1293.6						error	
	# of counts	error	t_1 (min)	t_2 (min)	A (cps)	A (cps)	
count # 1	127838	367.07	268	298	2617.75	7.52	
count # 2	78882	288.56	306	336	2623.92	9.60	
count # 3	48370	227.65	345	375	2647.27	12.46	
count # 4	32563	187.88	377	407	2681.53	15.47	
count # 5	21323	152.52	409	439	2642.05	18.90	
				sum	13212.53	30.01	
				average	2642.51	6.00	
In Activation w Cd capsule (mass: 0.2188 g), 1293.6						error	
	# of counts	error	t_1 (min)	t_2 (min)	A (cps)	A (cps)	
count # 1	11656	112.86	25	55	13.73	0.13	
count # 2	7688	92.11	59	89	13.97	0.17	
count # 3	5192	76.51	90	120	14.02	0.21	
count # 4	3374	62.91	122	152	13.71	0.26	
				sum	55.43	0.39	
				average	13.86	0.10	
const.	σ_0 (b)	error		φ_0 n/cm^{2}s	error	$\varphi_0 \times 10^7$n/cm^{2}s	error
1601414	162.3	0.7		25936883	222800.67	2.59	0.02

Table 3.15: *Thermal neutron fluence rate calculated using indium foil activation (1293.6 keV line)*

Therefore, the average thermal neutron fluence rate using indium foil activation (line 1293.6.3 keV) was found to be: $\varphi_0 = (2.59 \pm 0.02) \times 10^7$ **n/cm^{2}s**

The next table will summarize the results obtained for these three foils:

	φ_{th} ($\times 10^7$ n/cm^{2}s)	φ_{th} ($\times 10^7$ n/cm^{2}s) error
Gold	2.38	0.042
Manganese	2.86	0.06
Indium (1097.3 keV)	2.78	0.03
Indium (1293.6 keV)	2.59	0.02

Table 3.16: *Summary of thermal neutron fluence rate calculated using three different foils*

From the results obtained, we can see that there is a small discrepancy in calculated thermal neutron fluence rate at the prompt gamma experimental site, for different foils used. The possible reasons for this could be:

- *Impurities of the foils;* it is important to know that only manganese foil was the one from commercially available foil kit, with specific purity, while gold and indium foils were obtained from a different source, and the purities of these foils were assumed to be 100 %. See chapter II for details on these foils.

- *Constant fluctuation of reactor power;* MNR runs on nominal power of 2 MW, but the fluence rate constantly fluctuates due to several factors: reactor shimming, fuel changes, different core configurations, constant irradiation of different samples in the core (iodine production, rock samples, etc.) that interfere with core fluence rates, periodical trend in reactor on and off periods (see chapter I for details on this).

- *Uncertainty in the detector absolute efficiency calibration;* this is especially important for indium foil because there was approximately 7 % difference between results for two indium lines.

In order to minimize the above factors and to obtain more realistic number for thermal neutron fluence rate at the prompt gamma position, the simple solution would be to use commercially available foils with known impurities and to irradiate and count each foil at least two times per weekday (morning and afternoon). The latter would take care of daily core neutron fluence fluctuations. Of course, all these results should be averaged and they should be incorporated into the thermal neutron fluence calculations. Unfortunately, this has not been done, simply because of lack of appropriate foil materials (at least 10 identical foils of each material would be needed in order to do this), however this could be a good idea for future project, or even improvement of this project.

3.7 Prompt Gamma Neutron Activation Analysis (PGNAA) Experiments

i) Cadmium Experiments and Determination of Cadmium MDL

As mentioned previously, cadmium was used as the first element to be analyzed using prompt gamma experiments. In this case cadmium salt, $CdCl_2 \times 2.5H_2O$ was used. The mass percentage of cadmium in the salt is 49.2 %. The solution concentration ranged from 1 ppm to 50 ppm and seven different phantom sizes were irradiated (30 mL, 60 mL, 130 mL, 250 mL, 500 mL, 1 L and 2 L). There were 98 irradiations altogether. The phantoms ranging from 15 ppm to 50 ppm were irradiated for 300 s, while 9, 7 and 5 ppm phantoms were irradiated for 600 s and finally, 3 and 1 ppm phantoms were irradiated for 1800 s. All cadmium spectra were analyzed using Slide Write 4.1 program, and of course, the results obtained by the phantoms irradiated for longer time, were scaled appropriately. The spectra were analyzed between 528.112 keV and 586.551 keV. The cadmium prompt gamma peak is located in the middle of this range, at 558.46 keV. There were no other prominent peaks in this range. It was found that for different phantom sizes and dimensions, different fitting curves were used. For example, for 30 and 60 mL phantoms, Gaussian peak was used, along with slight linear decrement in the background. Therefore, the fitting equation was:

$$y = a_0 + a_1 e^{\left(-0.5\left(\frac{x-a_2}{a_3}\right)^2\right)} + a_4 a_1 x \qquad \textbf{eq 3.17}$$

Obviously, there are 5 coefficients in this fitting equation; a_0 is the background count, a_1 is the amplitude of the cadmium peak (# of counts), a_2 is the location of the cadmium peak (558 keV), a_3 is the Gaussian width and a_4 is small slope; component of the linear decrement of the equation. It is also obvious that above equation represents the

number of counts vs energy (keV) for the mentioned range. Furthermore, for the rest of the phantoms (130 mL – 2 L) error function had to be added to the equation 3.17, in order to accommodate for slight deviation from pure Gaussian peak. Therefore, the equation used was:

$$y = a_0 + a_1 e^{\left(-0.5\left(\frac{x-a_2}{a_3}\right)^2\right)} + a_4 a_1 erfc\left(\frac{x-a_2}{a_3}\right) + a_5 a_1 x \qquad \textbf{eq 3.18}$$

The next seven graphs will give the relationship between amplitude of the Gaussian cadmium peak vs concentration of the cadmium in water solution, for all seven kinds of phantoms. It is important to note that weighted least square fit was performed in each case, because we had different uncertainties for Gaussian amplitude (y value). The details of the calculations are given in appendix B5. Also, on the same graph, excel estimate of the straight line was given, along with R^2 values for each graph. It is obvious that in every graph, excellent straight line is observed and the slopes of the lines (weighted least square fit and excel estimate) are in excellent agreement.

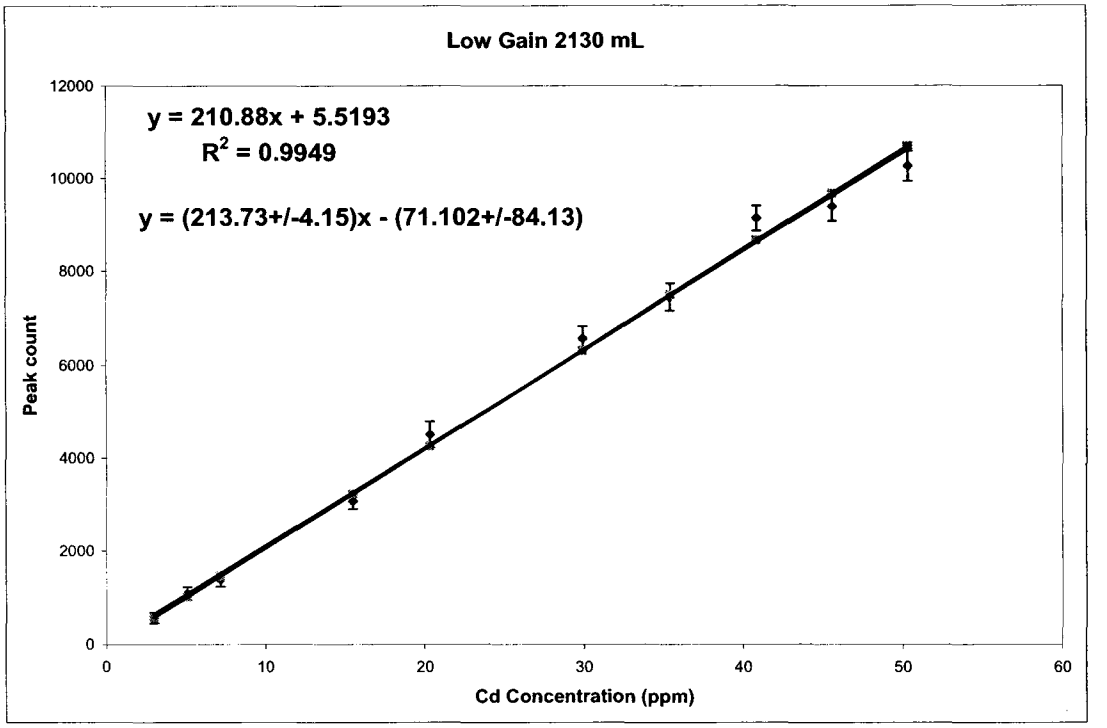

Figure 3.5: *Gaussian peak amplitude vs phantom cadmium concentration for 2130 mL phantom*

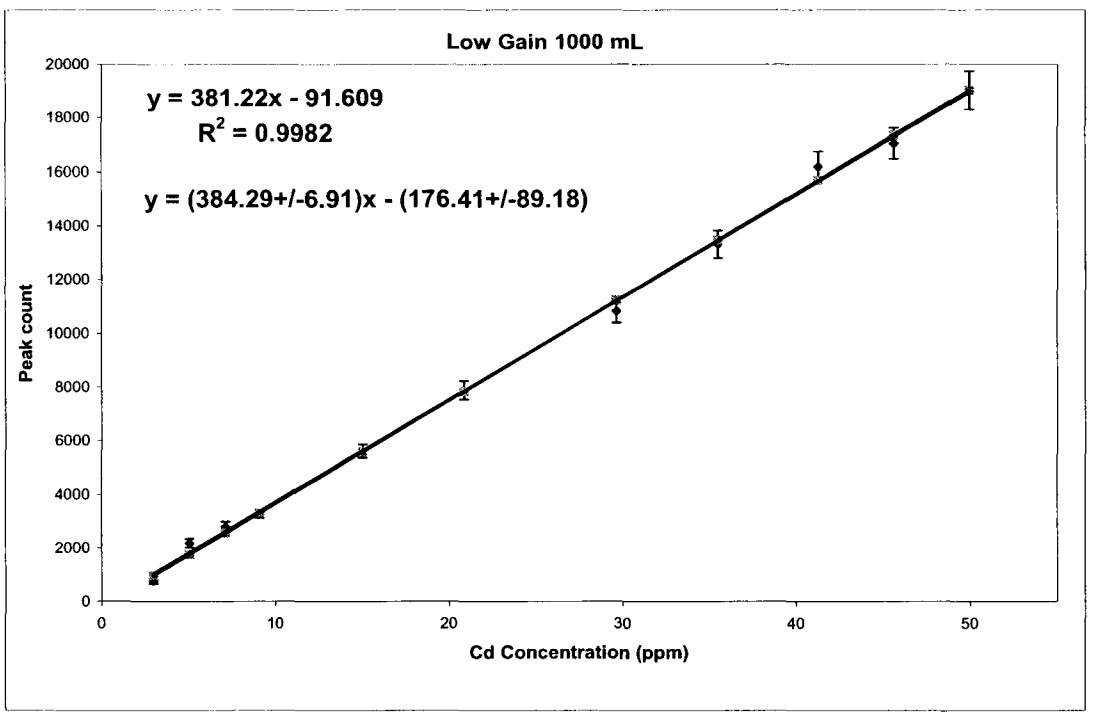

Figure 3.6: *Gaussian peak amplitude vs phantom cadmium concentration for 1000 mL phantom*

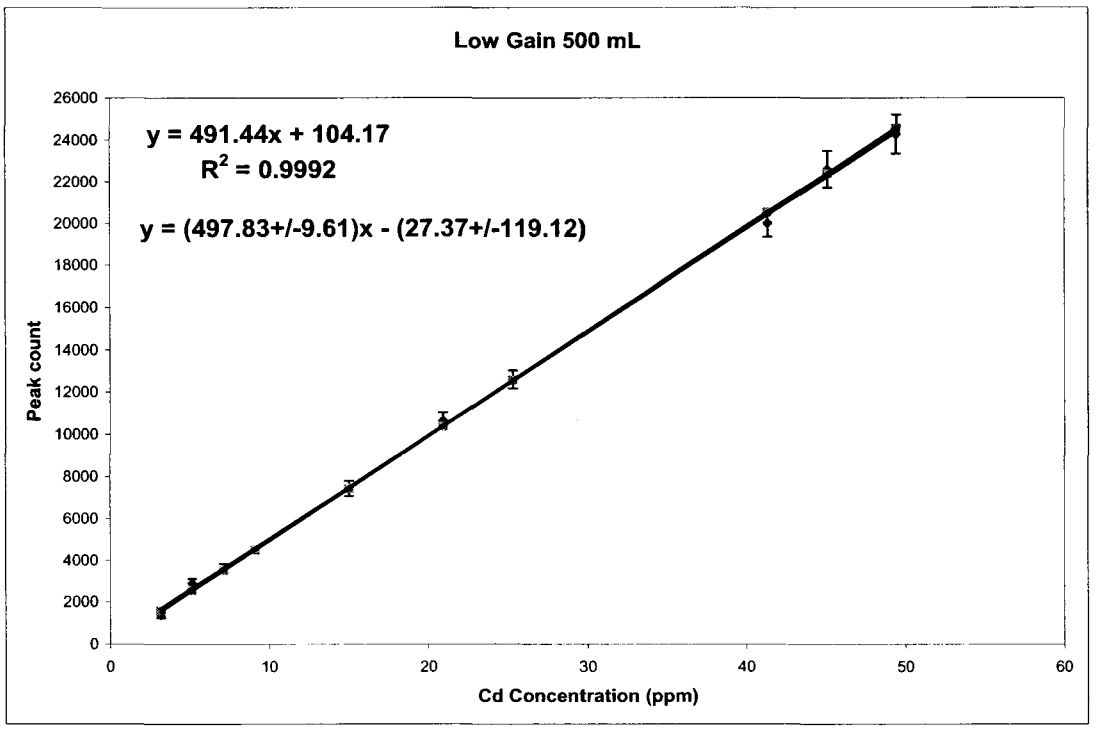

Figure 3.7: *Gaussian peak amplitude vs phantom cadmium concentration for 500 mL phantom*

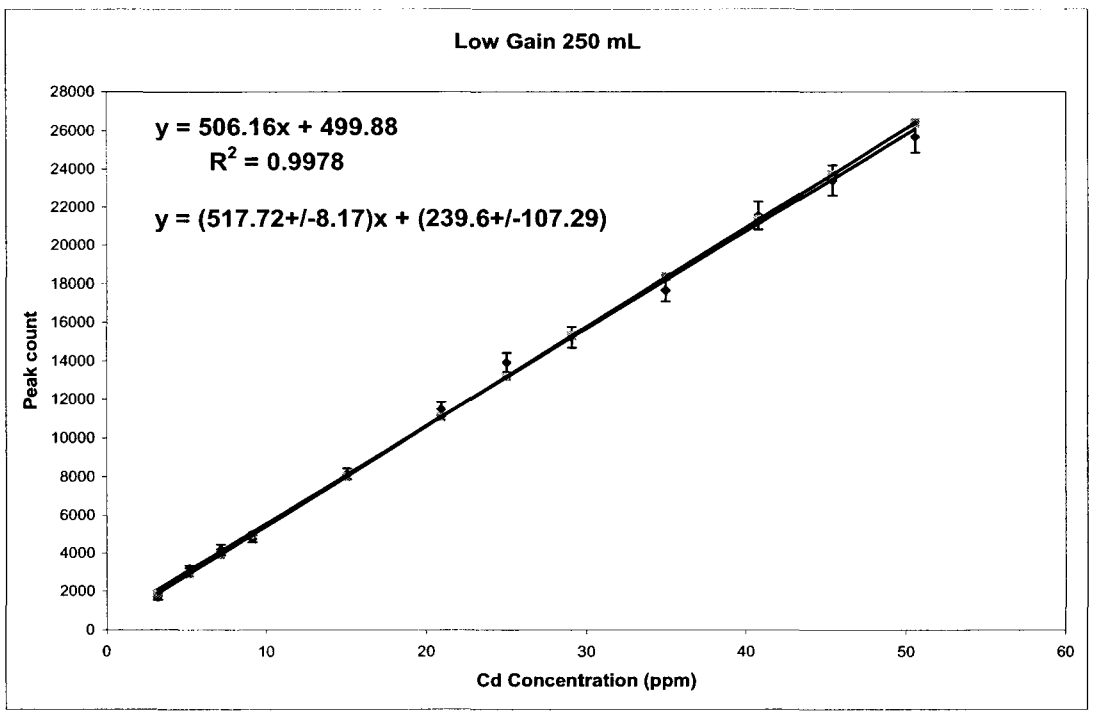

Figure 3.8: *Gaussian peak amplitude vs phantom cadmium concentration for 250 mL phantom*

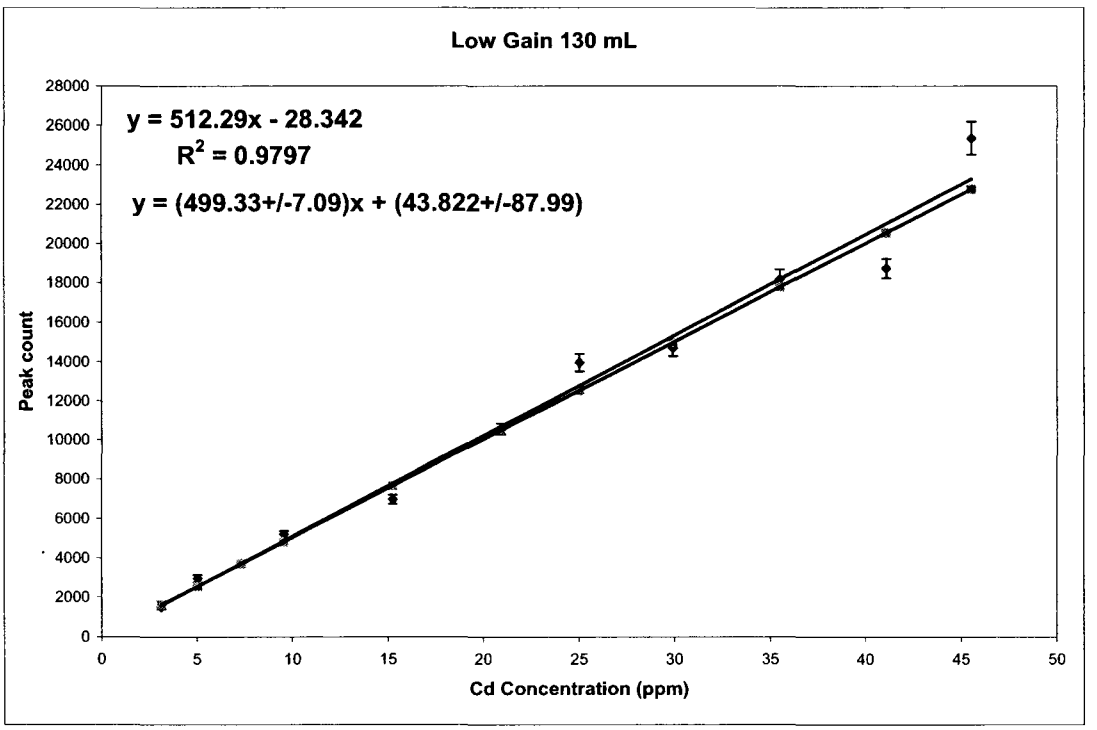

Figure 3.9: *Gaussian peak amplitude vs phantom cadmium concentration for 130 mL phantom*

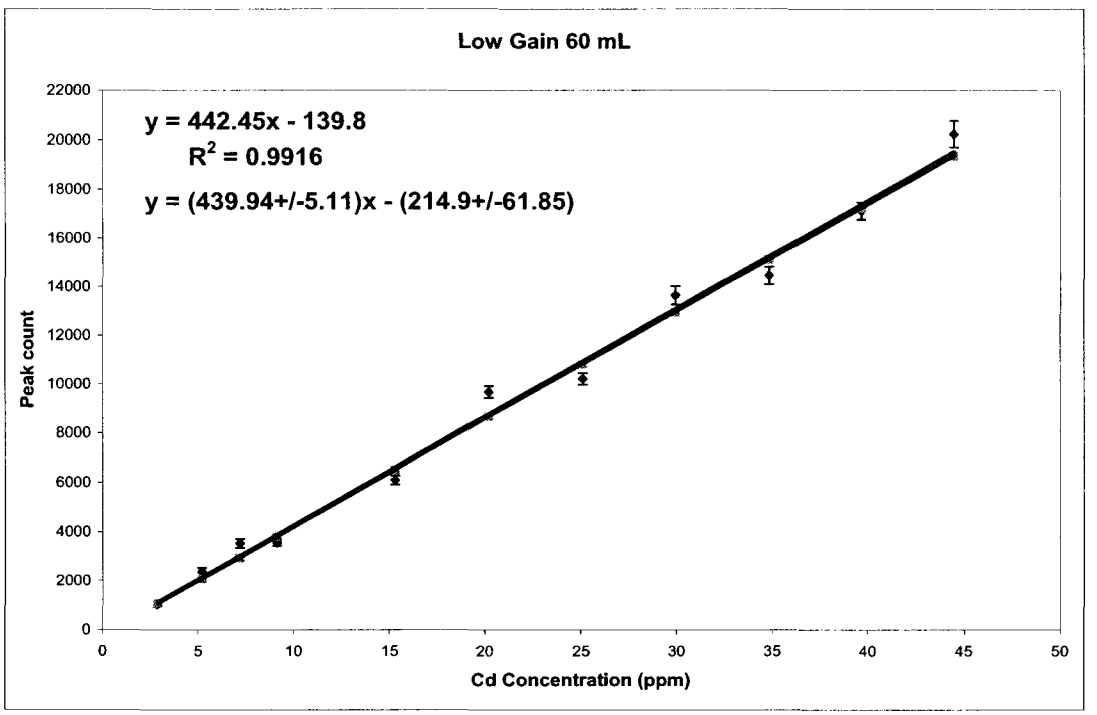

Figure 3.10: *Gaussian peak amplitude vs phantom cadmium concentration for 60 mL phantom*

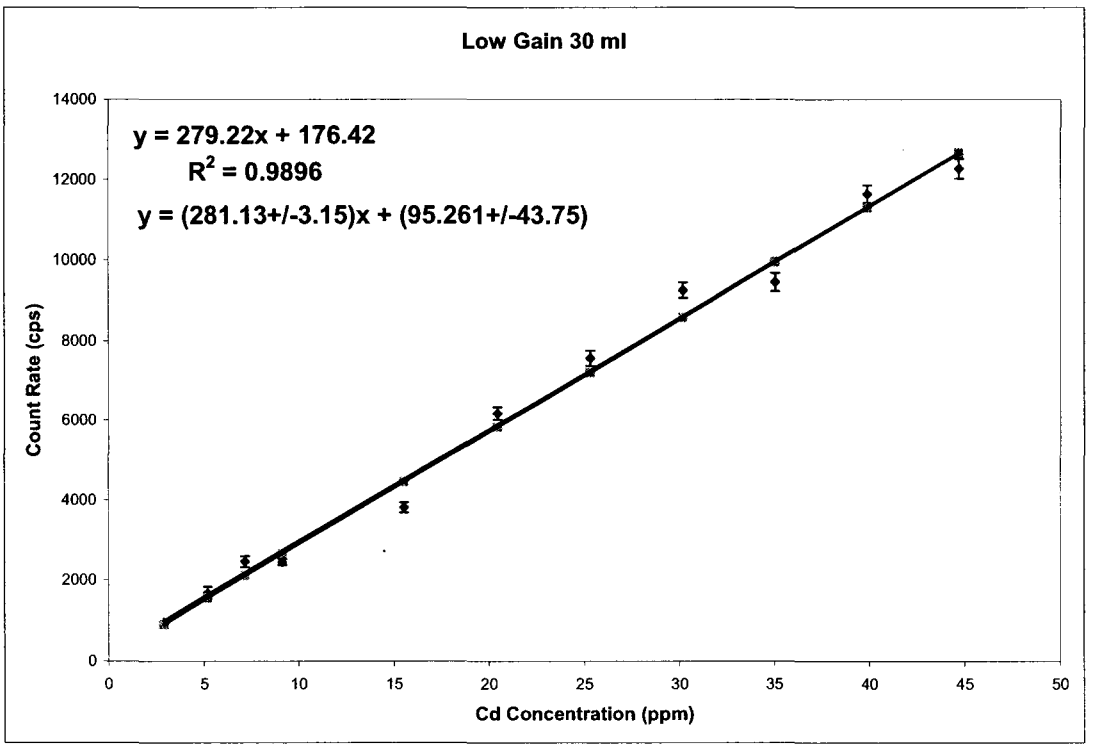

Figure 3.11: *Gaussian peak amplitude vs phantom cadmium concentration for 30 mL phantom*

Since the slopes of all the lines are determined (see the graphs), the next step is the determination of minimum detection limit (MDL) for every phantom size. MDL is given by the equation: **[Arnold]**

$$MDL = 2\sigma_{0ppm}/\text{calibration slope} \quad \textbf{eq 3.19}$$

The above equation reads that the MDL is obtained by dividing twice the uncertainty of the peak amplitude as the cadmium concentration approaches to zero (σ_{0ppm}) by the calibration slope of the line **[Pejovic-Milic]** (see the above graphs). In this project 1 ppm phantoms were used for obtaining σ_{0ppm}, because this is the lowest cadmium concentration (closest to zero) that could be measured in reasonable amount of time (30 min). The reason why 0 ppm phantoms were not used is simply because no good statistics could be obtained by fitting curves 3.17 and 3.18 through 0 ppm spectra.

Therefore, the following results might be a small overestimates of the MDL, because uncertainty of the peak amplitude for 0 ppm phantom is slightly lower than uncertainty of the peak amplitude for 1 ppm phantom. Increasing the concentration of the element, its peak amplitude is increased and therefore, the uncertainty in the peak amplitude is increased. However, according to Arnold's PhD thesis, (table 3.1, page 84) it is perfectly valid to use 1 ppm phantoms instead of 0 ppm phantoms, because the difference in uncertainties is negligible for these two concentrations (0 and 1 ppm). Therefore, the next table summarizes the results obtained for cadmium, for all seven phantom sizes.

mL	σ_{oppm} (counts)	Slope (counts/ppm)	Slope error	MDL (ppm)	MDL (mg)
30	123.33	281.13	3.15	0.8774 ± 0.0098	0.0263 ± 0.0003
60	75.25	439.94	5.11	0.3421 ± 0.0040	0.0205 ± 0.0002
130	60.43	499.33	7.09	0.2421 ± 0.0034	0.0315 ± 0.0004
250	81.43	517.72	8.17	0.3146 ± 0.0050	0.0786 ± 0.0012
500	100.94	497.83	9.61	0.4055 ± 0.0078	0.2028 ± 0.0039
1000	80.68	384.29	6.91	0.4199 ± 0.0075	0.4199 ± 0.0075
2130	86.11	213.73	4.15	0.8058 ± 0.0156	1.7163 ± 0.0333

Table 3.17: *Calculated MDL for different cadmium phantoms*

The last column in the above table represents the corresponding MDL in mg; for example: in order to observe appropriate MDL in 2130 mL phantom, it is necessary to have 1.7163 mg of Cd dissolved in 2130 mL of water, which is approximately 3.488 mg of $CdCl_2 \times 2.5H_2O$ salt. Note that the error in MDL is calculated using error propagation equation given in appendix B2. Obviously, the MDL for all seven sets of phantoms are surprisingly low, however that fact has its own cost in terms of the dose received by the possible patient (see chapter 4). This issue is further discussed in chapter 5.

As mentioned before, not only cadmium was measured and analyzed in this pilot project, the other mentioned elements were observed as well. Those were mercury and boron. Before those were measured, the simple calibration using cadmium results was

obtained in order to establish the best phantom volume for these experiments. In other words; cps/mg for each phantom was plotted vs phantom volume to see where the curve peaks and to establish the phantom with the highest value of cps/mg. For this curve, 50 ppm phantoms were used. The highest value of cps/mg had 30 mL phantom, so two more measurements with 25 and 15 mL phantoms were obtained in order to see if 30 mL is indeed the peak. It was found out that 30 mL phantom is the real peak, since we had lower values of cps/mg for 25 and 15 mL phantoms. The graph below illustrates that fact nicely.

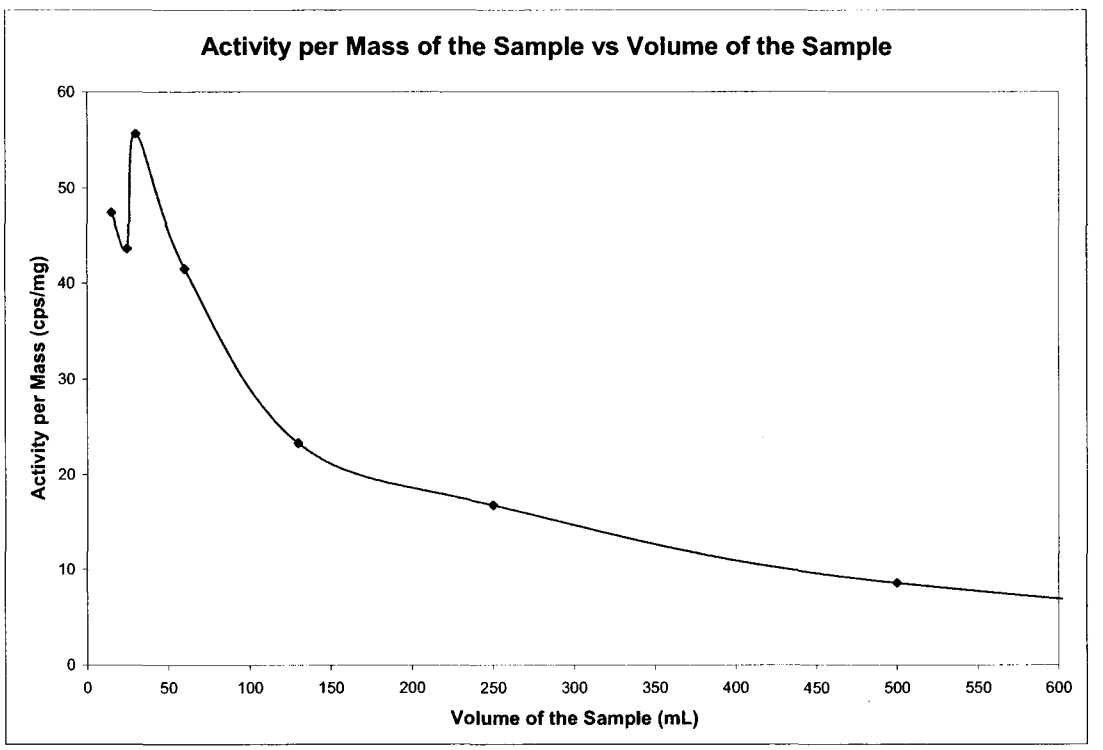

Figure 3.12: *Cadmium activity per mass vs sample volume for 50 ppm phantoms*

Therefore, based on the above discussion, mercury and boron measurements were performed in 30 mL phantoms.

ii) Mercury and Boron Experiments and Determination of their MDL's

As mentioned above, Hg and B measurements were performed with 30 mL phantoms. For mercury experiments, $HgCl_2$ (mercury II chloride) was chosen, because it is easily dissolved in water and for the same reason, for boron experiments, H_3BO_3 (solid boric acid), was chosen. The mass percentages of Hg and B in these compounds are 73.9 % and 17.5 % respectively.

Mercury concentrations ranged from about 50 ppm to 900 ppm and all the spectra were analyzed by the Slide Write program. Fifty and 100 ppm phantoms were irradiated for 600 s, 200 ppm phantom was irradiated for 480 s and the rest of phantoms were irradiated for 300 s. The procedure was similar as for the cadmium measurements, however this time, spectra were analyzed between 336 and 401 keV, because mercury prompt gamma peak is located at 367.94 keV. Similarly to the cadmium case, in this range, the only prominent peak was 367 keV mercury peak. The fitting curve was chosen to be the equation 3.18 since some deviation from pure Gaussian peak was observed in this case as well. The figure below shows the mercury phantom results, along with the weighted least square fit to the straight line, as well as excel estimate of the same.

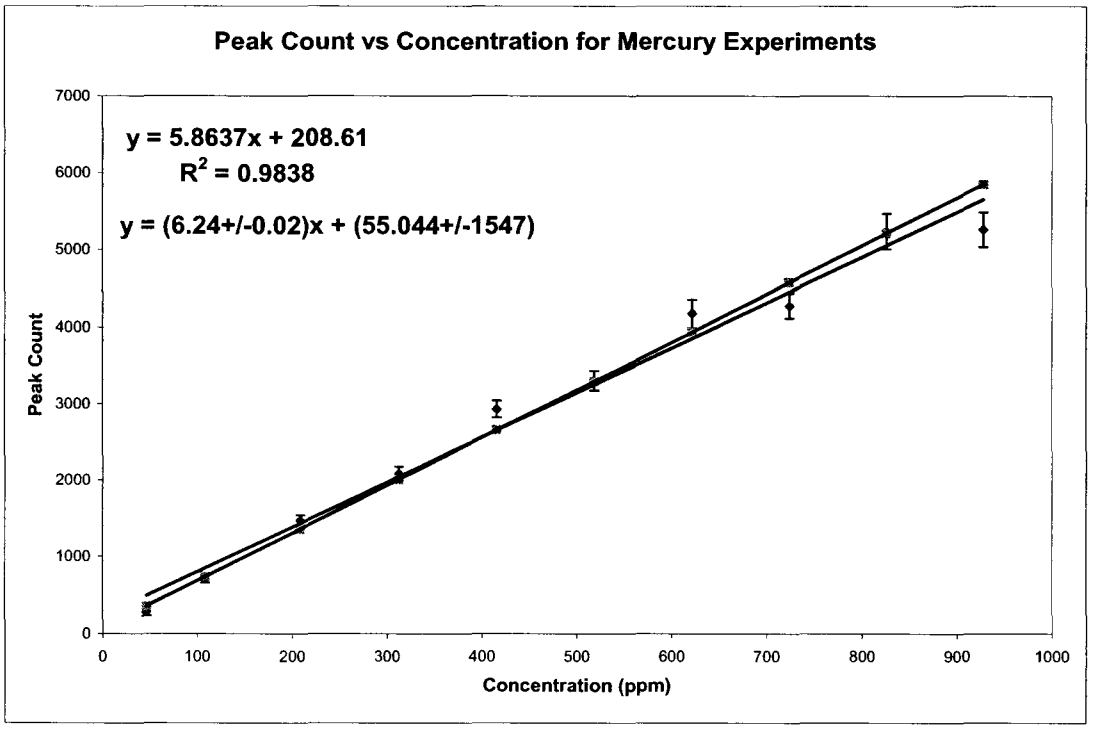

Figure 3.13: *Gaussian peak amplitude vs phantom mercury concentration for 30 mL phantom*

For calculating mercury MDL, similar approach was taken as for cadmium, except in this case the uncertainty in the 0 ppm phantom was calculated to be the square root of the background under the 367 keV peak on 0 ppm Hg spectrum. **[Pejovic-Milic]** It means that as the concentration of the element goes to zero, the intensity of the peak goes to zero as well, and uncertainty of the peak becomes the uncertainty of the background only, which is the square root of the background count, according to Poisson counting statistics. When equation 3.18 was used to fit the line on 0 ppm spectrum, the best fit obtained gave us the number of counts under 367 keV line. This number of counts corresponds to the background only, since no mercury was present in the phantom. Therefore, uncertainty is given simply by square root of this number of counts. Therefore, calculated MDL for mercury 30 mL phantoms is (16.91 ± 0.05) ppm. This

corresponds to (0.5073 ± 0.0015) mg of mercury or (0.686 ± 0.002) mg of corresponding mercury salt dissolved in 30 mL water phantom.

Same as for cadmium phantoms, the boron concentration in the phantoms ranged from 0 to 50 ppm. All the phantoms were irradiated for 300 s, except: 1 ppm (20 min), 3 and 5 ppm (15 min), 7 and 9 ppm (10 min). However, the boron analysis was done somewhat differently. The Slide Write program was not used for fitting the spectra, due to different (not Gaussian) shape of 480 keV boron peak. As mentioned before, this is not boron prompt gamma peak. This is rather the energy released from $^{10}B(n,\alpha)^{7}Li$ reaction in the form of gamma ray (480 keV). For this analysis, MCA Aptec program was used. The integration of the peaks was done completely by the Aptec software and count rate, along with the uncertainty was given by the same software. All the integrations were done between 463 and 493 keV and finally, the peak count rate vs phantom concentration was plotted.

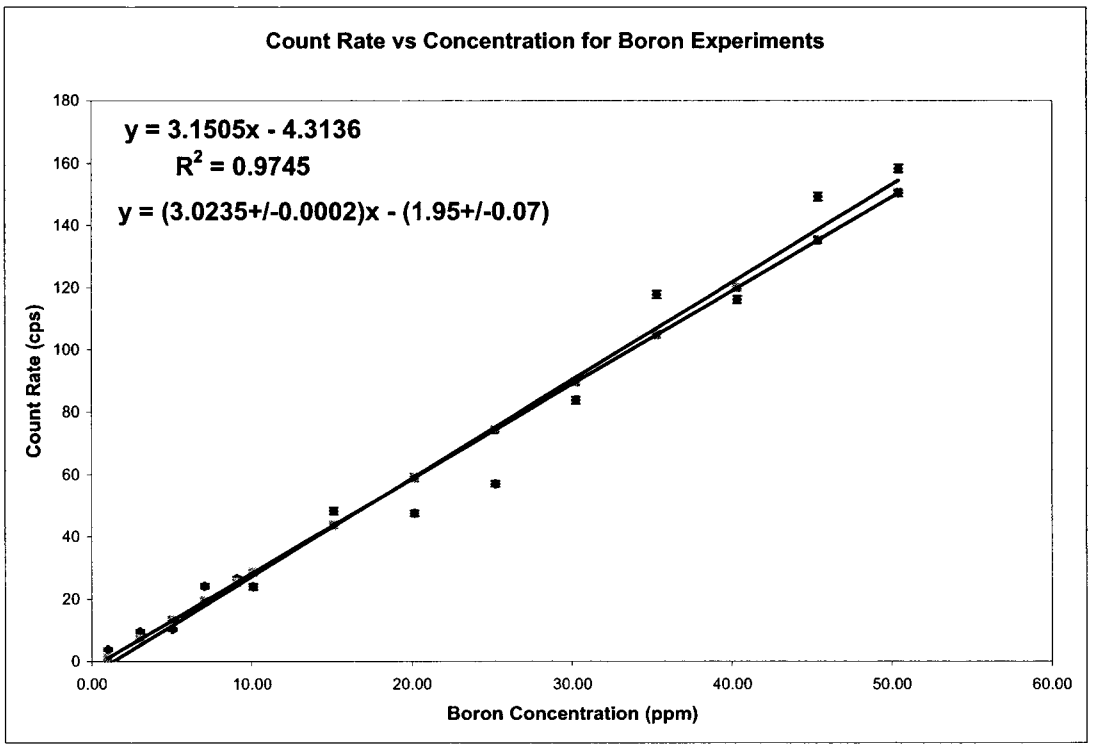

Figure 3.14: *The phantom count rate vs boron concentration for 30 mL phantoms*

Integrating 0 ppm phantom from 463 to 493 keV and taking the square root of the obtained background count in order to get the uncertainty in background count (σ_{0ppm}), MDL was found to be: (0.31321 ± 0.00002) ppm. This corresponds to (9.3963 ± 0.0006) μg of boron or (53.693 ± 0.003) μg of H_3BO_3 dissolved in 30 mL water phantom.

CHAPTER IV

Monte Carlo Experimental Modeling and Predictions

4.1 Creation and Testing of Source (sdef) card

As mentioned before, Monte Carlo calculations were performed in order to compare them with experimental results. Furthermore they were used as a tool for experimental predictions and for possible experimental site and method changes. The code used was MCNP (Monte Carlo N-Particle), version 4C2, developed in Los Alamos National Laboratories (LANL), New Mexico, US. This code was an excellent solution for this project's simulations, where neutron and photon transports were observed.

The main problem in this thesis, regarding MCNP calculations was the creation of appropriate source (sdef) card for the neutron beam in the prompt gamma cave. Since this was the very first attempt to MC model the prompt gamma cave there was no sdef card present for this experimental site. The only knowledge about the neutron beam source was that the beam was highly thermalized with rectangular cross section area of 2 inches by 1 inch. Also, it was known that the beam was collimated very well and that the scatter (when there is nothing in the beam) was negligible.

Since the cross sectional area of the beam was very small, it was assumed that spatially, the neutron fluence rate in the beam is constant, ie. $\varphi(x,y)$ at certain z position is constant. Therefore, the only concern was the energy dependant neutron fluence rate, ie. neutron spectrum.

From the very first experiments (foil irradiations), three facts were established about the neutron beam. Those are:

- ***the thermal neutron fluence rate was (2.653 ± 0.210)×10^7 n/cm^{2}s on average***
- ***the neutron beam consists of (99.94 ± 0.0011) % of thermal neutrons (kinetic energy ranging from 0 to 0.4 eV, where 0.4 eV is theoretical cadmium cut-off energy)***
- ***(0.06 ± 0.001) % of neutron in the beam were epithermal (kinetic energy, ranging from 0.4 eV to some "unknown energy"***
- ***neutron beam absolutely free of fast neutrons (no response with threshold foils)***

From the information above, it was impossible to create a complete sdef card, therefore some assumptions about the source had to be made. Furthermore, these assumptions had to be checked with MCNP in order to make sure that they would not make significant differences in code outputs. For those simulations, the source was made to be rectangular (as it is; 2.54 cm × 5.08 cm), unidirectional, collimated in the air, with very simple geometry; source enclosed in the sphere, with radius of 1 m. The tally f4 (particle fluence averaged across the cell) from the output, was observed, in different input settings, in order to optimize the neutron beam. The multiplier constant fm4 was not used, because the point of these exercises was only comparison of relative neutron fluence rates. In order to observe f4 tally outputs, it was required to make simple cubical shape cells, filled with an air, because f4 tally gives averaged neutron fluence rate across the 3D cell. Using different positions of these cells and their different sizes, two things were observed:

- ***neutron scatter out of the beam (beam collimation)***
- ***stability of neutron fluence rate along the beam in z direction, in air medium (attenuation of neutron beam in the air)***

However, the main concern about the neutron beam was the epithermal energy cut-off and the shape of thermal and epithermal parts of the spectrum. From the foils' irradiations (threshold foils), it was found out that the final energy cut off was 0.8 MeV, since no response was observed on $^{103}Rh(n,n')^{103m}Rh$ reaction, where threshold was 0.8 MeV. Therefore, the whole epithermal spectrum (0.06% of total neutron output) was set up from 0.4 eV to 0.8 MeV (maximum value). This maximum value was varied from 10 eV to 0.8 MeV in order to compare f4 tallies for different setups.

Finally, the shapes of thermal and epithermal output were observed. Several different energy descriptions (distributions) were used. The first energy setup was the simple histogram with two energy bins, where 99.94 % of neutrons were sitting in 0 - 0.4 eV range (Cd cut off) and the rest of the neutrons in 0.4 eV to 10 eV or 0.4 eV to 0.8 MeV) energy range. See the source card below:

```
40-    sdef par =1 x = d1 y = d2 z = 0 erg =d3 vec = 0 0 1 dir =1
41-    si1  h 0 2.54
42-    sp1  d 0 1
43-    si2  h 0 5.08
44-    sp2  d 0 1
45-    #    si3          sp3
46-         6.25e-9      0
47-         4e-7         0.9994
48-         1e-5         0.0006
```

Note that the last entry in energy distribution portion of sdef card (line 48) varied from 10 eV (1e-5 MeV) to 0.8 MeV, as it is said above.

The second energy setup was based on Maxwellian distribution for thermal neutrons (see equation 1.5). The equation was integrated with respect to energy in order to create a more complex energy histogram with 27 entries (again from 0 to 0.4 eV). The last

entry was the energy bin (epithermal neutrons 0.06 %) ranging from 0.4 eV – (10 eV – 0.8 MeV), same as in previous source card. See the source card below:

```
40-    sdef par =1 x = d1 y = d2 z = 0 erg = d3 vec = 0 0 1 dir =1
41-    si1  h 0 2.54
42-    sp1  d 0 1
43-    si2  h 0 5.08
44-    sp2  d 0 1
45-    #    si3              sp3
46-         6.25e-9          0
47-         0.000000008      0.015062417
48-         0.00000001       0.020191285
49-         0.000000012      0.022808583
50-         0.000000014      0.024911363
51-         0.000000016      0.026562721
52-         0.000000018      0.027819131
53-         0.00000002       0.02873109
54-         0.000000022      0.029343703
55-         0.000000024      0.029697205
56-         0.000000026      0.029827447
57-         0.000000028      0.029766325
58-         0.00000003       0.029542177
59-         0.000000032      0.029180139
60-         0.000000034      0.028702466
61-         0.000000036      0.028128828
62-         0.000000038      0.027476574
63-         0.00000004       0.026760968
64-         0.00000005       0.121702577
65-         0.00000006       0.100316501
66-         0.00000007       0.079922021
67-         0.00000008       0.062151344
68-         0.00000009       0.047465168
69-         0.0000001        0.03574367
70-         0.0000002        0.094218639
71-         0.0000003        0.003276555
72-         0.0000004        9.11025e-5
73-         0.00001          0.0006
```

At the end, the built in Maxwell shape function for thermal neutrons was used. The simple sdef energy distribution card is given below:

```
40-     sdef par =1 x = d1 y = d2 z = 0 erg = d3 vec = 0 0 1 dir = 1
41-     si1  h 0 2.54
42-     sp1  d 0 1
43-     si2  h 0 5.08
44-     sp2  d 0 1
45-     sp3 -2  2.53e-8
```

i) Stability of the neutron beam (source)

The first set of MCNP runs was done in order to check the neutron scatter and air attenuation of the beam. The energy distribution on the sdef card was decided to be integrated Maxwellian distribution, equation 1.5, pictured by histogram for 99.94 % of thermal neutrons (6 bins all together) and one bin for epithermal portion of the spectrum (0.06 % of the thermal fluence rate). This epithermal portion of the spectrum (last bin) was varied from 0.4 eV to 10 eV in one case and from 0.4 eV to 0.8 MeV in the other case (same as before). There was a negligible tally output difference for these two cases. It was less than 2 %. Therefore, the complete sdef card is given below:

```
sdef par =1 x = d1 y = d2 z = 0 erg = d3 vec = 0 0 1 dir = 1
 31-     si1  h 0 2.54
 32-     sp1  d 0 1
 33-     si2  h 0 5.08
 34-     sp2  d 0 1
 35-     #     si3          sp3
 36-           3.125e-9     0
 37-           6.25e-9      0.02588187
 38-           1.25e-8      0.06245625
 39-           5e-8         0.49875063
 40-           1e-7         0.31717782
 41-           4e-7         0.09503343
 42-           1e-5         0.0006
```

The table below (table 4.1) represents the summary of 6 MCNP runs with the above source card and different air cells, where f4 tallies were sampled. All the runs were with 10^6 histories (nps = 10^6), except run # 5, which was 10^7 histories, because the

neutron scatter in the air was involved and better statistics was required. In the first four MCNP runs, there were 7 f4 tallies sampled in 7 cells right above the source in the air medium. All those cells were rectangular in shape, with the dimensions given in the table. They were all located in the direct neutron beam. The MCNP run # 5 was the same as run # 2, except that 4 f4 tallies were added (outside the beam) in order to sample for possible neutron scatter out of the beam. Finally, the run # 6 was the same as run # 5, except that the run was performed in the vacuum. The simplified figure below shows the arrangement of the source and tally cells:

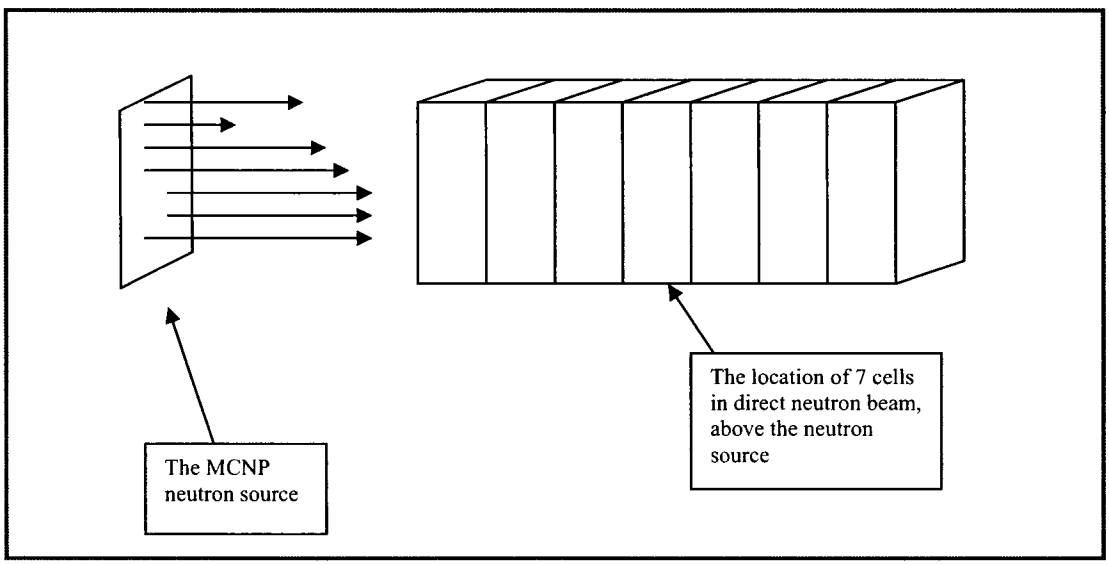

Figure 4.1: *The simplified arrangement of the MCNP neutron source and seven cells located directly above the source.*

Note that above diagram shows only the cells located directly in the neutron beam, however, there are 5 more rectangular cells that are not located in the beam. They are located outside the beam and they are used as neutron scatter tallies.

Description of MCNP run	f4	f14	f24	f34	f44	f54	f64	f74	f84	f94	f104	f114
7 cells right above the source, cells' volume: $(2.54\times5.08\times1)cm^3$	7.7513 ± 0.0000	7.7472 ± 0.0000	7.7436 ± 0.0000	7.7395 ± 0.0000	7.7360 ± 0.0000	7.7318 ± 0.0000	7.7282 ± 0.0000					
7 cells right above the source, cells' volume: $(2.54\times5.08\times2)cm^3$	7.7493 ± 0.0000	7.7414 ± 0.0000	7.7342 ± 0.0000	7.7265 ± 0.0000	7.7182 ± 0.0000	7.7102 ± 0.0000	7.7020 ± 0.0000					
7 cells right above the source, cells' volume: $(5.08\times10.16\times2)cm^3$	1.9389 ± 0.0000	1.9370 ± 0.0000	1.9353 ± 0.0000	1.9336 ± 0.0000	1.9316 ± 0.0000	1.9295 ± 0.0000	1.9275 ± 0.0000					
7 cells right above the source, cells' volume: $(1.27\times2.54\times2)cm^3$	7.7285 ± 0.0017	7.7207 ± 0.0017	7.7146 ± 0.0017	7.7075 ± 0.0017	7.6988 ± 0.0017	7.6908 ± 0.0017	7.6829 ± 0.0017					
7 cells right above source; $(2.54\times5.08\times2)cm^3$; 5 scatter cells	7.7494 ± 0.0000	7.7421 ± 0.0000	7.7345 ± 0.0000	7.7267 ± 0.0000	7.7189 ± 0.0000	7.7110 ± 0.0000	7.7031 ± 0.0000	3.4651 ± 0.0165	3.4299 ± 0.0166	3.0310 ± 0.0232	3.0577 ± 0.0232	2.5862 ± 0..0180
7 cells right above source; $(2.54\times5.08\times2)cm^3$; 5 scatter cells; all void cells	7.7500 ± 0.0000	7.7500 ± 0.0000	7.7500 ± 0.0000	7.7500 ± 0.0000	7.7500 ± 0.0000	7.7500 ± 0.0000	7.7500 ± 0.0000	0.0000 ± 0.0000	0.0000 ± 0.0000	0.0000 ± 0.0000	0.0000 ± 0.0000	0.0000 ± 0.0000

Table 4.1: *Summary of the 6 MCNP runs (tally f4); Source scatter and attenuation check*

Note that these MNCP runs did not have fm4 (multiplier constant) entered, because the purpose of these runs was only to observe the relative neutron fluence rates. Also, it is important to mention that in the table 4.1, the tallies f4-f64 are supposed to be multiplied by 10^{-2} and tallies f74-f114 are supposed to be multiplied by 10^{-5}. Therefore, in the run # 5, tally f64 will read $(7.7031\pm0) \times 10^{-2}$ and tally f74 will read $(3.4651\pm0) \times 10^{-5}$.

From the first four runs it is obvious that the beam is very constant, with negligible attenuation in the air. From the run # 1, neutron fluence attenuation is 0.298 %, in 6 cm ((7.7513 – 7.282)/7.7513). Furthermore, from the run # 2, the attenuation is 0.61 %, in 12 cm. The run # 5 shows that the neutron scatter out of the beam is negligible, because tallies f74-f114 are approximately 0.04 % of tallies f4-f54. The last run tells us that there is absolutely no scatter, nor attenuation in the vacuum. From the above facts, it is obvious that the neutron beam is constant throughout, the neutron scatter is negligible and it implies that the beam is very well collimated.

ii) The Choice of the Neutron Energy Distribution in sdef card

As mentioned above, several possible energy distribution cards were checked and the outputs were observed. Again, f4 tallies were observed, but this time, only 6 f4 tallies located directly in the neutron beam, since neutron scatter was previously checked. The next table summarizes the f4 tallies for different MCNP runs. Note that all the runs had 10^6 histories (nps = 10^6).

Description of MCNP run	f4	f14	f24	f34	f44	f54	f64
-6 bins based on Maxwell distribution -E_{max}=10eV	7.9693 ± 0	7.9613 ± 0	7.9539 ± 0	7.9460 ± 0	7.9375 ± 0	7.9292 ± 0	7.9209 ± 0
-6 bins based on Maxwell distribution -E_{max}=0.8MeV	8.0581 ± 0.0005	8.0501 ± 0.0005	8.0427 ± 0.0005	8.0348 ± 0.0005	8.0263 ± 0.0005	8.0181 ± 0.0005	8.0098 ± 0.0005
-6 bins based on Maxwell distribution -E_{max}=12MeV	8.1535 ± 0.0009	8.1455 ± 0.0009	8.1381 ± 0.0009	8.1302 ± 0.0009	8.1217 ± 0.0009	8.1134 ± 0.0009	8.1051 ± 0.0009
-27 bins based on Maxwell distribution -E_{max}=10eV	7.9398 ± 0	7.9318 ± 0	7.9245 ± 0	7.9167 ± 0	7.9083 ± 0	7.9001 ± 0	7.8918 ± 0
-27 bins based on Maxwell distribution -E_{max}=0.8MeV	8.0286 ± 0.0005	8.0207 ± 0.0005	8.0133 ± 0.0005	8.0055 ± 0.0005	7.9971 ± 0.0005	7.9889 ± 0.0005	7.9808 ± 0.0005
-27 bins based on Maxwell distribution -E_{max}=12MeV	8.1240 ± 0.0009	8.1161 ± 0.0009	8.1087 ± 0.0009	8.1009 ± 0.0009	8.0925 ± 0.0009	8.0843 ± 0.0009	8.0760 ± 0.0009
-energy distribution = Maxwell built in function	7.9191 ± 0	7.9111 ± 0	7.9027 ± 0	7.8941 ± 0	7.8860 ± 0	7.8771 ± 0	7.8685 ± 0
-only 2 energy bins -one for themal and one for epithermal energies	8.3633 ± 0	8.3633 ± 0	8.3633 ± 0	8.3633 ± 0	8.3633 ± 0	8.3633 ± 0	8.3633 ± 0

Table 4.2: *Summary of the 8 MCNP runs (tally f4); Source energy spectrum check*

All the entries in the above table are supposed to be multiplied by 10^{-1}, but this factor was omitted, as it was done in previous table, because we are interested only in comparison of numbers. Also, in these MCNP runs, "Fluence to Dose Equivalent Conversion Function for Neutrons" (NCRP 38) was used. That is the reason why the entries in the above table are approximately 10 times larger than entries in the table 4.1. Again, multiplier constant, fm4, was not used.

From the table 4.2 it can be concluded that there is no significant difference whether the energy cut off for epithermal neutrons is 10 eV or 0.8 MeV, or even 12 MeV. This is obvious by comparing f4 tallies of first and second run and of fourth and fifth run. The first and second run differ 1.1 % as well as fourth and fifth. Furthermore, if we compare epithermal cut off of 0.8 MeV and 12 MeV, we get insignificant difference again; 1.2 %. From all these observations, the conclusion can be drawn that epithermal portion that consists of 0.06 % of total neutron fluence, does not play very important role and it can be approximated by a single energy bin that goes from 0.4 eV to 10 eV, or 0.4 eV to 0.8 MeV. The difference is negligible. Furthermore, there was a MCNP run (# 7) representing Maxwell built in function for thermal fluence distribution. The difference between f4 of this run and f4 of run # 5 is 1.4 %. Finally, the difference between run # 5 and run # 8 (simple two energy bins for epithermal and thermal neutrons) is 4.2 %. Therefore, the final neutron energy spectrum that will be used further in MCNP runs will be integrated Maxwellian distribution equation for thermal neutrons (eq 1.5) that consists of 27 energy bins and one energy bin for epithermal portion of the spectrum that goes from 0.4 eV to 0.8 MeV (run # 5 in table 4.2)

iii) The Normalization of Neutron Fluence Rate for Further MCNP calculations

The thermal neutron fluence rate was measured to be 2.653×10^{7} n/cm^{2}s (99.94% of total neutron output) on average. This neutron fluence rate was measured at the position where prompt gamma rabbit samples are irradiated, since the irradiations of the foils were done at that position. According to the MCNP geometry, established for this particular project, the position in Cartesian coordinates that corresponds for irradiation

point is (0, -8.89, 0) cm. However, the starting point of the rectangular source is set at the point (26.67, -8.89, 0) cm. The particles (neutrons) are unidirectional, flying toward negative X direction. Therefore, the source strength has to be extrapolated from 0 to 26.67 cm in positive x direction in order to get the appropriate source strength (2.653×10^7 n/cm^2s) at the desired position (0, -8.89, 0) cm. To solve this problem, the previous MCNP runs will be used, particularly run # 5, from table 4.2. Graphing this MCNP output, the following was obtained:

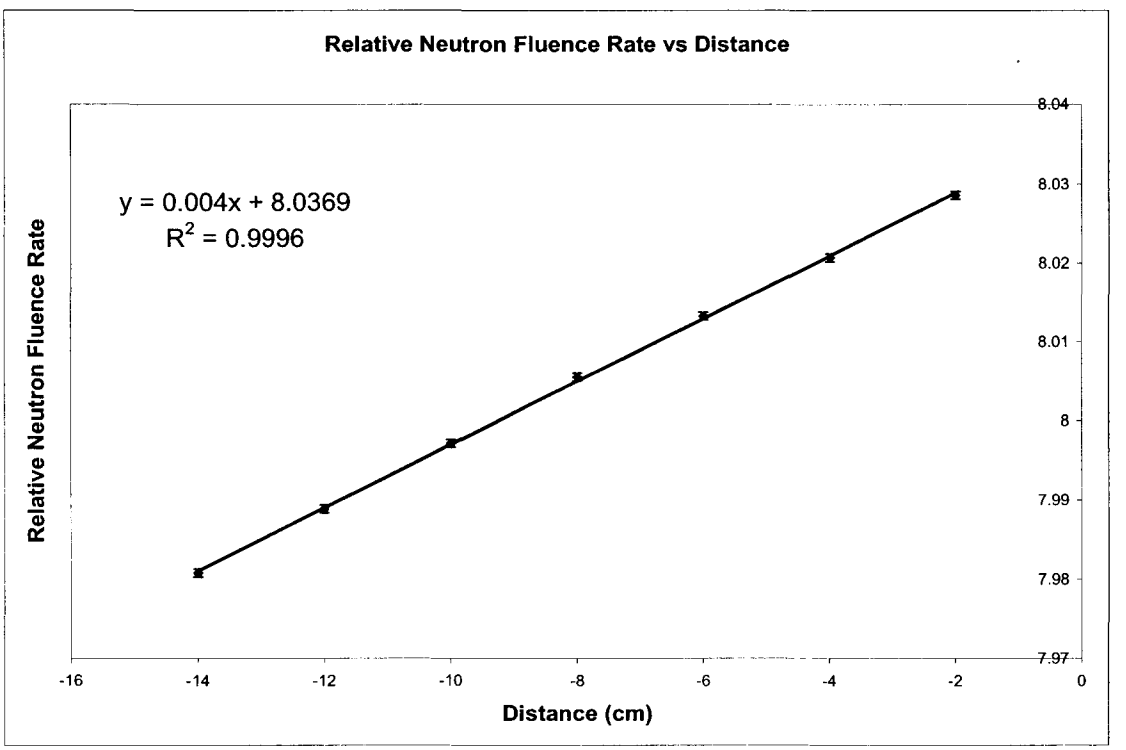

Figure 4.2: *MCNP Relative Source Strength vs Distance*

Obviously, the beam attenuation was approximated with the straight line, because neutron fluence rate is slowly varying in the air. The above figure illustrates that fact perfectly. Substituting position 0 and 26.67 cm into the equation of the straight line, we obtain relative neutron fluence rates of 8.0369 and 8.1436 respectively. Therefore the extrapolation factor for neutron fluence rate at position (26.67, -8.89, 0) would be

8.1436/8.0369 = 1.013. As it was indicated, this is important for further MCNP calculations, when multiplier constants are introduced in order to normalize gamma and neutron exposure rates at particular positions in the cave, as well as detector response function (f8 tally).

4.2 MCNP Simulations of Experiments

Since sdef card was created and tested, the next step would be the simulation of actual prompt gamma experiment, as well as exposure rate calculations due to neutrons and induced gamma rays at the experimental site. The main feature here would be the appropriate creation of the site's geometry. The concrete walls of the prompt gamma cave would be omitted, because it was shown that the beam was very well collimated, and negligible scatter was present when there was nothing in the beam. The emphasis would be given on the beam's vicinity and the detector shielding. Those things will be carefully modeled with appropriate material cards for: paraffin wax, aluminum, lead, boroflex, plywood, germanium, lithium carbonate, etc. The whole geometry, consisting of HPGe detector, its shielding, neutron beam and shielding in its vicinity will be enclosed in a large air sphere and number of different tallies will be observed and analyzed. The important geometry is shown on figure below:

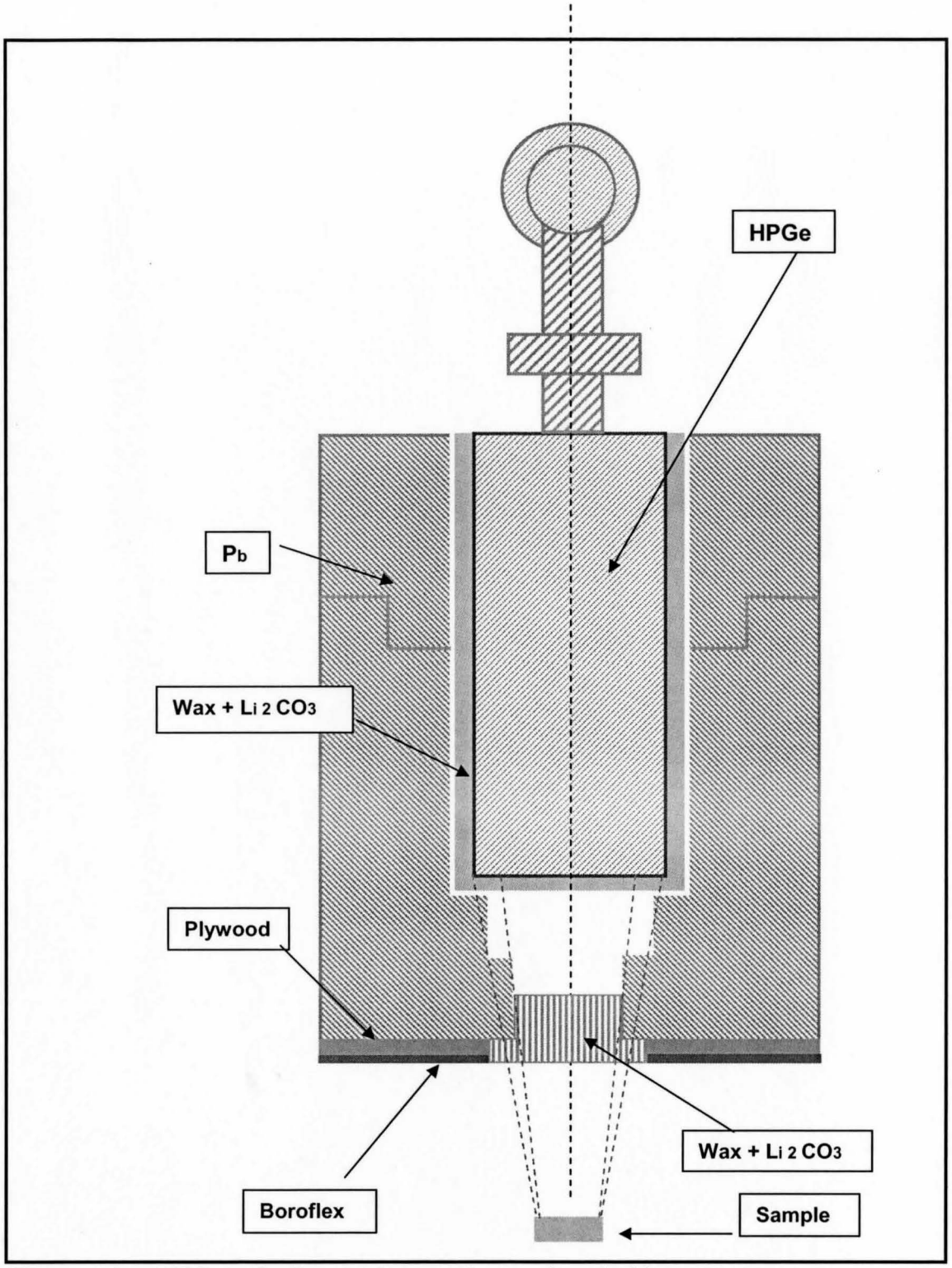

Figure 4.3: *HPGe in the Prompt Gamma Cave and its shielding*

From the above figure, HPGe is enclosed in the huge lead cylinder, with the other shielding materials present, like wax, lithium carbonate, boroflex and plywood. All this is covered with paraffin wax slabs, but that is approximated by the wax box with rectangular basis (87 × 77 × 127) cm^3. Furthermore, there is aluminum table where the samples sit and finally there is some more wax in the vicinity of the sample. The complete geometry is pictured in the figure 2.4 (chapter II).

i) MCNP Detector Pulse Analysis

Unfortunately, it is impossible to model HPGe (pulse height tally f8) and to simulate neutron and photon transport at the same time, simply because there are no germanium cross section data in the present XS library for neutron transport. In order to do that, it is necessary to purchase DLC-190 data library, along with software FSX96 in order to incorporate it into XS data library. This DLC-190 is available from RSICC collection of continuous energy cross section libraries based on recent JENDL (Japanese library) release. It contains the library for germanium, which is 32000.37c. Therefore, MCNP model of the prompt gamma experiment involving HPGe detector and collection of the f8 tally would be a good idea for future work.

However it is possible to do model HPGe detector, without DLC-190 data library only if the MCNP is running in the p mode (photon transport only). The material card for germanium in this case is simply 32000. Therefore, the only thing that is possible right now is the MCNP absolute efficiency calibration of the HPGe detector, using the standard Eu source (already used for foil counting calibration), as the probe and calibration check. The only problem with this experiment is the precise geometrical data

for germanium detector given by the manufacturer (ORTEC in our case). The simulated MCNP data probably would not agree with the experimental data for the first run. **[Karamanis at al.]**. There are two main reasons for that; the dead zone thickness can be different from the one provided by the manufacturer (grow up every year about 1 mm, due to constant heating and cooling of the detector) and the distance between the Ge crystal and Al enclosure can change due to repairing **[Karamanis at al.]**. Therefore, these parameters are adjustable and they would be constantly adjusted until the excellent agreement is achieved between experimental and simulated results. Once the HPGe detector correct inside geometry is established, the absolute efficiency calibration for different samples can be done. This implies the absolute efficiency calibration for different phantom sizes and geometries. Basically, known concentration and activity of the known gamma emitters (this represents a source in MCNP code) would be loaded into the water filled phantoms with different dimensions and it would be MCNP modeled in order to get detector response (f8 tally). This would be pure MCNP detector absolute efficiency calibration, without experimental trials and of course MCNP calculations for the self shielding of the source will be performed in order to adjust the absolute efficiency. However, this project is very broad itself and would require lots of time and effort. Moreover it would diverge from the main course of this thesis. Therefore, this could be left for some future research, as well.

However, MCNP will be used here in order to check the photon energy spectrum that crosses the detector window, as well as photon energy spectrum created while irradiating 30 mL phantom, filled with water only. The main emphasis will be on the most prominent lines; 511 keV annihilation peak and 2.2 MeV hydrogen prompt gamma

peak. The reason why the smallest phantom was used is simply because it's shape and dimensions are similar to the shape and dimensions of the europium calibration source used previously; SRM 4276B-198. (see chapter 3), although they are not identical. The first step was the experimental absolute efficiency calibration of the prompt gamma site, at the irradiation position. This was done same as in chapter 3. The table 3.10 has all the information about the calibration source. The only difference is that time correction was 7723 days, instead of 7487 days, because this calibration took place on June 22nd 2004 (the previous one was on October 29th 2003). Furthermore, 6 peaks were omitted, because of bad counting statistics for them. Those were 86.6 keV ^{155}Eu peak and all five ^{125}Sb peaks. The next table and figure summarize the HPGe absolute efficiency calibration.

Isotope	Energy (keV)	Activity (c/s)	act error (c/s)	ε_{abs}	error ε_{abs}	% error
^{155}Eu	105.3	0.221	0.003	0.00067	0.0000111	1.67
^{154}Eu	123.1	3.146	0.007	0.00069	0.0000051	0.73
^{154}Eu	248	0.452	0.003	0.00059	0.0000052	0.88
^{154}Eu	591.7	0.198	0.002	0.00036	0.0000046	1.29
^{154}Eu	723.3	0.724	0.003	0.00032	0.0000025	0.76
^{154}Eu	873.2	0.369	0.003	0.00027	0.0000027	0.98
^{154}Eu	996.4	0.274	0.002	0.00024	0.0000032	1.34
^{154}Eu	1004.8	0.479	0.003	0.00024	0.0000022	0.92
^{154}Eu	1274.4	0.847	0.003	0.00022	0.0000016	0.71
^{154}Eu	1596.5	0.032	0.001	0.00016	0.0000037	2.29

Table 4.3: *Absolute efficiency calibration of the HPGe detector in prompt gamma cave*

The activity column represents the measured activity of the calibration source. Note that for example the absolute efficiency of this detector, for 996.4 keV line is about 73 times lower than the absolute efficiency of the detector used for foil counting, for the same line (see chapter 3). This is because of different experimental setup and much bigger distance from the source to the detector.

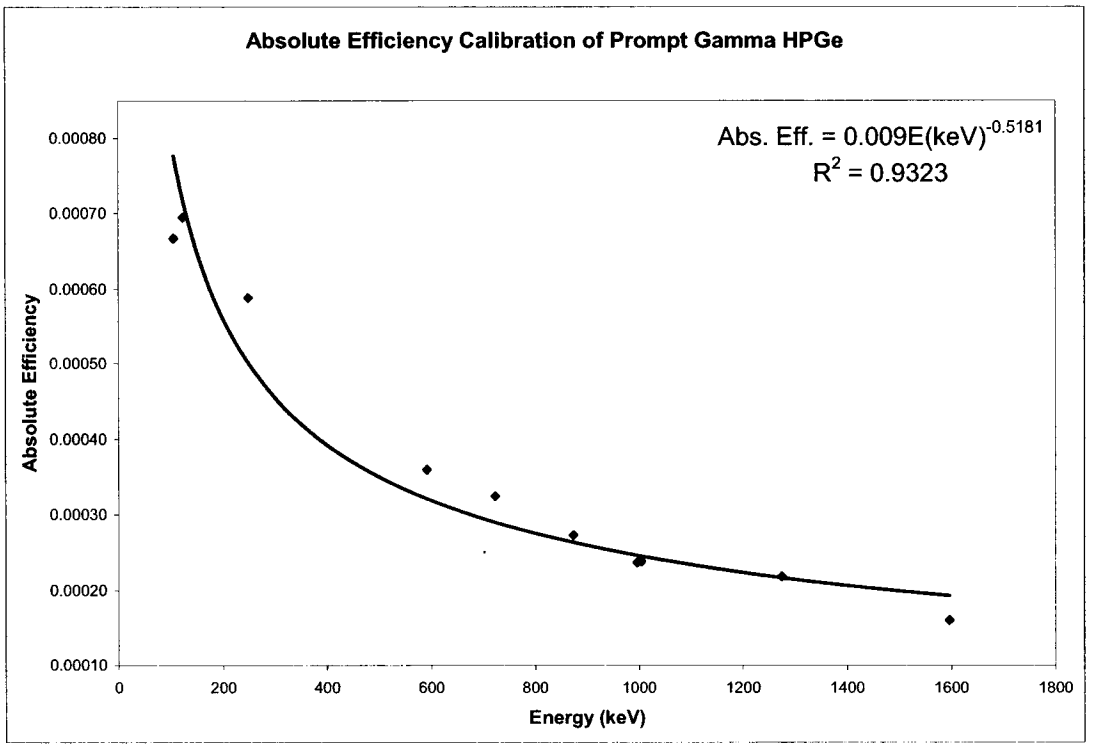

Figure 4.4: *Absolute efficiency calibration of the HPGe detector in prompt gamma cave*

According to the equation of the line, the absolute efficiencies for annihilation (511 keV) and prompt gamma hydrogen line (2.2 MeV) are 0.0003557 and 0.0001660, respectively. Based on experiments, (30 mL phantoms) count rates for these lines were 1848 ± 9 cps (hydrogen) and 127 ± 1 cps (annihilation), on average. This implies that when irradiated with prompt gamma site neutron beam, the 30 mL phantom emits (1.113 ± 0.005) × 10^7 photons/s (2.2 MeV hydrogen prompt gamma) and (3.57 ± 0.03) × 10^5 photons/s (annihilation), approximately. Using these two numbers, assumption that detector (window area 27.3258 cm^2) sees the 30 mL phantom as the isotropic point source and distance between the detector and the source (20.03 cm) we can approximate the number of photons that cross the detector window every second. This is given by the simple relation:

$$\phi = \frac{AS}{4\pi r^2} \quad \textbf{eq 4.1}$$

Where A is the area of detector window, S is the source strength (number of particular photons per second emitted from the source) and r is the distance between detector and the source. Putting all these parameters into the above equation, we get:

- annihilation (1936 ± 16) p/s

- 2.2 MeV line (60356 ± 271) p/s

The experimental intrinsic efficiency of the detector is obtained by dividing number of detector recorded pulses with number of events that cross the detector window. Using that, we can easily calculate the experimental intrinsic efficiencies of the detector for annihilation peak and 2.2 hydrogen prompt gamma line. They are 6.56 % and 3.06 %, respectively.

For this case, two MCNP runs were done. The first one gave us annihilation photon fluence rate and 2.2 MeV prompt gamma photon fluence rate that crosses the detector front window. This run took 7 h of computer time and it was f2 segmented tally that gave us the desired result. According to this run, the annihilation photon fluence rate entering the detector window is (101 ± 10) photons/cm^{2}s, 2.2 MeV prompt gamma photon fluence rate is (2683 ± 15) photons/cm^{2}s and finally, the total photon fluence rate that crosses the detector window (up to 2.5 MeV) is (4019 ± 13) photons/cm^{2}s. Therefore, using the area of the detector window, we can easily calculate the number of photons that cross the detector front window each second, by multiplying the detector window area with photon fluence rates

- (2.75 ± 0.27) × 10^3 p/s for annihilation

- $(7.33 \pm 0.04) \times 10^4$ p/s for 2.2 MeV hydrogen prompt gamma peak

- $(1.098 \pm 0.003) \times 10^5$ p/s for total

Comparing the experimental results and this MCNP run it is obvious that 4.62 % of annihilation photons and 2.52 % of 2.2 MeV prompt gamma hydrogen photons that cross the detector window are detected. These numbers are actually combined MCNP and experimental intrinsic efficiencies of the detector for 511 keV and 2.2 MeV respectively. Obviously, they are slightly lower than previously calculated pure experimental intrinsic efficiencies (6.56 % and 3.06 %). However, combined MCNP and experimental are probably more accurate than pure experimental, because we made several assumptions in our calculations and the most important thing is that we did not assume any shielding between the detector and the source.

The second MCNP run was tallied for the total number of photons emitted from the 30 mL water phantom, while irradiated in the prompt gamma cave. The approach to this problem was very simple; the sphere with radius of 3 cm was located around the sample and photon fluence rate was tallied on that sphere, using f2 tally. The sphere area is 113.04 cm^2 and photon fluence rate for different photon energies (2.2 MeV and annihilation) was multiplied with this area in order to get total number of photons per second emitted from the sample. After 210 min MCNP run, the following results were obtained:

- annihilation peak: (504.78 ± 3.3) p/cm^2s; which is $(5.71 \pm 0.04) \times 10^4$ p/s

- 2.2 MeV hudrogen peak: (139437 ± 90) p/cm^2s; which is $(1.576 \pm 0.001) \times 10^7$ p/s

- total: (199514 ± 110) p/cm^2s; which is $(2.255 \pm 0.001) \times 10^7$ p/s.

Comparing the above two MCNP runs, the conclusion can be drawn that about 0.465 % of 2.2 MeV hydrogen prompt gamma photons emitted from the sample, actually cross the detector window, as well as 4.82 % of annihilation photons. The other comparison can be made between the second MCNP run and experimental results for annihilation and 2.2 MeV photons. See the above results. It was found that experimental 2.2 MeV photon emission rate is about 29 % lower and experimental annihilation emission rate is 86 % higher than corresponding MCNP simulated rate. These results are reasonable and they show good agreement between calculated and simulated values, even though the differences are 29 and 86 %. These differences are predominantly due to calculated absolute efficiency calibration line and assumption that calibration source has the same geometry as the 30 mL irradiated phantom. The differences would be negligible if the calibration was more precise, i.e. if the calibration source was made to be geometrically identical as the 30 mL phantom and if those calibration isotopes were dissolved in 30 mL of water. The improvements in experimental absolute efficiency detector calibration will be the important part of the future research. Other than that, this combination of MCNP runs and experimental results showed clearly that MCNP runs give us reasonable and valuable results and what is the most important, the multiplier constants and the source definition are valid, for now.

ii) MCNP Neutron and Gamma Exposure Survey Inside the Prompt Gamma Cave

This MCNP exercise will give the neutron dose rate and secondary gamma exposure rate in the prompt gamma cave, when neutron beam is on. The neutron dose rate will be calculated in mrem/h and gamma exposure rate will be calculated in mR/h. These values are observed using f4 type tally (#/cm^2, fluence averaged across a cell). In

order to get f4 type tally, it is required to make a cell, where this tally is observed. There were nine rectangular cells added to original geometry. They were all filled with air. Every cell had rectangular basis with beam dimensions (2.54 × 5.08) cm^2 and height of 2 cm. The central cell was located directly in the beam at zero x position and it covered the beam completely. The rest of the cells were located around the central cell at the vicinity of the beam. Therefore, they made a mesh of 8 cells around the central cell, which covered the beam completely. Furthermore, conversion tables from fluence rate to dose were used for neutrons and photons, as well as multiplier constants (fm4 values) in order to get appropriate units for f4 tallies, ie. mrem/h and mR/h. The conversion tables are:

- neutrons: *NCRP 38 (10CFR835) Dose Equivalent per Unit Fluence*
- photons: *Conversion Coefficients for Air Kerma per Unit Fluence (ICRP 74)*

The multiplier constants (fm4) are calculated in a following way:

$$\phi = \frac{2.653 \times 10^7 \, n/cm^2 s \times 1.013}{0.9994} \times (5.08cm \times 2.54cm) = 3.47 \times 10^8 \, n/s$$

This value represents the total neutron output per second, for complete source (area = 5.08 × 2.54 cm^2), where 1.013 is normalization constant explained before in the chapter and the division with 0.9994 indicates the total neutron fluence rate, including 0.06 % of epithermal neutrons. For neutron tallies, the fm4 is further calculated:

$$fm4 = \left(\frac{pSv}{s}\right)\left(\frac{s}{n}\right)\left(3.47 \times 10^8 \frac{n}{s}\right)\left(100\frac{rem}{Sv}\right)\left(10^{-9}\frac{mSv}{pSv}\right)\left(3600\frac{s}{h}\right) = 124908.12\frac{mrem}{h}$$

For photon tallies, the fm4 is further calculated:

$$fm4 = \left(\frac{rad}{s}\right)\left(\frac{s}{n}\right)\left(\frac{1}{0.876}\frac{R}{rad}\right)\left(1000\frac{mR}{R}\right)\left(3.47\times10^{8}\frac{n}{s}\right)\left(3600\frac{s}{h}\right) = 1.426\times10^{15}\frac{mR}{h}$$

The results of this MCNP run are presented in the 3×3 table below. Note that every table cell represents the actual cell where f4 tally was observed. The middle cell covers the neutron beam completely. The MCNP run had 5.5 × 10^8 histories, what was approximately 775 minutes of computer time.

28.598 ± 0.026 mrem/h 1.416 ± 0.012 mR/h **cell # 1**	35.279 ± 0.024 mrem/h 1.738 ± 0.011 mR/h **cell #2**	28.395 ± 0.026 mrem/h 1.944 ± 0.010 mR/h **cell #3**
53.417 ± 0.018 mrem/h 1.993 ± 0.011 mR/h **cell # 4**	97963 ± 0 mrem/h 3.363 ± 0.008 mR/h **cell # 5**	53.653 ± 0.018 mrem/h 2.571 ± 0.009 mR/h **cell #6**
29.936 ± 0.026 mrem/h 1.644 ± 0.011 mR/h **cell #7**	36.571 ± 0.024 mrem/h 1.989 ± 0.010 mR/h **cell #8**	29.385 ± 0.026 mrem/h 2.196 ± 0.009 mR/h **cell # 9**

Table 4.4: *Neutron dose rates and gamma exposures in prompt gamma cave at various positions*

Another MCNP run was performed, but this time, f4 tally was sampled in only one cell, that was actually made of previous nine cells. It was found out that neutron dose rate corresponding to that cell was 10918 ± 0 mrem/h and gamma exposure was 2.088 ± 0.010 mR/h. Summing all neutron dose rates and all gamma exposure rates from the above table and averaging it over 9 cells, we obtain 10918 ± 0 mrem/h and 2.095 ± 0.010 mR/h for neutrons and photons respectively. Obviously, this is in agreement with a sampling f4 tally in a single cell. Finally, one more MCNP run was performed, with the identical 9 sampling cells (same as in the first run), but this time the source was changed slightly. The area of the source was increased 4 times, so it covered cell # 5 completely

(as before) and it partially covered the rest of the cells. Obviously fm4 constants for photons and neutrons were multiplied by 4. Again, focusing on central cell (cell # 5), this MCNP run gave neutron dose rate of 98018 ± 6 mrem/h and gamma exposure rate of 9.65 ± 0.07 mR/h. Obviously, neutron dose rate is slightly increased, compared to the first run (table 4.3, cell # 5) and gamma exposure is increased about 3 times, but still negligible, compared to the neutron dose rate. This insignificant neutron dose rate increment is due to the increased scatter of neutrons in the air, since source area is increased. The same can be argued for secondary gamma exposure rate.

From these three MCNP runs, it can be concluded that the highest gamma exposure rate of 3.363 ± 0.008 mR/h (cell # 5) is negligible, ie. the possible patient could spend a significant amount of time in the beam without potential hazard. However, this is not the case with neutron dose rate in the beam. Obviously it is approximately 100 rem/h, which is 1 Sv/h of neutron dose rate (cell # 5), over the area of 12.9 cm^2 (5.08 × 2.54) cm^2. Taking into the account the results obtained in the previous section (*Detector Pulse Analysis)*, it is obvious, that multiplier constants are valid and that this is indeed the neutron dose rate in the beam over the area of the neutron beam. Furthermore, this can be checked by the simple calculation, using the total neutron fluence rate; 2.689×10^7 n/cm^2s and using the conversion factor of 10.21 $pSvcm^2$ for thermal neutrons. This is taken from the table used in our MCNP calculations; *dose equivalent per unit fluence (NCRP 38)*. Therefore, by multiplying these two numbers, we get the neutron dose rate of 0.988 Sv/h, which is in total agreement with MCNP calculations. This is further argued and discussed in the next chapter.

CHAPTER V

Discussion of the Results and Future Research

Since this was the first project of this kind done on the beam port # 4 at McMaster Nuclear Reactor, it is reasonable to conclude, after two years of research and a thesis written, that every aspect and part of the project could be improved, or at least done with the different approach or different technique and those results could be compared with the results presented in this project. This thesis showed that there are lots of open possibilities and ways for approaching the problem of in vivo prompt gamma nuclear activation analysis at the MNR. As it is done in this project, the improvements and future research could start from the very beginning. In other words, the possible future research will include the ***deeper exploration of the neutron beam*** and improvements of in vivo prompt gamma analysis, which include:

- ***geometrical rearrangement of the shielding at the site***
- ***improvement of the detection system***
- ***accurate neutron and gamma dosimetry***
- ***rearrangement of the complete site in order to accommodate the possible patient***

The Monte Carlo simulations, using MCNP program will be the most important tool in preliminary assessments and anticipations for the future research.

5.1 Neutron Energy Spectrum Determination

This project showed that the neutron beam used, is predominantly made of thermal neutrons (99.94 %). The properties of the neutron beam were determined using both experimental techniques and MCNP simulations. The neutron spectrum obtained gave us reasonable agreement between further MCNP calculations and experimental results. However, looking from this perspective, a few things could be done in order to improve our knowledge about the neutron spectrum and to rule out most of uncertainties and possible false assumptions. The first and the simplest thing that could be done is the check for the neutron beam collimation. This project assumed totally collimated neutron beam and that fact was used in creation of the MCNP sdef card (vec = 0 0 1 and dir = 1). The collimation of the neutron beam could be checked using neutron radiography films. These films could be located at various places in the neutron beam (different distances from the neutron output) and the shape and dimensions of the photographed neutron beam cross section could be observed in order to see if the rectangular beam diverges as the distance from the beam output increases. If this was the case, then sdef card would be changed in order to accommodate this divergence and of course, the MCNP neutron dose rate (1 Sv/h – chapter 4) would significantly decrease at the point of observation, since neutron fluence rate decreases with the distance in the diverging beam. This is analogous to neutron isotropic point source, where the neutron fluence rate decreases as: $C/4\pi r^2$, where C is the constant. Another important thing concerns the neutron spectrum itself. The neutron spectrum could be obtained by the foil irradiation, but this time, the foils could be irradiated in the reactor pool in front of the beam tube # 4 entrance. This would give us all 3 portions of the neutron spectrum (thermal, epithermal and fast). The neutron

spectrum unfold could be done using ASTM calculations or SAND II code simulations **[Kennedy]**. After that, the unfolded spectrum would be the input spectrum for MCNP run, that would be carried through the simple geometry of the beam tube # 4 (figure 2.2). Finally the output, tallied spectrum would be the new input spectrum for MCNP prompt gamma analysis. This approach to the neutron spectrum determination would completely rule out any assumptions or concerns like: if there are any fast neutrons present in the neutron spectrum, or if the obtained spectrum is indeed the one. Furthermore, the relative neutron output could be monitored on regular basis, every operational day in the week, using fission chamber located at the entrance of the beam port # 4, in order to check the power and neutron fluence daily fluctuations. This would be exceptionally important when fuel change is done and the core configuration is changed.

5.2 The Improvements of in vivo Prompt Gamma Analysis

The first thing that comes into mind, after finishing all irradiation experiments with water phantoms (polyethylene bottles) is that the phantoms for the future research have to be more realistic. It means that they have to simulate human body more closely. For example, for irradiating kidneys and liver there should be a big phantom, filled with water that simulates the human torso and two smaller phantoms located at the liver and kidney's positions. Those phantoms would simulate these two. Of course, the targeted organs would be liver and kidneys and the trace element solution should be there.

The aim of every in vivo activation analysis project is to create the best possible detection system (the lowest MDL obtained) and to minimize the neutron and gamma doses received by the patient. This project showed that with the present detection

configuration, the cadmium MDL's for different phantoms (30 mL – 2 L) are less than 1 ppm (see table 3.17) and MDL's for mercury and boron for 30 mL phantom are (16.91 ± 0.05) ppm and (0.31321 ± 0.00002) ppm, respectively. These are relatively low concentrations and very small MDL's, but they cannot be taken as reasonable values, taking into the account that they are in direct relationship with the neutron and gamma dose received by the patient. This means that in order to detect the lowest possible concentration of any element, with any detection system, the irradiation time has to be increased in order to get reasonable counting statistics. The increased irradiation time directly increases the neutron and gamma dose received by the patient. Therefore, by lowering MDL, the neutron and gamma doses are increased. For example, from our experiments, in order to get reasonable counting statistics for cadmium phantoms, for 1 ppm, the irradiation time was 30 min, also it was 10 min and 20 min for 50 ppm mercury and 1 ppm boron phantoms, respectively. Obviously these values are higher than MDL's calculated for all three elements. Therefore, in order to achieve these MDL's, the irradiation times had to be even bigger than these maximum times. The aim for the future research should be the achievement of the proposed MDL's, with the reasonable counting statistics (less than 5 % uncertainty) in 5 minutes counting time. According to MCNP calculation done in chapter 4, this (5 minutes spent in the neutron beam) would give the patient 81.64 mSv of neutron field exposure over the area of the neutron beam (see table 4.3). Of course, this achievement of good statistics (5 minutes counting time, for 1 ppm phantoms), require the significant lowering of the background count. The background count lowering can be achieved by rearrangement of the experimental site, i.e. introduction of the new elements to the detection system. As mentioned before, every

geometrical change of the experimental site will be strictly checked, beforehand, with the most powerful tool – MCNP calculations. One of the solutions is the introduction of another HPGe **[Ember]**, or combination of two NaI detectors **[Gardner]**, for coincidence counting. This solution requires a complete rearrangement of the prompt gamma experimental site; drastically increasing the site's area and volume, because another (mirror image) massive detector shielding would have to be constructed at the site. However, this might interfere with the other projects and work at the MNR, especially with the project at the beam port # 3, therefore, this could be a huge obstacle for creating coincidence counting unit at the beam port # 4. Another solution for background lowering is the introduction the NaI Compton suppression annular crystal around the present HPGe. This solution will not require any enlargement of the prompt gamma experimental cave and it would be probably the first step toward the task of lowering the background count in this experimental environment. According to the ORTEC NaI Compton suppression crystal manual, this might reduce the background more than 10 times.

Obviously, this project deals with prompt gamma analysis, however, the experimental site has excellent properties for in vivo delayed gamma analysis of the elements with short half lives, like aluminum (2.25 min). The idea is to irradiate phantom or patient's hand **[Pejovic-Milic]** at the irradiation position, for appropriate amount of time. After that, without removing the sample, the shutter will be closed (neutron beam cut) and the count could start immediately.

As mentioned before, the most important problem in this project is the neutron dose rate inside the cave. From MCNP calculations, it was found that gamma exposure

was not the big issue, but neutron dose rate raises some serious concerns. It was found that for 5 min exposure time, the patient is in the time integrated field of 81.64 mSv over the area of the neutron beam (2.54 × 5.08) cm^2. Obviously, effective patient dose was not calculated in this project, but some comparisons can be made with previously done projects. For example, the hand dose in Palerme's MSc thesis (MNR, beam port # 2) was found to be 43 mSv and hand dose in Pejovic-Milic's MSc thesis (accelerator) was found to be 9 mSv. If our 81.64 mSv was approximated as the hand dose, it would be approximately the double of the hand dose in Palerme's thesis. Probably the most reasonable comparison should be with the preliminary work of Joanna Grinyer, the PhD student at Medical Physics Unit. She is currently working on prompt gamma detection of cadmium, using ^{238}Pu/Be source. The neutron fluence rate from this source at the point of interaction is in the order of 10^5 n/cm^2s. These neutrons are predominantly fast. Grinyer's the most current results indicate the 30 min cumulated neutron dose of 0.4 mSv, for both kidney and liver measurements (measured by the "Snoopy" neutron detector). Furthermore, her results showed MDL of 1.75 mg for the kidney (125 mL phantom) and 3.3 ppm for liver (2 L phantom). Using these results and equivalent results from this project (see table 3.17), we can compare them, simply by inserting them into the relationship MDL × $(Dose)^{1/2}$. This is normalized MDL and the purpose of doing this is simple comparison of these values for different experimental settings. Substituting Grinyer's values into the normalized MDL equation, we obtain 1.107 $mg(mSv)^{1/2}$ and 2.087 $ppm(mSv)^{1/2}$ for 125 mL and 2 L phantoms respectively. Now, using table 3.17 and MCNP calculated neutron dose for 5 min measurements (81.64 mSv), we can estimate the normalized MDL for this project. Therefore, for 125 mL phantom, the

normalized MDL is 0.285 mg$(mSv)^{1/2}$ and for 2 L phantom it is 7.281 ppm$(mSv)^{1/2}$. Furthermore, we can calculate the same normalized MDLs for exposure of 30 min. This is more realistic exposure for the present system, since good statistics for 1 ppm (lowest concentration) cadmium phantoms was obtained when phantoms were irradiated for 30 min. The exposure of 30 min would give us MCNP neutron dose of 489.815 mSv. Hence, substituting that value and values from table 3.17, we get 0.697 mg$(mSv)^{1/2}$ and 17.834 ppm$(mSv)^{1/2}$ for 125 mL and 2 L phantoms respectively. Obviously, compared to Grinyer's work, this project gave the better normalized MDL for 125 mL phantom, for both 5 and 30 min measurements (0.285 and 0.697 compared to 1.107) and much worse results for 2 L phantom (7.281 and 17.834 compared to 2.087). This could be due to the fact that our experimental site was particularly designed for small sample analysis, therefore, smaller the sample, better the obtained results. Furthermore, the fact that MDLs from Grinyer's work decrease as the phantom size increases, which is totally opposite pattern from the one observed in this project (see table 3.17, last column) further confirms the above argument. However, regardless how good normalized MDL for 125 mL phantoms happens to be, there is a still a reasonable problem of high neutron dose in the cave and that will be one of the most important issues in the future work.

As mentioned, more work has to be done in the future in order to fully asses the neutron and gamma doses. The MCNP calculated neutron dose rate relies mostly upon the description of the neutron field in sdef card. As discussed, the neutron field is described without any divergence in the beam. If the preliminary results in the future research show that there is an even a small diverging property of the rectangular beam, the dosimetry calculations will become more reasonable and simulated neutron dose will

drop. However, in the future work, the dosimetry calculations will not be based on MCNP results, they would rather be done using microdosimetry techniques and physical dose measurements, using the calibrated neutron dosemeters **[Aslam]**.

APPENDIX A

A1 Derivation of the Equations for Calculation of Thermal Neutron Fluence Rate (basics and advanced):

Note that the derivation of the flux perturbation factor F_1 closely follows a book: **"Technical Reports Series, No.107, Neutron Fluence Measurements"**. These theories and method, or variations of them were also confirmed in Kruger's **"Principle of Activation Analysis"** and Master's thesis by John Kennedy: **"A Comparison of McMaster Nuclear Reactor Irradiation Experiments With Simulation"**. Furthermore, the theory was used by Hertel and Sweezy, Georgia Institute of Technology in their: **"Neutron Flux Measurements by Activation Analysis"**.

The production and decay equation is given by:

$$\frac{dN_A(t)}{dt} = RN_T(0) - \lambda N_A(t) \qquad \textbf{eq A1}$$

Where

- $N_A(t)$ is total # of product nuclei as a function of time
- $R = \sigma\varphi$, reaction rate,
- $N_T(0)$ is the total number of target nuclei in the sample. We also assume that number of new nuclei produced $N_A(t)$, during the time of neutron bombardment is negligible compared to total number of parent nuclei in the sample, $N_T(0)$. It means that incoming neutron beam (neutron fluence rate, φ_0), "sees" the constant number of target nuclei during the bombardment, even though some of them are transformed due to interaction with incoming neutron. The number of transformed nuclei is negligible. That is why we can easily say that the rate of production R is constant during the irradiation period.

Solving the equation further, we get:

$$\frac{dN_A(t)}{RN_T(0)-\lambda N_A(t)} = dt \qquad \textbf{eq A2}$$

$$\int_0^{N_A(t)} \frac{dN_A(t)}{RN_T-\lambda N_A(t)} = \int_0^t dt \qquad \textbf{eq A3}$$

$$-\frac{1}{\lambda}\ln\left(RN_T(0)-\lambda N_A(t)\right)^{N_A(t)}_0 = t \qquad \textbf{eq A4}$$

$$\ln\frac{RN_T(0)-\lambda N_A(t)}{RN_T(0)} = -\lambda t \qquad \textbf{eq A5}$$

Finally, the change of product nuclei per time during the irradiation time is given by:

$$N_A(t) = \frac{RN_T(0)}{\lambda}\left(1-e^{\lambda t}\right) \qquad \textbf{eq A6}$$

And the activity of the sample during the irradiation time is given by:

$$A_A(t) = \lambda N_A(t) \qquad \textbf{eq A7}$$

So, the activity of the sample is:

$$A_A(t) = RN_T(0)\left(1-e^{-\lambda t}\right) \qquad \textbf{eq A8}$$

Therefore, the activity is given by:

$$A_A(t) = \varphi\sigma N_T(0)\left(1-e^{-\lambda t}\right) \qquad \textbf{eq A9}$$

Note that this is the activity of the sample during the irradiation (neutron bombardment) time. As soon as irradiation is stopped, the activity of the irradiated sample behaves like simple exponential decay with the equation:

$$A_A(t) = A_0 e^{-\lambda t} \qquad \textbf{eq A10}$$

Where:

$$A_0 = A_A(t_{irr}) \quad \textbf{eq A11}$$

$A_A(t_{irr})$ is the activity of the sample at the end of irradiation period. Therefore, activity after irradiation and after some time t, would read:

$$A_A(t) = \varphi\sigma N_T(0)\left(1 - e^{-\lambda t_{irr}}\right)e^{-\lambda t} \quad \textbf{eq A12}$$

This is general equation, but neutron fluence rate is continuous, energy dependant quantity that is spanned between 10^{-2} to 10^{7} eV (9 orders of magnitude). Therefore in general case, we use the average neutron fluence rate, that is, neutron fluence rate integrated over whole energy range:

$$\bar{\varphi} = \int_0^{\infty} \bar{\varphi}(E)dE \quad \textbf{eq A13}$$

One of the goals of this project is to try to specify this energy spectrum, as good as possible ie. try to distinguish between thermal, epithermal and fast neutron fluence rates. As it was said above, we start with thermal region of the spectrum, where neutron fluence rate is integrated between zero energy and cadmium cut-off energy:

$$\varphi_0 = \int_0^{E_{Cd}} \varphi_0(E)dE \quad \textbf{eq A14}$$

The cadmium cut-off energy, E_{Cd} is described in theory section. Hence, our equation A12 will become:

$$A_A(t) = N_T(0)\bar{\varphi}\sigma f(t_{irr}, t) \quad \textbf{eq A15}$$

Where $f(t_{irr},t)$ is just exponential part of the equation 12. Again, our goal is to find φ_0, the thermal portion of the neutron fluence rate, therefore we can modify equation A15 into:

$$A_A(t) = N_T(0)\varphi_0 F_1 \sigma_0 f(t_{irr}, t) \quad \textbf{eq A16}$$

Where σ_0 is thermal cross section for particular element and F_1 is simply factor that is given by:

$$F_1 = \frac{\bar{\varphi}}{\varphi_0} \quad \textbf{eq A17}$$

Factor F_1 is called a flux (neutron fluence rate) perturbation factor and it is different for different target elements and different media. This factor can be broken down into two parts, the coefficient of self shielding, G and the coefficient of flux depression H:

$$F_1 = GH \quad \textbf{eq A18}$$

The coefficient of self shielding, G is the ratio of the mean neutron fluence rate in the detector (irradiation foil), to the neutron fluence rate at the surface of the detector, and the coefficient of flux depression, H, is defined as the ratio of the fluxes at the surface of the detector placed in the medium and the flux prior to the insertion of the detector:

$$G = \frac{\bar{\varphi}}{\varphi_s} \quad \textbf{eq A19} \text{ and } \quad H = \frac{\varphi_s}{\varphi_0} \quad \textbf{eq A20}$$

As this might become obvious later, factor G represents the property of the detector material and factor H represents the property of the medium of interaction.

See the figure below:

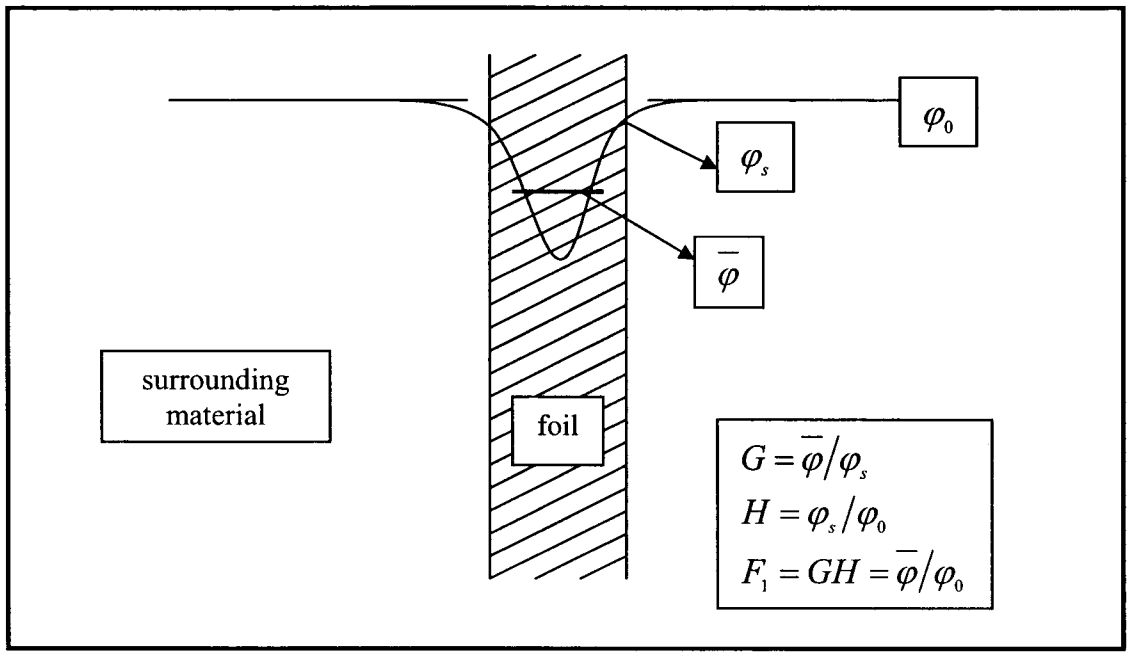

Figure A1: *Fluence rate depression and self shielding parameters; Source:* ***"Neutron Fluence Measurements"****, Technical Reports Series # 107*

Furthermore, the self-absorption factor G is described as a probability that that the neutrons entering the sample will not be captured in it. If we have pure absorbing, each collision represents the capture and we have:

$$G = P_0 = 1 - P_c \qquad \textbf{eq A21}$$

However, we cannot say that we have absolutely absorbing samples and the equation A21 is modified to:

$$G = P_0 = \frac{1 - P_c}{1 - P_c\left(1 - \frac{\Sigma_c}{\Sigma_t}\right)} \qquad \textbf{eq A22}$$

Where, Σ_c and Σ_t are macroscopic capture and total cross sections, respectively. Parameter P_c is given in equations:

$$1 - P_c = \frac{1}{2x}\left(1 - 2E_3(x)\right) \quad \textbf{eq A23 and } x = \Sigma_t a \quad \textbf{eq A24}$$

$$a = \frac{2V}{S} \quad \textbf{eq A25}$$

Where, V and S are volume and surface area of the foil (sample). Function $E_3(x)$ is given by the expression:

$$E_n(x) = \int_1^\infty e^{-xu} u^{-n} du \quad \textbf{eq A26}$$

Therefore, $E_3(x)$ will read:

$$E_3(x) = \int_1^\infty \frac{e^{-xu}}{u^3} du \quad \textbf{eq A27}$$

The value of this definite integral, for known value of x is easily calculated using **"Maple software"**.

Now, calculation of H factor is given here, but since our medium is air (sample is irradiated in the air), H can be approximated as 1. Therefore, $F_1 = G$. Factor H is given by:

$$H = \frac{1}{1 + g\Sigma_c aG} = \frac{1}{1 + gx\frac{\Sigma_c}{\Sigma_t}G} \quad \textbf{eq A28}$$

Where:

$$g = \frac{4}{\pi}\frac{r}{\lambda_t}\left[1 - \frac{3\pi}{16}\frac{r}{L}\right] - K\left(\frac{2r}{\lambda_t}, \gamma\right) \quad \textbf{eq A29}$$

There are several methods used in obtaining g (the only unknown coefficient equation A28). However, they will not be mentioned here, simply because, it was assumed that H = 1 and it was not used in the calculations throughout this project.

A2 The Derivation of the Equations for Calculations of the Fast Neutron Fluence Rate

The content of the first section of appendix A, deals only with calculations of the absolute value for the thermal neutron fluence rate. The calculations for resonance neutron fluence rates are described in chapter 3. This part of appendix A will give some basic ideas of calculating fast neutron fluence rates based on results obtained by threshold detectors. The obvious reason why this project will just scratch the surface of these calculations is because our experiments with threshold foils showed no presence of fast neutrons in the beam. Therefore, it was assumed that fast neutron fluence rate was negligible. The equations and derivation in this part of appendix A are primarily based on: **"Technical Reports Series, No.107, Neutron Fluence Measurements"** and Master thesis by J. Kennedy **"A Comparison of McMaster Nuclear Reactor Irradiation Experiments With Simulation".**

The equations for calculating fast neutron fluence rate will be very similar to the equations that were used for thermal neutron fluence calculations. Of course, there will be some modifications. Therefore, for the fast neutron fluence rate we will use the equation:

$$\varphi_0 = \frac{A_{tot}}{\varepsilon I_\gamma a N \sigma(E_i) F_1 \left(1 - e^{-\lambda t_{irr}}\right)} \qquad \textbf{eq A30}$$

A_{tot} represents the absolute activity of the previously irradiated threshold foil (produced isotope of interest). This is actually the activity right after the end of the neutron bombardment. Obviously, the only change would be the cross section. In

thermal calculations, we simply had σ_0, thermal cross section. In this case we have $\sigma(E_i)$, effective cross section. **[Technical Reports, 107]**. The effective cross section is given by:

$$\sigma(E_i) = \frac{\int_0^{\infty} \sigma(E)\varphi(E)dE}{\int_{E_i}^{\infty} \varphi(E)dE} \qquad \textbf{eq A31}$$

In the above integral relationship, E_i represents the threshold energy and $\varphi(E)$ represents the fission spectrum. This is an analytical function and it could be represented by any of the three functions, explained in chapter 1 (equations 1.1, 1.2, 1.3); $\sigma(E)$ is the energy dependent cross section for the threshold reaction of interest. These are discrete functions and are taken from ENDF files, Brookhaven labs. The graphs of these functions, for reactions of interest, are given in chapter 2. See figures: 2.8, 2.9, 2.10, 2.11, 2.12. Value $\sigma(E_i)$ can be calculated using numerical integration, or it can be taken from Brookhaven web site.

APPENDIX B

This appendix section deals with calculations of experimental error propagation for some major experimental results obtained in this project. These calculations are primarily based on P. Bevington's book: **"Data Reduction and Error Analysis for the Physical Sciences"**, and G. Knoll's book: **"Radiation Detection and Measurements"**.

B1 Error propagation for ϕ_r/ϕ_{th} results:

The equation for ϕ_r/ϕ_{th} ratio is given by:

$$\frac{\phi_r}{\phi_{th}} = \frac{(\sigma_0 \pm \delta\sigma_0)}{(I_{tot} \pm \delta I_{tot})\left(\frac{CR \pm \delta CR}{CR_{Cd} \pm \delta CR_{Cd}} - 1\right)} \qquad \textbf{eq B1}$$

Let:

$$\left(\frac{CR \pm \delta CR}{CR_{Cd} \pm \delta CR_{Cd}} - 1\right) = B \pm \delta B \qquad \textbf{eq B2}$$

So we have:

$$\delta\left(\frac{\phi_r}{\phi_{th}}\right) = \frac{\sigma_0}{I_{tot} B}\sqrt{\left(\frac{\delta\sigma_0}{\sigma_0}\right)^2 + \left(\frac{\delta I_{tot}}{I_{tot}}\right)^2 + \left(\frac{\delta B}{B}\right)^2} \qquad \textbf{eq B3}$$

Where:

$$B = \frac{CR}{CR_{Cd}} - 1 \qquad \textbf{eq B4 and } \delta B = \frac{CR}{CR_{Cd}}\sqrt{\left(\frac{\delta CR}{CR}\right)^2 + \left(\frac{\delta CR_{Cd}}{CR_{Cd}}\right)^2} \qquad \textbf{eq B5}$$

And:

$$\left(\frac{\delta B}{B}\right)^2 = \left[\frac{\frac{CR}{CR_{Cd}}\sqrt{\left(\frac{\delta CR}{CR}\right)^2 + \left(\frac{\delta CR_{Cd}}{CR_{Cd}}\right)^2}}{\frac{CR}{CR_{Cd}} - 1}\right]^2 \qquad \textbf{eq B6}$$

After doing some rearrangement in the main bracket:

$$\left(\frac{\delta B}{B}\right)^2 = \left[\left(\frac{\delta CR}{CR}\right)^2 + \left(\frac{\delta CR_{Cd}}{CR_{Cd}}\right)^2\right]\left(\frac{CR}{CR - CR_{Cd}}\right)^2 \qquad \textbf{eq B7}$$

And finally:

$$\delta\left(\frac{\phi_r}{\phi_{th}}\right) = \frac{\sigma_0}{I_{tot}\frac{CR - CR_{Cd}}{CR_{Cd}}}\sqrt{\left(\frac{\delta\sigma_0}{\sigma_0}\right)^2 + \left(\frac{\delta I}{I_{tot}}\right)^2 + \left(\frac{CR}{CR - CR_{Cd}}\right)^2\left[\left(\frac{\delta CR}{CR}\right)^2 + \left(\frac{\delta CR_{Cd}}{CR_{Cd}}\right)^2\right]}$$

eq B8

B2 Error Propagation for Absolute Efficiency Calculations:

Chapter 3, section 3.5 deals with the calculation of the absolute efficiency of the HPGe detector used for foil counting. The calculations for simple error propagation for this section of chapter 3 are given below. The absolute efficiency, ε_{abs} of the detector is given by:

$$\varepsilon_{abs} = \frac{A_{meas} \pm \delta A_{meas}}{A_{calc} \pm \delta A_{calc}} \qquad \textbf{eq B9}$$

Where A_{meas} is measured foil activity and A_{calc} is calculated foil activity. The error in absolute efficiency is given by:

$$\delta\varepsilon_{abs} = \frac{A_{meas}}{A_{calc}}\sqrt{\left(\frac{\delta A_{meas}}{A_{meas}}\right)^2 + \left(\frac{\delta A_{calc}}{A_{calc}}\right)^2} \qquad \textbf{eq B10}$$

B3 Error Propagation in Thermal Fluence Rate Calculations

Equation 3.14 was used for the thermal fluence rate calculations. This equation reads:

$$\varphi_0 = \frac{A_{tot} - A_{epi}}{\varepsilon I_\gamma a N \sigma_0 F_1 \left(1 - e^{-\lambda t_{irr}}\right)} \qquad \textbf{eq B11}$$

As mentioned before, uncertainty values are associated to A_{tot}, A_{epi}, and σ_0 values. Therefore, the error propagation for φ_0 would be:

$$\delta\varphi_0 = \frac{A_{tot} - A_{epi}}{\varepsilon I_\gamma a N \sigma_0 F_1 \left(1 - e^{-\lambda t_{irr}}\right)}\sqrt{\left(\frac{\delta A_{tot}}{A_{tot}}\right)^2 + \left(\frac{\delta A_{epi}}{A_{epi}}\right)^2 + \left(\frac{\delta \sigma_0}{\sigma_0}\right)^2} \qquad \textbf{eq B12}$$

B4 Estimated Error of the Mean

For all mean calculations and estimated error of the mean throughout this project, the simple average formulas were used **[Bevington]**. Therefore, the mean is calculated using the formula:

$$\bar{x} = \frac{\sum_{i=1}^{n} x_i}{n} \qquad \textbf{eq B13}$$

Estimated error of the mean is calculated using the formula:

$$\bar{\delta} = \frac{\sqrt{\sum_{i=1}^{n} \delta_i^2}}{n} \qquad \textbf{eq B14}$$

B5 Weighted linear Least Square Fit

For fitting the straight lines, for MDL determination, the weighted least square fit was used, since uncertainties in number of counts were not equal. The Bevington's textbook was used for these exercises, as well. The straight line is given by:

$$y = a + bx \quad \textbf{eq B15}$$

Where:

$$a = \frac{1}{\Delta}\begin{vmatrix} \sum \frac{y_i}{\sigma_i^2} & \sum \frac{x_i}{\sigma_i^2} \\ \sum \frac{x_i y_i}{\sigma_i^2} & \sum \frac{x_i^2}{\sigma_i^2} \end{vmatrix} \quad \textbf{eq B16}$$

$$b = \frac{1}{\Delta}\begin{vmatrix} \sum \frac{1}{\sigma_i^2} & \sum \frac{y_i}{\sigma_i^2} \\ \sum \frac{x_i}{\sigma_i^2} & \sum \frac{x_i y_i}{\sigma_i^2} \end{vmatrix} \quad \textbf{eq B17}$$

$$\Delta = \begin{vmatrix} \sum \frac{1}{\sigma_i^2} & \sum \frac{y_i}{\sigma_i^2} \\ \sum \frac{x_i}{\sigma_i^2} & \sum \frac{x_i^2}{\sigma_i^2} \end{vmatrix} \quad \textbf{eq B18}$$

Also, uncertainties in the slope and y intercept are given by:

$$\sigma_a^2 \approx \frac{1}{\Delta} \sum \frac{x_i^2}{\sigma_i^2} \quad \textbf{eq B19}$$

$$\sigma_b^2 \approx \frac{1}{\Delta} \sum \frac{1}{\sigma_i^2} \quad \textbf{eq B20}$$

REFERENCES

Arnold M. Development of an Accelerator Based System for In Vivo Neutron Activation Analysis Measurements of Manganese in Humans. PhD Thesis. McMaster University (2000)

Aslam. Spectroscopy and Dosimetry for Accelerator Based In Vivo Measurements. PhD Thesis. McMaster University (2003)

Bevington P.R. Data Reduction and Error Analysis for the Physical Sciences. First Edition. McGraw-Hill, Inc. (1969)

Brookhaven National Laboratories. Evaluated Nuclear (reaction) Data File (ENDF). Retrieved from: http://www.nndc.bnl.gov/endf/index.html

Brookhaven National Laboratories. Thermal Neutron Capture Gamma-rays (CapGam). Retrieved from: http://www.nndc.bnl.gov/capgam/

Brookhaven National Laboratories. Nuclear Structure and Decay Data (NuDat). Retrieved from: http://www.nndc.bnl.gov/nudat2/index.jsp

Brookhaven National Laboratories. Table of Nuclides. Retrieved from: http://www2.bnl.gov/ton/index.html

Canberra. Spectroscopy Amplifier Model 2020 Operator's Manual.

Carew S. The Use of In Vivo X-Ray Fluorescence Measurements in the Analysis of Cadmium Toxicology. MSc Thesis. McMaster University (2001)

Duderstadt J.J., Hamilton L.J. Nuclear Reactor Analysis. John Wiley & Sons, Inc. First Edition. (1976)

Ember P.P., Belgya T., Weil J.L., Molnar G.L. Coincidence Measurement Setup for PGNAA and Nuclear Structure Studies. *Applied Radiation and Isotopes.* **57**, 573-577, (2002)

Ernest Orlando Lawrence Berkeley National Laboratory. Table of Isotopes. Retrieved from: http://ie.lbl.gov/toi.htm

Failey M.P. Neutron Capture Prompt Gamma Ray Activation Analysis: A Versatile non Destructive Technique for Multielement Analysis of Complex Matrices. PhD Thesis. University of Maryland (1979)

Gardner R.P., Mayo C.W., El-Sayyed E.S., Metwally W.A., Zheng Y., Poezart M. A Feasibility Study of a Coincidence Counting Approach for PGNAA Aplications. *Applied Radiation and Isotopes.* **53**, 535-541, (2000)

Grinyer J. PhD Student. Personal Communication. Medical Physics and Applied Radiation Sciences Unit. McMaster University (2004)

Hertel N.E., Sweezy J.E. Neutron Flux Measurement by Activation Analysis Reactor Laboratory. Georgia Institute of Technology. Atlanta, GA. Internal article. Laboratory problem

ICRP 74. Conversion Coefficients for Air Kerma per Unit Photon Fluence.

Karamanis D., Lacoste V., Andriamonje S., Barreau G., Petit M. Experimental and Simulated Efficiency of a HPGe Detector With Point-Like and Extended Sources. *Nuclear Instruments and Methods in Physics Research A.* **487**, 477-487, (2002)

Kennedy J.A. A Comparison of McMaster Nuclear Reactor Irradiation Experiments with Simulation. MEng Thesis. McMaster University (2000)

Knoll G.F. Radiation Detection and Measurement. Second edition. John Wiley & Sons, Inc. (1989)

Krane K.S. Introductory Nuclear Physics. John Wiley & Sons Inc. Second Edition. (1998)

Kruger P. Principles of Activation Analysis. First Edition. John Wiley & Sons, Inc. 1971

McMaster Nuclear Reactor Website: http://www.science.mcmaster.ca/mnr/Main-Page/Frameset-homepage.htm

MCNP manual, version 4C2. Oak Ridge National Laboratories. Oak Ridge Tennessee 2000

Medical Physics 4R06. Lecture Notes. McMaster University. 2000/2001

Mildner D.F.R., Arif M., Stone C.A. The Neutron Transmission of Single-Crystal Sapphire Filters. *J. Appl. Cryst.* **26**, 438-447, (1993)

NCRP 38 (10CFR835). Neutron Dose Equivalent per Unit Fluence

Nieman H.F., Tennant D.C., Dolling G. Single Crystal Filters for Neutron Spectrometry. *Review of Scientific Instruments.* **51**, 10, 1299-1330, (1980)

Nuclear Data Inc. ND580 Series Analog to Digital Converter Operator's Manual 07-0300. (1986)

Nuclear Data Inc. ND599 Loss-Free Counting (LFC) Module Operator's Manual 07-0191. (1987)

Olsher R.H., Seagraves D.T. Practical MCNP for the Health Physicist Rad Engineer & Medical Physicist. MCNP courseware. Los Alamos National Laboratories. 2004

O'Meara J.M. Measuring Lead, Mercury and Uranium by In Vivo X-Ray Fluorescence. Phd Thesis. McMaster University (1999)

Palerme S. Pilot Studies for In Vivo Bone Aluminum Measurements. MSc Thesis. McMaster University (1993)

Pejovic-Milic A. An Accelerator Based In Vivo Measurement of Aluminum in Human Bone by Neutron Activation Analysis. MSc Thesis. McMaster University (1998)

Reactor Experiments Inc. Catalog No. 1551, 1552, 1553. Activation Foils. Fast Neutron Foils (1551). Thermal / Resonance Foils (1552). Broad Spectrum Foils (1553)

Shaw D.M., Smith P.L.C. Concentration of B, Sm, Gd and H in 24 Reference Materials. Internal Study. McMaster University (1990)

Stamelatos I.E., Messoloras S. Sapphire Filter Thickness Optimization in Neutron Scattering Instruments. *Review of Scientific Instruments.* **71**, 1, 70-73, (2000)

Swift-Schultz C.L. Neutron Dose-Equivalent Estimation for Rat Whole-Body Calcium Measurements. MSc Thesis. McMaster University (1985)

Technical Report Series No. 107. Neutron Fluence Measurements. International Atomic Energy Agency (IAEA), Vienna 1970

Tomlinson, Landsberger, Smith, Neutron Capture Prompt Gamma Ray Activation Analysis (PGAA) of Selected Elements in NRC Marine Sediment Standard BCSS-1. Internal Study. McMaster University (undated)